UNIVERSITY OF WEST ATTICA

DEPARTMENT OF MECHANICAL ENGINEERING

MACHINE ELEMENTS & VEHICLES LABORATORY

# Modelling and simulation of the dynamical response of coaxial magnetic gear transmissions admitting computationally lightweight and robust solutions for torque modelling and power losses

Doctoral Dissertation

Panteleimon Tzouganakis

**Supervision:** Antonios Tsolakis, Associate Professor, UNIWA

Athens, July 2024

ΠΑΝΕΠΙΣΤΗΜΙΟ ΔΥΤΙΚΗΣ ΑΤΤΙΚΗΣ

ΤΜΗΜΑ ΜΗΧΑΝΟΛΟΓΩΝ ΜΗΧΑΝΙΚΩΝ

ΕΡΓΑΣΤΗΡΙΟ ΣΤΟΙΧΕΙΩΝ ΜΗΧΑΝΩΝ ΚΑΙ ΟΧΗΜΑΤΩΝ

# Μοντελοποίηση και προσομοίωση της δυναμικής συμπεριφοράς ομοαξονικών μαγνητικών μεταδόσεων κίνησης με χρήση εύρωστων και χαμηλού υπολογιστικού κόστους λύσεων για την περιγραφή της ροπής και των απωλειών ισχύος

Διδακτορική Διατριβή

Παντελεήμων Τζουγανάκης

**Επίβλεψη:** Αντώνιος Τσολάκης, Αναπληρωτής Καθηγητής, ΠΑΔΑ

Αθήνα, Ιούλιος 2024

# ΔΗΛΩΣΗ ΣΥΓΓΡΑΦΕΑ ΔΙΔΑΚΤΟΡΙΚΗΣ ΔΙΑΤΡΙΒΗΣ

Ο κάτωθι υπογεγραμμένος Τζουγανάκης Παντελεήμων του Μιλτιάδη, υποψήφιος διδάκτορας του Τμήματος Μηχανολόγων της Σχολής Μηχανικών του Πανεπιστημίου Δυτικής Αττικής, δηλώνω ότι:

«Είμαι συγγραφέας και δικαιούχος των πνευματικών δικαιωμάτων επί της διατριβής και δεν προσβάλλω τα πνευματικά δικαιώματα τρίτων. Για τη συγγραφή της διδακτορικής μου διατριβής δεν χρησιμοποίησα ολόκληρο ή μέρος έργου άλλου δημιουργού ή τις ιδέες και αντιλήψεις άλλου δημιουργού χωρίς να γίνεται αναφορά στην πηγή προέλευσης (βιβλίο, άρθρο από εφημερίδα ή περιοδικό, ιστοσελίδα κ.λπ.). Επίσης, βεβαιώνω ότι αυτή η εργασία έχει συγγραφεί από μένα αποκλειστικά και αποτελεί προϊόν πνευματικής ιδιοκτησίας τόσο δικής μου, όσο και του Ιδρύματος. Παράβαση της ανωτέρω ακαδημαϊκής μου ευθύνης αποτελεί ουσιώδη λόγο για την ανάκληση του διδακτορικού διπλώματος μου».

Επιθυμώ την άμεση διάθεση στο πλήρες κείμενο της διατριβής μου έπειτα από αίτηση μου στη Βιβλιοθήκη.

Ο Δηλών

**Supervisory Board**

1.Antonios Tsolakis, Ass. Prof. UNIWA


2.Vasilios Spitas, Prof. NTUA

Vasileios Spitas
26.11.2024 12:38

3.Yerassimos Panayiotatos, Prof. UNIWA

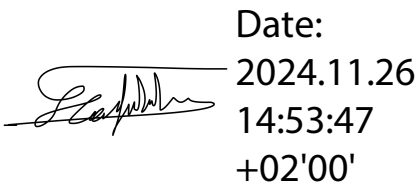


**Seven-member committee**

1.Antonios Tsolakis, Ass. Prof. UNIWA

2.Vasilios Spitas, Prof. NTUA

3.Yerassimos Panayiotatos, Prof. UNIWA

4. Constantinos Stergiou, Prof. UNIWA

5. Georgios Nicolaides, Prof. UNIWA

6. Antonios Kladas, Prof. NTUA

7. Pantelis Nikolakopoulos, Prof. UPatras

# ACKNOWLEDGEMENTS

Throughout my work in my PhD thesis and my career as a mechanical engineer there is a significant number of people I would like to express my gratitude for their continuous support and encouragement.

First and foremost, I would like to thank my family for their support and encouragement. Their financial support has been pivotal since I was an undergraduate student.

I would also like to thank my colleagues and friends who were along my journey as a mechanical engineer. I would especially like to thank Christos Papalexis, Christos Kalligeros and Dimitrios Krifos. I met them since the first days as an undergraduate student and we continue to work together as they also embarked in the pursuit of a doctoral title. The countless hours of discussions, modelling and coding we shared have forged me as an engineer and as a person.

In addition, I would like to thank Vasilis Gakos whom I met as a supervisor of his diploma thesis. His effort has been invaluable in my PhD thesis. Specifically, Vasilis has assisted me in the developing and the validation of the key findings in my thesis. Furthermore, I would like to thank Nikolina Nikolarea and Christos Floros for their support in certain parts of my PhD thesis.

Furthermore, I would like to thank my supervising professors Prof. Antonios Tsolakis, Prof. Vasilios Spitas and Prof. Yerassimos Panayiotatos. Their help and guidance have been crucial to the conclusion of my thesis. I would like to thank Prof. Tsolakis for accepting me as his PhD student at University of West Attica. I would like to thank Prof. Spitas whom I met as an undergraduate student in the school of Mechanical Engineering in the National Technical University of Athens. I have also concluded my diploma thesis under his supervision. The countless hours of discussions in a variety of scientific fields have been a source of inspiration for me as a researcher.

Moreover, I would like to thank all of my friends in my life from my close friends to recent acquaintances. From the friends that I met in my early childhood, the friends that I made during my career as a chess player, to the most recent people that came into my life.

Finally, I would to thank everyone that inspired me as person, as an engineer and as a researcher.

I wish them health, happiness and success in their life

# ABSTRACT

Coaxial magnetic gears (CMGs) have been of great interest amongst researchers and the industry since their introduction two decades ago. Magnetic gears possess significant advantages compared to mechanical gears such as higher performance in terms of attained speeds, versatility, vibration attenuation, backdrivability and efficiency. However, some drawbacks limit their wide adoption in the industry. Even with the use of rare-earth permanent magnets and implementing sophisticated designs the torque density of magnetic gears is significantly lower compared to mechanical gears. Increasing the torque density is a major issue in magnetic drivetrains and has been extensively discussed in the literature. However, the calculation of the torque is typically performed through FEA and/or numerical methods, thus increasing the computational cost for optimization processes. Furthermore, slippage that occurs during transient operation of CMG drives is a phenomenon that should be thoroughly investigated since it limits their operation when high acceleration/deceleration is present. The analysis of slippage in the literature has been conducted by mainly implementing FE transient simulations or with other iterative methods, without giving additional insights on the complex dynamical phenomena of CMGs and with high computational cost. Finally, power losses due to eddy current and core losses are a significant drawbacks in CMG drives and should be examined since high values of power losses could lead to excess heat that could increase the temperature of the system leading to degradation of the permanent magnets and the CMG as a whole. The power losses are usually calculated implementing FE transient simulations that require high computational cost and therefore limiting optimization methods aiming towards the reduction of eddy current and core losses.

The objective of this thesis is to introduce two analytical 2D models for fast and efficient calculation of the applied torques for every rotation angle, geometry configuration and constitutive parameters of the magnets using the Maxwell Stress Tensor. The first model refers to the standard CMG drive, while the second to the Halbach-array CMG drive, due to its comparative advantages. The results obtained from the models were compared against those obtained from FEA. The calculated torques at the inner and outer rotor were in perfect agreement with FEA, however the analytical models were more than two orders of magnitude faster. In addition, an analytical calculation of the torque ripple in coaxial magnetic gear drives is made possible using the proposed models. An investigation of the influence of the modulator ring on stall torque was performed illustrating that there is an optimum arc length for the ferromagnetic segment to maximize torque density.

Furthermore, the dynamical equations of the coaxial magnetic gear drive were formulated and a model was developed to simulate the dynamical response of the system without the requirement of torque calculation at each time step that significantly decreases computational cost. The slippage phenomenon was thoroughly investigated in the present thesis. It was demonstrated that the governing equations of the dynamical response of the coaxial magnetic gear are the same with the dynamical equation of the driven pendulum. A non-dimensional criterion was

formulated for the prediction of the dynamical behavior of the CMG drive during transient operation. Finally, it was demonstrated that the dynamical response of the CMG drive could exhibit chaotic behavior under certain conditions. With the developed analysis, besides the significant reduction of the computational cost important insights regarding the complex dynamical phenomena during the operation of CMG drives are obtained.

Moreover, a detailed analysis regarding the calculation of power losses during the operation of CMGs has been conducted. Using the analytical calculation of the magnetic induction the eddy current losses in the permanent magnets of the CMG and the core losses on the modulator ring were obtained. An investigation on the effect of the magnet segmentation to the power losses was conducted, illustrating that eddy current losses can be significantly reduced by applying this technique.

Finally, a detailed design of a CMG drive is presented showcasing the important designs aspects for manufacturing a robust and efficient CMG drive. A detailed analysis regarding the bearing tolerances and their subsequent effect on the natural frequencies of the CMG drive is conducted illustrating its significance as a design aspect.

# ΠΕΡΙΛΗΨΗ

Τα ομοαξονικά συστήματα μαγνητικής μετάδοσης κίνησης (coaxial magnetic gears) έχουν προκαλέσει μεγάλο ενδιαφέρον στους ερευνητές και τη βιομηχανία από την εισαγωγή τους πριν από δύο δεκαετίες. Τα ομοαξονικά συστήματα μαγνητικής μετάδοσης κίνησης διαθέτουν σημαντικά πλεονεκτήματα σε σύγκριση με τα μηχανικά όπως υψηλότερη απόδοση όσον αφορά τις ταχύτητες που επιτυγχάνονται, μειωμένο θόρυβο και φθορά, μικρότερο κόστος συντήρησης, ενώ δεν απαιτείται λίπανση. Ωστόσο, ορισμένα μειονεκτήματα περιορίζουν την ευρεία υιοθέτησή τους στη βιομηχανία. Ακόμη και με τη χρήση μόνιμων μαγνητών σπάνιας γαίας και την υλοποίηση πολύπλοκων σχεδιασμών, η πυκνότητα ροπής των μαγνητικών μεταδόσεων είναι σημαντικά χαμηλότερη σε σύγκριση με τις μηχανικές μεταδόσεις. Η αύξηση της πυκνότητας ροπής αποτελεί ένα σημαντικό ζήτημα στις μαγνητικές μεταδόσεις και έχει αναφερθεί εκτενώς στην βιβλιογραφία. Ωστόσο, ο υπολογισμός της ροπής συνήθως γίνεται μέσω μεθόδων πεπερασμένων στοιχείων (FEA) και/ή αριθμητικών μεθόδων, αυξάνοντας έτσι το υπολογιστικό κόστος για τις διαδικασίες βελτιστοποίησης. Επιπλέον, η ολίσθηση που συμβαίνει κατά την μεταβατική λειτουργία είναι ένα φαινόμενο που πρέπει να ερευνηθεί εκτενώς καθώς περιορίζει τη λειτουργία των μαγνητικών μεταδόσεων όταν υπάρχει υψηλή επιτάχυνση/επιβράδυνση. Η ανάλυση της ολίσθησης στη βιβλιογραφία έχει γίνει κυρίως μέσω της υλοποίησης προσομοιώσεων FEA μεταβατικής κατάστασης ή με άλλες αριθμητικές μεθόδους, χωρίς να δίνουν πρόσθετες πληροφορίες για τα πολύπλοκα δυναμικά φαινόμενα και με υψηλό υπολογιστικό κόστος. Τέλος, οι απώλειες ισχύος λόγω δινορευμάτων αποτελούν σημαντικά μειονεκτήματα και πρέπει να εξεταστούν καθώς υψηλές τιμές απωλειών ισχύος μπορεί να οδηγήσουν σε υπερβολική παραγωγή θερμότητας που μπορεί να αυξήσει τη θερμοκρασία του συστήματος οδηγώντας σε υποβάθμιση των μόνιμων μαγνητών και του συστήματος συνολικά. Οι απώλειες ισχύος συνήθως υπολογίζονται υλοποιώντας προσομοιώσεις FEA μεταβατικής κατάστασης που απαιτούν υψηλό υπολογιστικό κόστος και κατά συνέπεια περιορίζουν τις μεθόδους βελτιστοποίησης που στοχεύουν στη μείωση των δινορευμάτων.

Η παρούσα διδακτορική διατριβή πραγματεύεται την μελέτη και την μοντελοποίηση ομοαξονικών συστημάτων μαγνητικής μετάδοσης κίνησης . Στην παρούσα διατριβή αναπτύχθηκε ένα καινοτόμο αναλυτικό μοντέλο για τον υπολογισμό του μαγνητικού πεδίου και των εφαρμοζόμενων ροπών για κάθε γωνία περιστροφής. Για τον υπολογισμό του μαγνητικού πεδίου χρησιμοποιήθηκαν οι εξισώσεις Maxwell ενώ για τον υπολογισμό της ροπής ο Τανυστής Maxwell. Επιπλέον, αποδείχτηκε ότι η ροπή σε οποιαδήποτε σχετική θέση των δυο ροτόρων μπορεί να υπολογιστεί συναρτήσει της γωνίας περιστροφής τους και της μέγιστης ροπής (stall torque). Οι υπολογισθείσες ροπές επαληθεύτηκαν με υπολογιστικά πακέτα πεπερασμένων στοιχείων του εμπορίου (ANSYS Maxwell). Το μοντέλο αυτό γενικεύτηκε για την περίπτωση των ομοαξονικών συστημάτων μαγνητικής μετάδοσης κίνησης με την χρήση διατάξεων Halbach (Halbach-array coaxial magnetic gears). Με την χρήση της διάταξης αυτής, γίνεται δυνατή η επίτευξη υψηλότερης πυκνότητας ροπής σε σχέση με την περίπτωση του απλού μαγνητικού συστήματος. Στην διατριβή έγινε ο αναλυτικός υπολογισμός της ροπής που θα ασκηθεί για κάθε σχεδιασμό της διάταξης Halbach.

Επιπλέον, αποδείχτηκε ότι σχέση που συνδέει τις ροπές στους δυο ρότορες με την μέγιστη ροπή και τις σχετικές γωνίες είναι ίδιος με την περίπτωση του απλού μαγνητικού συστήματος. Με τον τρόπο αυτό μπορεί εύκολα να πραγματοποιηθεί η βελτιστοποίηση της διάταξης των ομοαξονικών μαγνητικών συστημάτων μετάδοσης κίνησης για την επίτευξη της μέγιστης δυνατής πυκνότητας ροπής με μεγάλη ακρίβεια και χαμηλό υπολογιστικό κόστος λόγω του αναλυτικού τρόπου επίλυσης του φαινομένου.

Στην συνέχεια, σημαντική βαρύτητα δόθηκε στην μελέτη της δυναμικής συμπεριφοράς των ομοαξονικών συστημάτων μαγνητικής μετάδοσης κίνησης καθώς η ολίσθηση (slippage) αποτελεί σημαντικό πρόβλημα σε αυτές τις μεταδόσεις. Στην βιβλιογραφία ο υπολογισμός της δυναμικής απόκρισης γίνεται συνήθως με την χρήση υπολογιστικών πακέτων τα οποία έχουν μεγάλο υπολογιστικό κόστος. Στην παρούσα διατριβή χρησιμοποιώντας το αναλυτικό μοντέλο υπολογισμού των ροπών που περιγράψαμε παραπάνω έγινε δυνατή η κατάστρωση των δυναμικών εξισώσεων του συστήματος με αναλυτική μορφή. Στην συνέχεια δημιουργήθηκε ένα αδιάστατο κριτήριο το οποίο μπορεί να προσδιορίσει την συμπεριφορά που θα έχει το σύστημα χωρίς την ανάγκη επίλυσης του συστήματος των εξισώσεων με την χρήση αριθμητικών μεθόδων. Επομένως, με το κριτήριο αυτό γίνεται δυνατός ο υπολογισμός της μέγιστης δυνατής επιτάχυνσης που μπορεί να εφαρμοστεί προκείμενου το ομοαξονικό μαγνητικό σύστημα μετάδοσης κίνησης να μην ξεπεράσει το μέγιστο επιτρεπτό σφάλμα ανάλογα την εφαρμογή που αυτό θα χρησιμοποιηθεί. Αποδείχτηκε ότι η δυναμική συμπεριφορά του συστήματος κατά την επιτάχυνση είναι παρόμοια με την συμπεριφορά του εκκρεμούς (driven pendulum). Τέλος, δείχθηκε ότι υπό ορισμένες συνθήκες επιτάχυνσης το σύστημα μπορεί να παρουσιάσει χαοτική συμπεριφορά.

Έπειτα, έγινε μελέτη των αναπτυσσόμενων δινορευμάτων εξαιτίας των εναλλασσόμενων μαγνητικών πεδίων κατά την περιστροφή του συστήματος. Τα δινορεύματα έχουν ως αποτέλεσμα την αύξηση της θερμοκρασίας του συστήματος γεγονός που μπορεί να οδηγήσει σε υποβάθμιση των μαγνητικών ιδιοτήτων, που θα έχει ως αποτέλεσμα την υποβάθμιση του συστήματος συνολικά. Για το λόγο αυτό η μελέτη των δινορευμάτων είναι σημαντική και απαραίτητα κατά τον σχεδιασμό των ομοαξονικών συστημάτων μαγνητικής μετάδοσης κίνησης. Στην παρούσα διατριβή με την χρήση των αναλυτικών μοντέλων υπολογισμού του μαγνητικού πεδίου για κάθε γωνία περιστροφής των δυο ροτόρων έγινε αναλυτικός υπολογισμός των απωλειών του συστήματος λόγω των δινορευμάτων. Τα αποτελέσματα επαληθεύτηκαν με υπολογιστικά πακέτα πεπερασμένων στοιχείων του εμπορίου (ANSYS Maxwell). Τέλος, δείχθηκε ότι με την χρήση τεχνικών ελασματοποίησης των μαγνητών (magnet segmentation) οι απώλειες των δινορευμάτων μπορούν να μειωθούν σημαντικά.

Τέλος, έγινε ο σχεδιασμός ενός ομοαξονικού συστήματος μαγνητικής μετάδοσης κίνησης στο οποίο τονίστηκαν τα σημαντικά σημεία κατά την διάρκεια του σχεδιασμού/κατασκευής. Ιδιαίτερη έμφαση δόθηκε στην επιλογή των κατάλληλων ανοχών των αξόνων και των ρουλεμάν με σκοπό την αποφυγή των επικίνδυνων για την ομαλή λειτουργία ιδιοσυχνοτήτων.

# THESIS OVERVIEW

To facilitate the reading of the present thesis a brief introduction of each chapter is presented herein:

**Introduction:** A brief literature review on magnetic gears is presented. In addition, an introduction on non-linear dynamics and chaos theory is presented focusing on the complex dynamics of the damped-driven pendulum that would prove to be important for the understanding of the dynamical phenomena in coaxial magnetic gear drives.

**Chapter 1:** The analytical modelling of the scalar magnetic potential, the magnetic induction and the induced torque in the two rotors of the CMG drive is presented. The analytical solutions are compared with FEA results. An investigation on the effect of the modulator ring to the stall torque is conducted. The developed model in this Chapter is the core model of the present thesis.

**Chapter 2:** The analytical model derived in Chapter 1 is generalized for the case of Halbach-array CMG drives. It is demonstrated that every Halbach-array CMG could be analyzed in the same way as the standard CMG. It is illustrated that Halbach-array CMG achieve superior performance compared to the standard CMG.

**Chapter 3:** A detailed investigation on the dynamics of the CMG during transient operation is presented. The similarities between the CMG and the driven-pendulum are showcased. An analysis and the formulation of a non-dimensional criterion that predicts the response of the CMG drive during transient operation is derived. Furthermore, it is demonstrated that under certain conditions, the dynamical response of the CMG drive could exhibit chaotic behavior showcasing the fascinating dynamics of the CMG drive.

**Chapter 4:** A detailed analysis on the power losses due to eddy current and core losses. An analytical calculation of the power losses during the operation of the CMG is derived using the analytical calculation of the magnetic induction as obtained in Chapter 1.

**Chapter 5:** A detailed design of CMG drive is presented showcasing the important designs aspects for manufacturing a robust and efficient CMG drive.

# Contents

**Introduction** ..... **15**

*I.1 Magnetic Gears* ..... *15*

*I.1.1 Magnetic Gear Topologies* ..... *15*

*I.1.1.1 Non-modulated magnetic gears* ..... *15*

*I.1.1.2 Modulated magnetic gears* ..... *16*

*I.1.1.3 The Coaxial Magnetic Gear* ..... *20*

*I.2 Maxwell Equations* ..... *21*

*I.3 Non-linear dynamics* ..... *22*

*I.3.1 The pendulum problem* ..... *22*

*I.3.2 The essence of chaos* ..... *31*

*Appendix AI.1* ..... *35*

*Appendix AI.2* ..... *37*

*Introduction-References* ..... *39*

**1 2D Analytical Modelling of Coaxial Magnetic Gears** ..... **45**

*1.1 Magnetic Potential Calculation* ..... *45*

*1.2 Boundary Conditions* ..... *52*

*1.3 Torque Calculation* ..... *56*

*1.4 Torque as a function of rotation* ..... *59*

*1.5 Validation of the analytical model with FEA* ..... *60*

*1.6 Influence of modulator ring in torque density* ..... *72*

*Chapter 1-Conclusions* ..... *74*

*Appendix A1.1* ..... *75*

*Appendix A1.2* ..... *77*

*Appendix A1.3* ..... *79*

*Appendix A1.4* ..... *84*

*Appendix A1.5* ..... *85*

*Appendix A1.6* ..... *86*

*Chapter 1-References* ..... *88*

**2 Halbach-Array Coaxial Magnetic Gears** ..... **89**

*2.1 Analytical model of Halbach-array CMG drives* ..... *89*

*2.2 Optimization of HAL-CMG and comparison with standard CMG* ..... *95*

*Chapter 2-Conclusions* ..... *98*

*Appendix A2.1* ..... *99*

*Chapter 2-References* ..... *102*

**3 Dynamical response in coaxial magnetic gears** ..... **103**

*3.1 Non-dimensionalization of the governing ODEs* ..... *104*
*3.2 Modelling for acceleration with ripple and chaotic behaviour* ..... *107*
*3.3.1 Verification of the stability criterion and discussion* ..... *108*
*3.3.2 Chaotic behaviour and discussion* ..... *109*
*Chapter 3-Conclusions* ..... *119*
*Appendix A3.1* ..... *120*
*Chapter 3-References* ..... *121*

***4 Power losses in coaxial magnetic gears*** ..... **123**
*4.1 Mathematical Modelling of Power Losses* ..... *124*
*4.1.1 Eddy current losses in the PMs* ..... *124*
*4.1.2 Tangential segmentation of PMs* ..... *125*
*4.1.3 Computation of core losses of the ferromagnetic segments using a hybrid model* ..... *126*
*4.2 Results and discussion* ..... *129*
*4.2.1 Eddy current and core losses calculation and comparison with FEA* ..... *129*
*4.2.2 Power losses for different external loads* ..... *133*
*4.2.3 Algorithm computational cost vs accuracy* ..... *133*
*4.2.3.1 Reduction of time steps* ..... *133*
*4.2.3.2 Mesh sensitivity analysis* ..... *134*
*Chapter 4-Conclusions* ..... *136*
*Chapter 4-References* ..... *137*

***5 Design of an experimental coaxial magnetic gear*** ..... **139**
*5.1 Basic Geometrical Parameters* ..... *139*
*5.2 Alternative ways of operation* ..... *140*
*5.3 Stress on the rotors and modulator ring* ..... *141*
*5.4 Magnet attachment to the rotors* ..... *143*
*5.5 Bearing selection and natural frequencies of the CMG* ..... *145*
*5.6 Temperature calculation of the CMG due to power losses* ..... *147*
*5.7 Torque ripple due to radial forces* ..... *148*
*Chapter 5-Conclusions* ..... *150*
*Chapter 5-References* ..... *151*

***Thesis Conclusions*** ..... **153**

***Thesis Novelties*** ..... **155**

***Future Work*** ..... **157**

***Thesis Publications*** ..... **159**

***Other publications of the author*** ..... **161**

# *Introduction*

## *I.1 Magnetic Gears*

Mechanical gears have been extensively used in power transmission application by the industry since they can achieve high torque densities. However, they are prone to various problems such as noise, friction, requirement for lubrication, wear, fatigue and as a consequence poor reliability. Magnetic gears (MGs) on the other hand, have much lower level of noise, vibration and wear, therefore requiring a significantly lower maintenance cost compared to mechanical gears. In addition, since there is no contact between the shafts, MGs are protected against overload, leading to higher reliability [I.1] while making them ideal for vibration attenuation applications. In addition, backdrivability is a major advantage of magnetic drives, since there is no reduction in the efficiency of transmission when it works in reverse. Therefore, MGs could be used in a variety of applications [I.2] such as in aircraft mechanical transmission [I.3]-[I.5], wind power generation [I.6]-[I.9], wave energy conversion [I.10], traction [I.11] and aerospace [I.12].

### *I.1.1 Magnetic Gear Topologies*

The concept of MGs can be traced back to the early 1900s. Armstrong's patent [I.13] laid the foundation by introducing a power-transmission device using magnetic force, initially relying on coil-generated magnetism instead of permanent magnets (PMs). The first MG utilizing solely PMs was developed in 1941 [I.14]. In 1968, Martin proposed a patent for a coaxial MG [I.15]. During that time, various MG designs emerged, but their torque density was limited due to suboptimal magnet performance and use. The advent of high energy product ($BH_{max}$) rare-earth magnets reignited interest in MGs. Particularly since 2001, following Atallah's [I.16] introduction of a novel coaxial MG with NdFeB magnets, MG research has been increasingly prominent. MG topologies are categorized into two main groups. The first group comprises what are known as conventional non-modulated MGs, while the second group comprises of modulated MGs.

#### *I.1.1.1 Non-modulated magnetic gears*

These types of MGs function through non-contact interactions where Permanent Magnets (PMs) are arranged in various configurations to interact magnetically. Essentially, the concept of conventional MGs is derived from traditional mechanical gears. Examples include the spur gear, as illustrated in Fig.I.1(a), the worm gear depicted in Fig.I.1(b), the perpendicular gear shown in Fig.I.1(c), the magnetic screw as in Fig.I.1(d), and the skew gear. These conventional MGs, despite their straightforward design, often exhibit low torque density, due to the poor utilization of magnets making them unattractive for industrial applications [I.1].

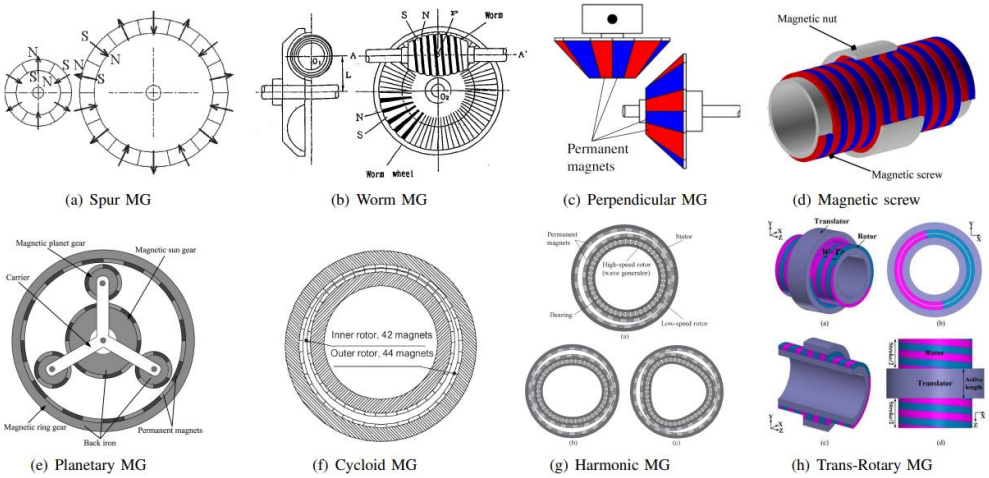


**Figure I.1: Different non-modulated topologies of magnetic gear drives that has been proposed to literature [I.1]**

In contrast, some other conventional MG topologies demonstrate significantly high torque densities, albeit with more complex structures. An example is the magnetic planetary gearing setup, analogous to mechanical planetary gears, which was simulated and built as shown in Fig.I.1(e) [I.17]. Simulations revealed that with six magnetic planet gears, the torque density approached 100 kNm/m³, compared to less than 50 kNm/m³ with a three-planetary-gear system. Another example, the cycloid MG depicted in Fig.I.1(f) and based on cycloid gearing principles, was detailed in [I.18]. This design uses cycloid motion to modulate the air gap between two magnetic rings, enabling effective gear reduction. Experimentally, it achieved a torque density of approximately 107 kNm/m³. Additionally, a magnetic version of the harmonic gear, shown in Fig.I.1(g) and analyzed in [I.19], suits applications requiring high gear ratios. This MG design offers ripple-free torque transmission and can reach torque densities up to 150 kNm/m³ at high gear ratios. While the cycloid and harmonic MGs boast high torque densities and gear ratios, their mechanical complexity significantly impedes commercialization prospects. Moreover, a transrotary MG, investigated in [I.20] and shown in Fig.I.1(h), presents another example of innovative MG design.

### *I.1.1.2 Modulated magnetic gears*

This group appears to be particularly promising due to its combination of high efficiency and high torque density. A notable advantage of these configurations is that all the permanent magnets (PMs) are engaged in torque transmission. This involvement of all PMs is instrumental in achieving the high torque density. Different modulated MG topologies are presented in Fig.I.2.

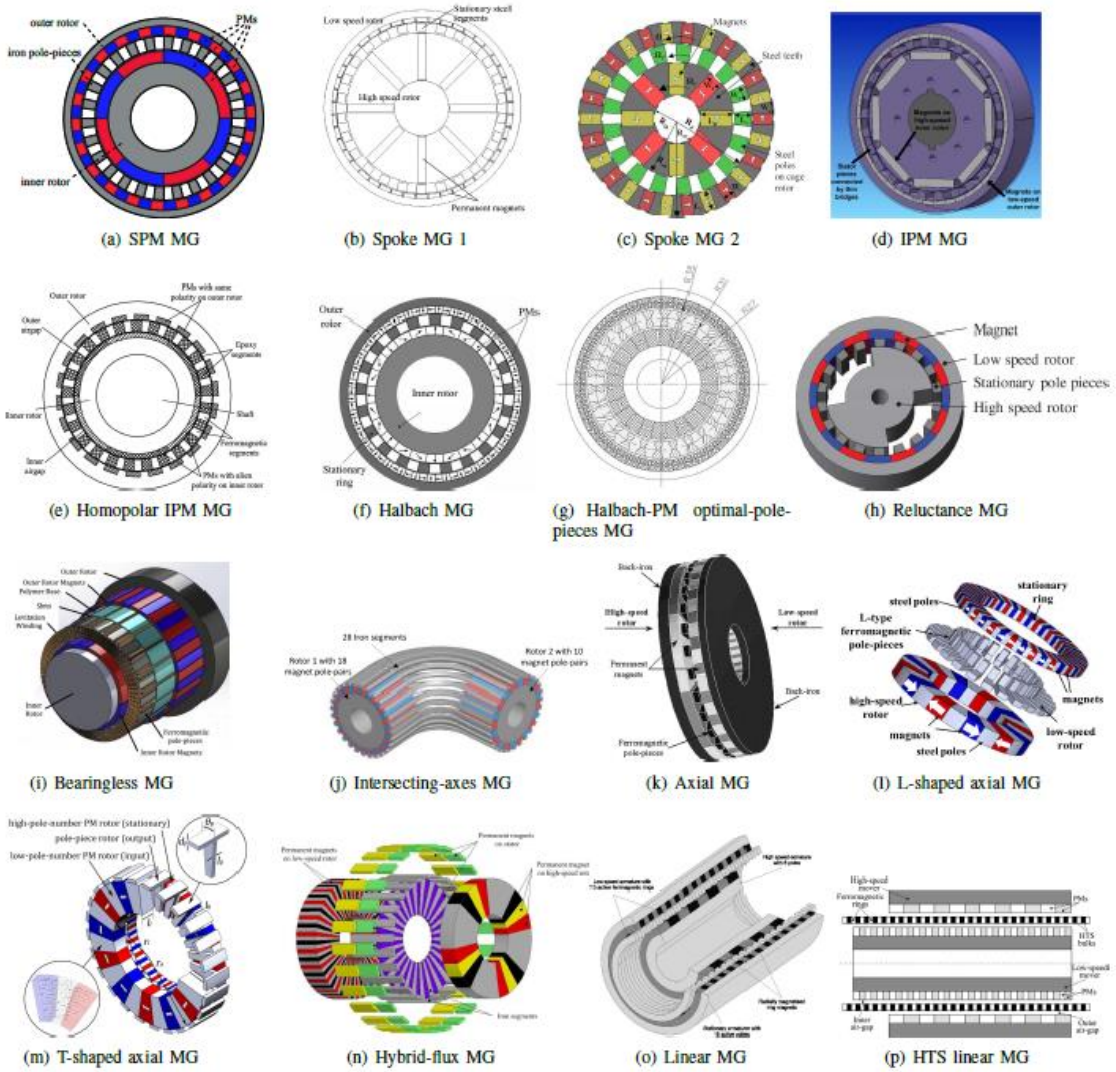


**Figure I.2: Different modulated topologies of magnetic gear drives that has been proposed to literature [I.1]**

The initial proposal for a coaxial Magnetic Gear (MG) using rare-earth magnets was made in [I.16], as depicted in Fig.I.2(a), with detailed design and performance analysis provided in [I.16] and [I.21]. This MG consists of three components: Permanent Magnets (PMs) attached to both the inner and outer rotors (i.e., Surface-Mounted Permanent Magnet or SPM rotors), and iron pole-pieces (flux modulators) positioned between the two rotors. The yokes of the rotors and iron pole-pieces are made from silicon steel lamination or soft magnetic composite. A prototype demonstrated a transmitted torque density exceeding 70 kNm/m³ [I.21]. Furthermore, it was shown in [I.22] that the coaxial MG can match the performance of its mechanical counterparts. Over the past 20 years, a variety of rotor structures have emerged in the literature.

In [I.23], optimization of this SPM MG topology focused on the flux modulator shape, leading to a prototype with a measured torque density of 111 kNm/m³. Another design, featuring a spoke-type inner rotor shown in Fig.I.2(b), was introduced in [I.24],

achieving a torque density of 54 kNm/m³. It was suggested that a surface-mounted PM rotor might be more effective than a spoke design of the same volume.

In contrast, a lower-cost flux-focusing MG using ferrite magnets was explored in [I.25] and is illustrated in Fig.I.2(c). Experimental evaluations of ferrite, NdFeB, and hybrid designs in [I.26] revealed torque densities of 33 kNm/m³, 151 kNm/m³, and 66 kNm/m³, respectively. Notably, a significant measured torque density of over 200 kNm/m³ was achieved in [I.27] by scaling up a previous NdFeB spoke MG design, indicating that spoke-type MGs achieve very high torque densities when built with NdFeB magnets rather than ferrite.

In [I.28], a coaxial MG incorporating interior PMs was presented, as illustrated in Fig.I.2(d). This study also explored three different methods for connecting stator pole-pieces. A novel coaxial MG design featuring an interior-magnet outer-rotor configuration was introduced in [I.29], shown in Fig.I.2(e). This design employs homopolar Interior IPMs, where PMs of the same polarity are arranged along the circumference of the outer rotor, simplifying manufacturing. However, due to the reduced use of PMs, this prototype achieved a torque density of about 53 kNm/m³.

A coaxial MG utilizing Halbach PM arrays, depicted in Fig.I.2(f), was proposed and thoroughly analyzed in [I.30]. This design demonstrated a 13% increase in torque density, a 67% reduction in cogging torque, and a 28% decrease in total iron losses compared to a standard coaxial MG. NASA's recent studies on MGs with Halbach arrays [I.31] suggest the technology's potential for low-torque applications.

In [I.32], a new coaxial MG design was developed, featuring an optimized iron pole-piece shape and a Halbach magnetic arrangement, as shown in Fig.I.2(g). The proposed pole-piece design potentially increases torque density by 15% or more compared to regular designs. An innovative approach was explored in [I.33] with an air-core coaxial MG using Halbach arrays. This design eliminates the use of back irons attached to the magnets on both inner and outer rotors. Instead, the magnets are mounted on a lighter, nonmagnetic material, leading to designs with reduced weight.

In [I.34], a new type of reluctance MG designed for high-speed transmission was introduced, as seen in Fig.I.2(h). This MG employs salient poles on a high-speed rotor made solely of iron core, creating a simple and robust structure. It eliminates magnet eddy current loss, thus enhancing efficiency. However, its simulated torque density was relatively low at 29.4 kNm/m³.

A bearingless magnetic gear concept was proposed in [I.35], incorporating levitation windings between the iron pole-pieces, as illustrated in Fig.I.2(i). By precisely controlling the current, radial forces can be generated for levitation, without impacting the torque density of the gear. For applications requiring intersecting shafts, a unique solution was described in [I.36]. This design resembles the conventional coaxial MG, but with bent flux modulators, as shown in Fig.I.2(j). The torque density for this topology was limited to 5.4 kNm/m³, constrained by the size of the modulators and flux leakage.

Moving beyond coaxial topologies, various modulated MG structures have been proposed. An axial-field MG was described in [I.37], shown in Fig.I.2(k), achieving a simulated torque density of around 70 kNm/m³. In [I.38], the use of Halbach PM arrays in an axial-field MG was suggested, offering higher torque density than the standard axial-field MG. A novel axial-flux MG with L-shaped modulators and a spoke-type magnet arrangement was presented in [I.39], as seen in Fig.I.2(l). This complex geometry necessitated the use of 3D printing. It improved both flux leakage reduction and torque density, reaching a simulated torque density of 74 kNm/m³ using NdFeB magnets. An axial-transverse-flux MG with T-shaped flux modulators was introduced in [I.40], as depicted in Fig.I.2(m). This design reduces saturation in the iron pole-pieces and limits flux leakage, with a T-shaped modulator creating both axial and transverse flux paths. 3D simulations indicated a significantly higher torque density, up to 280 kNm/m³.

In [I.41], a hybrid transverse-axial MG with additional PMs on the flux modulator side was proposed, as shown in Fig.I.2(n). 3D FEM simulations indicated a torque density of 181.2 kNm/m³, about a 20% improvement over the axial-flux MG. A high-performance linear MG was introduced in [I.42], shown in Fig.I.2(o), with a thrust force density of 1.7 MN/m³. Its operating principle is akin to that of the coaxial MG. Finally, [I.43] proposed a new tubular linear MG utilizing high-temperature superconductor (HTS) bulks for field modulation, as illustrated in Fig.I.2(p). With HTS assistance, the thrust force transmission capacity is significantly enhanced compared to conventional designs.

The torque densities for the different MGs topologies are summarized in Table I.1 [I.1].

**Table I.1: Comparison of different MG topologies in the literature**

| Gear Type | Gear ratio | Torque density (kNm/m$^3$) |
|---|---|---|
| Mechanical Gears | 1-1000 | 47-607 |
| Planetary MG | 3:1 | 97.3 |
| Cycloid MG | 21:1 | 142 |
| Harmonic MG | 360:1 | 75 |
| SPM MG | 5.75:1 | 117 |
| Optimized SPM MG | 10.5:1 | 117 |
| Spoke MG 1 | 5.5:1 | 92 |
| Spoke MG 2 | 4.25:1 | 40 |
| Spoke NdFeB MG | 4.25:1 | 239 |
| IPM MG | 5.5:1 | 64 |
| Homopolar IPM MG | 7.33:1 | 53 |
| Halbach MG | 4.25:1 | 124 |
| Reluctance MG | 8:1 | 29 |
| Axial MG | 5.75:1 | 70 |
| L-shaped axial MG | 3.17:1 | 280 |
| T-shaped axial MG | 3.17:1 | 74 |
| Hybrid-flux MG | 5.5:1 | 181 |

### *I.1.1.3 The Coaxial Magnetic Gear*

The coaxial MG (CMG), shown in Fig.I.3 was proposed by Atallah et al. [I.20] will be investigated in depth in the present thesis. The CMG consists of two concentric iron yokes, the PMs that are mounted on them and a flux-modulator ring that is placed between them. For the proper operation of the CMG it is essential that the number of iron pole pieces used in the modulator ring are equal to the sum of the pole pairs of the PMs in the inner rotor and the pole pairs of the PMs in the outer rotor. Furthermore, the theoretical equivalent gear ratio of CMG in the case of a stationary modulator ring is equal to the quotient of the number of pole pairs in the outer rotor and the number of pole pairs in the inner rotor [I.44]. The optimization of the CMG has been extensively discussed in the literature in order to increase torque density [I.45]-[I.49]. Halbach-array CMG is an improved version of the standard CMG topology due to its higher torque density and its superior dynamical characteristics [I.30].

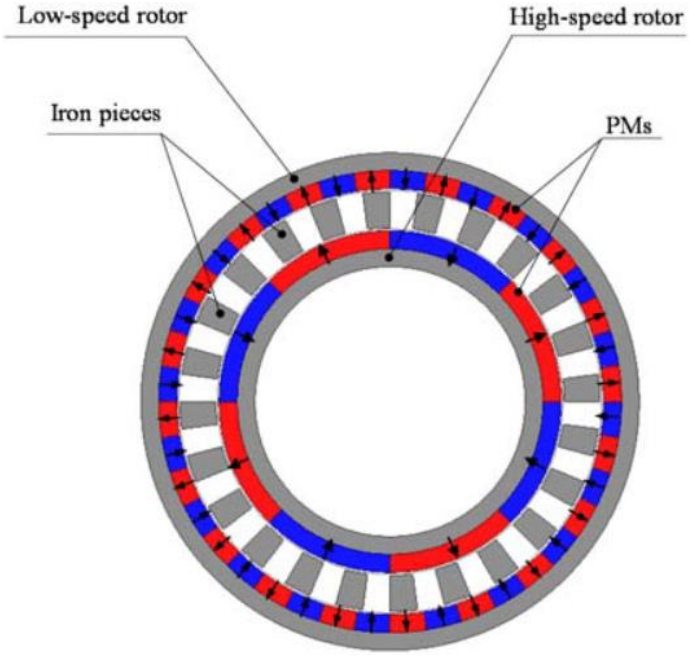


**Figure I.3: The Coaxial Magnetic Gear**

The governing equations of the CMG drive are obtained from Maxwell's equations, however, the non-linearity of the iron pole pieces results to complex systems of partial differential equations (PDEs) that cannot be solved analytically [I.50]. In particular, Jian et al. [I.50] developed a 2D analytical model for the calculation of the scalar magnetic potential assuming equipotential iron pole pieces and implementing a Fourier series formulation to overcome the non-linearity in the boundary conditions of the iron pole pieces. As a consequence, a system of linear equations is formed, from which the coefficients of the general solutions of the system's PDEs are calculated analytically implementing Gauss elimination method. Therefore, for a given design of the CMG drive, the magnetic induction in the radial and tangential directions can be calculated for any angle of rotation of the inner and outer rotor. As a consequence, the torque at the inner and outer rotor of the CMG is determined numerically from the Maxwell

Stress Tensor, [I.51]-[I.52] for every angle of rotation of the rotors. The slip-effect and the dynamical response of the CMG drive during a transient operation are determined by calculating the above torques for the new angle of the rotors' rotation at each time step [I.53]. The transient response of the CMG could also result from finite element analysis (FEA) [I.54]-[I.55].

Due to the complexity and the large number of optimization parameters, i.e. the pole-pairs number, the dimensions of the iron pole pieces (both in radial and tangential direction), the airgap between each rotor and the modulator ring, the thickness of the PMs used it is evident that an analytical model of calculation of the torque would significantly reduce the computational time required for the optimization algorithm. In addition, the variety of optimization goals appear in the design process of a CMG drive regarding each application, i.e. achieve high torque density, attain a desired dynamical response, vibration attenuation, require a fast calculation of the dynamical response of the CMG drive, without the requirement of torque calculation at every time step, since the Gauss elimination algorithm requires a non-negligible computational cost. In this way, an optimization algorithm with a significantly lower computational cost could be developed in order to achieve the desired characteristics of the CMG drive in each design process.

However, specific limitations and inherent problems of MGs have hindered their wide establishment in industrial applications. The torque density of MGs is substantially lower compared to mechanical gears and as a consequence they cannot be used in applications where high torques are required [I.56]. Furthermore, the dynamical response and specifically the slip effect of MGs during the transient state of acceleration or deceleration has to be investigated thoroughly in applications where high accuracy is required [I.2]-[I.4], [I.57]-[I.59]. Finally, eddy current and core losses especially in high angular velocities [I.60] should be investigated when designing a CMG.

## *I.2 Maxwell Equations*

Maxwell's equations, are a set of coupled partial differential equations that, together with the Lorentz force law, form the foundation of classical electromagnetism, classical optics, electric and magnetic circuits. The equations provide a mathematical model for electric, optical, and radio technologies, such as power generation, electric motors, wireless communication, lenses, radar, etc. They describe how electric and magnetic fields are generated by charges, currents, and changes of the fields. The Maxwell equations in their differential form are:

$$\nabla \cdot \mathbf{B} = 0 \tag{I.1}$$

$$\nabla \cdot \mathbf{D} = \rho \tag{I.2}$$

$$\nabla \times \mathbf{H} = \mathbf{J} + \frac{\partial \mathbf{D}}{\partial \mathrm{t}} \tag{I.3}$$

$$\nabla \times \mathbf{E} = -\frac{\partial \mathbf{B}}{\partial \mathrm{t}} \tag{I.4}$$

where $\mathbf{E}$ the electric field intensity, $\mathbf{B}$ the magnetic induction, $\mathbf{H}$ the magnetic field intensity, $\mathbf{J}$ the electric current density, $\mathbf{D}$ the electric displacement and ρ the electric charge density.

The Maxwell equations will be used in Chapter 1 and Chapter 2 of the present thesis in order to model the magnetic induction in coaxial magnetic gears.

## *I.3 Non-linear dynamics*

In mathematics and science, a non-linear system is a system in which the change of the output is not proportional to the change of the input. Non-linear problems are of interest to engineers, physicists, mathematicians, and many other scientists since most systems are inherently nonlinear in nature. Examples of non-linear equations are the Navier-Stokes equations, the Van der Pol oscillator the swinging of a clock pendulum and many others [I.61]-[I.62].

### *I.3.1 The pendulum problem*

It will be demonstrated in the present thesis and specifically in Chapter 3 that the governing equations of the dynamical response in coaxial magnetic gears resemble the driven pendulum. Therefore, it was deemed necessary to briefly introduce the pendulum problem since it showcases a fascinating behaviour even though it is governed, at first glance, by a simple ordinary differential equation.

A pendulum is a body suspended from a fixed support so that it swings freely back and forth under the influence of gravity. When a pendulum is displaced sideways from its resting, equilibrium position, it is subject to a restoring force due to gravity that will accelerate it back towards the equilibrium position. When released, the restoring force acting on the pendulum's mass causes it to oscillate about the equilibrium position, swinging it back and forth.

We will begin our journey of understanding the dynamical behaviour of the pendulum by initially considering the simplest case. Therefore, no damping or external force will be applied to the pendulum except gravity. In order to obtain the governing equation of the pendulum we consider Fig.I.4.

The pendulum equation can be obtained from conservation of energy principle.

The change in potential energy is given by:

$$\Delta U = mgh \tag{I.5}$$

The change in kinetic energy is given by:

$$\Delta K = \frac{1}{2} mu^2 \tag{I.6}$$

Since no energy is lost (no damping) it yields that:

$$mgh = \frac{1}{2}mu^2 \tag{I.7}$$

The velocity for a given change in height can be expressed as:

$$u = \sqrt{2gh} \tag{I.8}$$

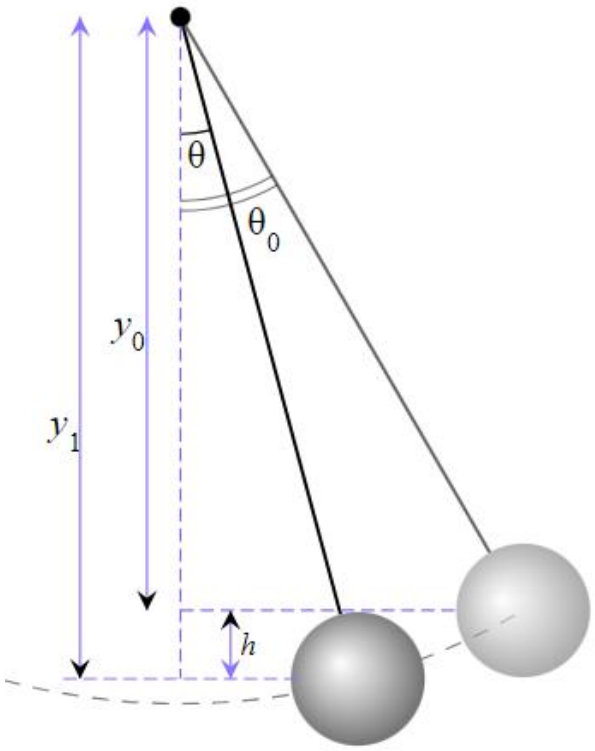


**Figure I.4: Simple pendulum**

From the arc length formula we obtain:

$$u = l\frac{d\theta}{dt} = \sqrt{2gh} \tag{I.9}$$

where $l$ is the length of the pendulum and $g$ the acceleration of gravity .

From Fig.I.3, if the pendulum starts its swing from some initial angle $\theta_0$ then $y_0$, the vertical distance from the screw, is given by:

$$y_0 = l\cos\theta_0 \tag{I.10}$$

Similarly, for $y_1$, we have:

$$y_1 = l\cos\theta \tag{I.11}$$

As a result, the difference of $y_0$ and $y_1$ is:

$$h = l(\cos\theta - \cos\theta_0) \tag{I.12}$$

From Eq.(I.9) and Eq.(I.12) we obtain:

$$\frac{d\theta}{dt} = \sqrt{\frac{2g(\cos\theta - \cos\theta_0)}{l}} \tag{I.13}$$

By differentiating Eq.(I.13) we obtain:

$$\frac{d^2\theta}{dt^2} = \frac{1}{2}\frac{-\frac{2g}{l}\sin\theta}{\sqrt{\frac{2g(\cos\theta - \cos\theta_0)}{l}}}\frac{d\theta}{dt} \tag{I.14}$$

Combining Eq.(I.3) and Eq.(I.14):

$$\frac{d^2\theta}{dt^2} = -\frac{g}{l}\sin\theta \tag{I.15}$$

that yields the governing equation of the pendulum:

$$\ddot{\theta} + \frac{g}{l}\sin\theta = 0 \tag{I.16}$$

The differential equation Eq.(I.16) is not easily solved, and there is no solution that can be written in terms of elementary functions.

When the amplitude of the oscillation of the pendulum the small angle approximation can be used due to the fact that $\sin\theta \approx \theta$. Therefore, Eq.(I.16) is reduced to:

$$\ddot{\theta} + \frac{g}{l}\theta = 0 \tag{I.17}$$

The solution of Eq.(I.17) is:

$$\theta(t) = \theta_0 \sin\left(\sqrt{\frac{g}{l}}t\right) \tag{I.18}$$

where $\theta_0$ is the amplitude of the oscillations. The period of the oscillation is therefore:

$$T_0 = 2\pi\sqrt{\frac{l}{g}} \tag{I.19}$$

For amplitude beyond the small angle approximation the period of the oscillation can be obtained from inverting Eq.(I.13).

$$\frac{dt}{d\theta} = \sqrt{\frac{l}{2g(\cos\theta - \cos\theta_0)}} \tag{I.20}$$

Integrating over a complete cycle and since:

$$T = t(\theta_0 \to 0 \to -\theta_0 \to 0 \to \theta_0) \tag{I.21.A}$$
$$T = 4t(\theta_0 \to 0) \tag{I.21.B}$$

yields that the period of oscillation is:

$$T = 4\sqrt{\frac{l}{2g}}\int_0^{\theta_0} \frac{d\theta}{\sqrt{\cos\theta - \cos\theta_0}} \tag{I.22}$$

The integral of Eq.(I.22) can be simplified as shown in Appendix AI.1 in:

$$T = 4\sqrt{\frac{l}{g}}K(k) \tag{I.23.A}$$

where $K(k)$ is the complete elliptic integral of the first kind defined as:

$$K(k) = \int_0^{\pi/2} \frac{1}{\sqrt{1 - k^2\sin^2 u}}\, du \tag{I.23.B}$$

and $k = \sin\frac{\theta_0}{2}$

The complete elliptic integral $K(k)$ cannot be solved analytically however it can be approximated with the use of Taylor series as shown in Appendix AI.2 as:

$$K(k) = \frac{\pi}{2}\sum_{n=0}^{\infty}\left(\frac{(2n-1)!!}{(2n)!!}k^n\right)^2 \tag{I.24}$$

Therefore, the period of the oscillation is obtained from:

$$T = 2\pi\sqrt{\frac{l}{g}}\sum_{n=0}^{\infty}\left(\frac{(2n-1)!!}{(2n)!!}\left(\sin\frac{\theta_0}{2}\right)^n\right)^2 \quad \text{(I.25)}$$

which can also be written as:

$$T = T_0\sum_{n=0}^{\infty}\left(\frac{(2n-1)!!}{(2n)!!}\left(\sin\frac{\theta_0}{2}\right)^n\right)^2 \quad \text{(I.26)}$$

It is interesting to show how the true period of the oscillation is different from the small angle period approximation with respect to the initial angle $\theta_0$. In Fig.I.5 the ratio of the true and small angle approximation period with respect to the initial angle is presented.

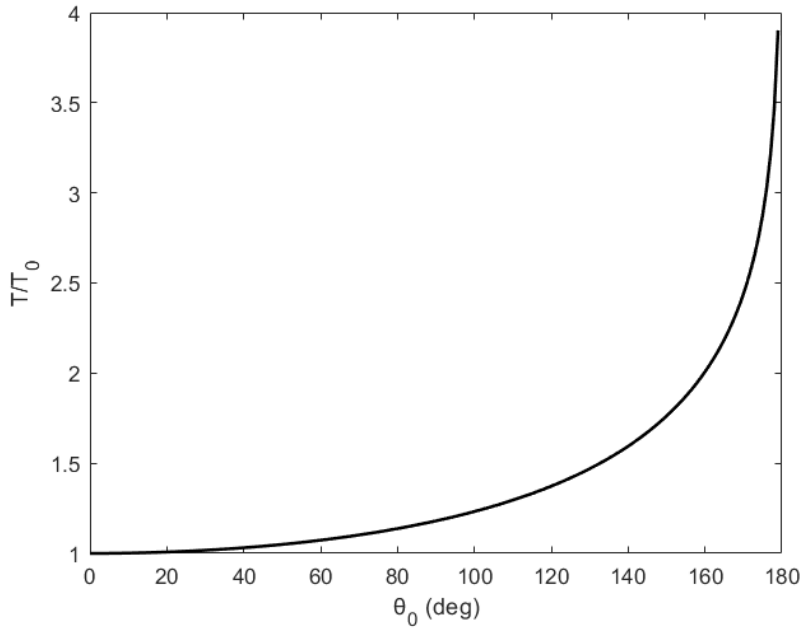


**Figure I.5: Ratio of the true and small angle approximation period with respect to the initial angle**

It can be observed that in small angles the approximation is accurate, however as the initial angle $\theta_0$ is increases the ratio increases and will tend to infinity if the angle approaches 180°.

In Fig.I.6 the oscillation of the pendulum with respect to time is presented at various initial angles. The length of the pendulum was considered to be 1m which yields to a small angle approximation period $T_0 \approx 2s$. Eq.(I.16) was solved using Simulink.

It can be observed, that in small angles (i.e. $\theta_0 = 10°$) the oscillation of the pendulum closely resembles a sine wave similar to the Eq.(I.18), while the period of the oscillation is approximately 2 seconds close to $T_0$.

However, as the initial angle increases the oscillation changes its behaviour and the period of the oscillation increases. In the extreme case were the initial angle is $\theta_0 = 179°$, the oscillation no longer resembles a sine wave especially near the angles $\pm\theta_0$. The period of the oscillation is almost 4 times higher than $T_0$ at around 8 seconds which can also be verified from Fig.I.5.

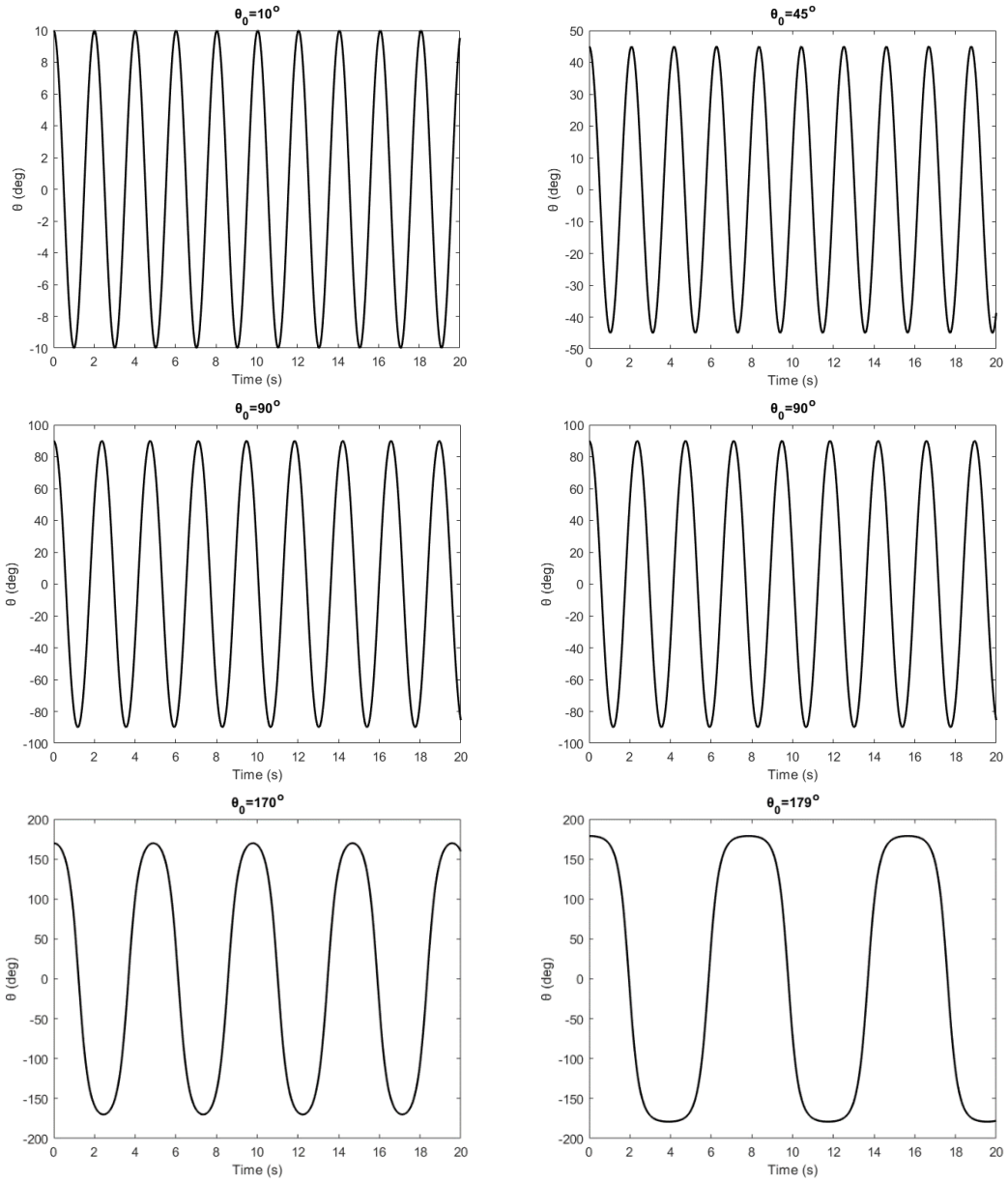


**Figure I.6: Oscillation of the pendulum with respect to time for various initial angles**

From the brief analysis of the simple pendulum it can be understood that even though the governing ordinary differential equations is relatively simple a very interesting

behaviour can be observed especially and large initial angles where the period of the oscillation and the oscillation itself has a very different behaviour when compared to small initial angles.

We will now consider a more general case of the simple pendulum the damped-driven pendulum, since the governing equations in coaxial magnetic gears resemble more the driven pendulum than the simple pendulum. The governing differential equation of the damped-driven pendulum is the following (from torque equilibrium in Fig.I.3):

$$\mathrm{mL}^2\ddot{\theta} + \mathrm{bL}^2\dot{\theta} + \mathrm{mgl}\sin\theta = \mathrm{FL}\cos(\Omega t) \tag{I.27}$$

where $\mathrm{m}$ is the mass of the bob, $\mathrm{b}$ is the damping coefficient due to air resistance, $\mathrm{F}$ is the amplitude of the forcing and $\Omega$ is the angular velocity of the forcing oscillations. Therefore, dividing Eq.(I.27) with $\mathrm{mL}^2$ the following non-dimensional form is derived:

$$\ddot{\theta} + 2\beta\dot{\theta} + \omega_0^2\sin\theta = \gamma\omega_0^2\cos(\Omega t) \tag{I.28.A}$$

where:

$$2\beta = \frac{\mathrm{b}}{\mathrm{m}} \tag{I.28.B}$$

$$\omega_0^2 = \frac{\mathrm{g}}{\mathrm{L}} \tag{I.28.C}$$

$$\gamma = \frac{\mathrm{F}}{\mathrm{mg}} \tag{I.28.D}$$

Eq.(I.28.A) exhibits chaotic behaviour [I.63]-[I.64]. The exact motion of this pendulum can only be found numerically and is highly dependent on the initial conditions. In order to understand chaotic behaviour a set of different case studies will be presented according to the parameters of Table I.2.

**Table I.2: Case study parameters**

| | |
|---|---|
| $\omega_0$ | 1.5 |
| $\beta$ | 0.375 |
| $\Omega$ | 1 |
| $\theta_0(t=0)$ | 0 |
| $\dot{\theta}_0(t=0)$ | 0 |

Different values of the non-dimensional force $\gamma$ will be given and the dynamical response of the pendulum will be calculated with Simulink.

In Fig.I.7 the oscillation of the damped-driven pendulum for various non-dimensional force $\gamma$ is presented.

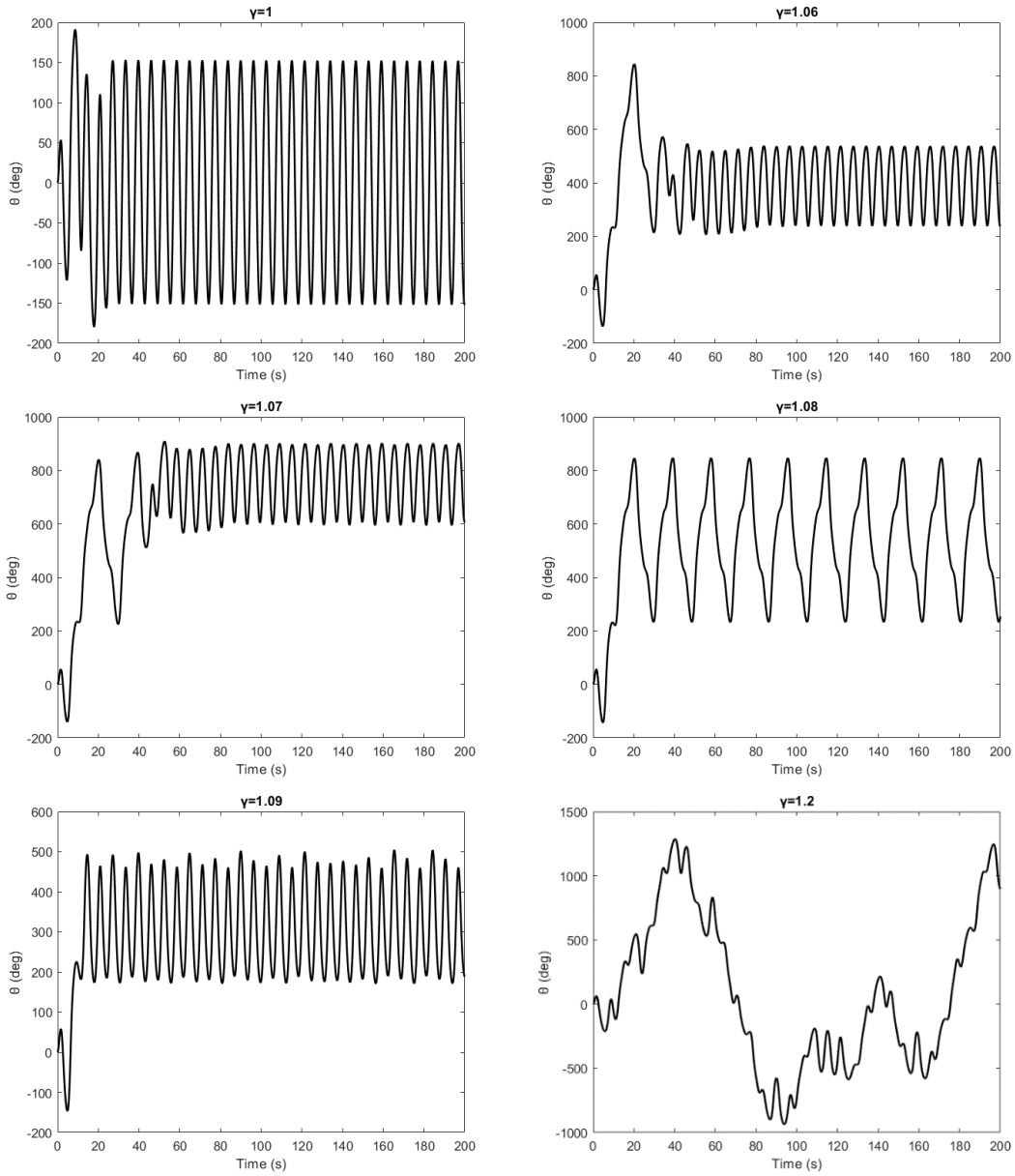


**Figure I.7: Oscillation of the damped-driven pendulum with respect to time for various non-dimensional force γ**

In most cases, some initial transients are present, however we are will focus our attention after the transient period. For the case of $\gamma = 1$, it can be observed that the pendulum oscillates with a period of approximately 5 seconds. A similar behaviour, is observed for the case of $\gamma = 1.06$, although the transient phenomenon is longer. However, for the case of $\gamma = 1.07$, after the initial transients we observe a period doubling. For the case of $\gamma = 1.08$, we observe that the period is four times larger than the case of $\gamma = 1.06$, while for the case of $\gamma = 1.08$, we observe that the period is eight times larger than the case of $\gamma = 1.06$. Finally for the case of $\gamma = 1.2$, we observe an aperiodic oscillation and chaotic behaviour.

An important phenomenon that is observed in all chaotic systems is that a small a very small change to the initial conditions of the system could lead to a very different dynamical responses of the system as the time progresses. In order to demonstrate

this phenomenon, the parameters of Table I.2 were used and a non-dimensional force $\gamma = 1.5$ was applied to system. In Fig.I.8 the dynamical response of the pendulum for different initial conditions is presented. It can be observed that initially the responses are very similar, however after some time they begin to showcase a small deviation that will eventually lead to a completely different behaviour.

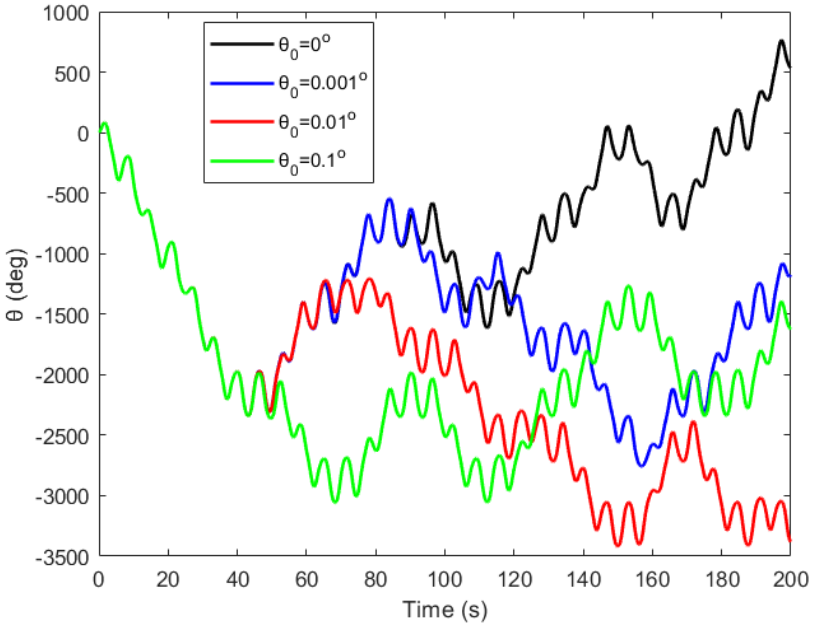


**Figure I.8: Oscillation of the damped-driven pendulum with respect to time for different initial conditions**

The different initial conditions are compared with the case when $\theta_0(t = 0) = 0°$. For the case of $\theta_0(t = 0) = 0.1°$, the two oscillations begin to deviate at around 45 seconds, for the case of $\theta_0(t = 0) = 0.01°$, the two oscillations begin to deviate at around 70 seconds while for the case of $\theta_0(t = 0) = 0.001°$ the two oscillations begin to differ at around 90 seconds.

As expected, when the initial conditions are closer to each other the deviation of the two oscillations requires more time. The amount of time for which the behaviour of a chaotic system can be effectively predicted depends on how accurately its current state can be measured, and a time scale depending on the dynamics of the system, called the Lyapunov time [I.61].

It is evident from the example of the damped-driven pendulum that chaotic behaviour in dynamical systems is a phenomenon that is hard to predict and could arise in simple physical phenomena. Therefore, a brief introduction in chaos theory is necessary in order to understand some fundamental principles that will be useful in the dynamical response study in coaxial magnetic gears.

### *I.3.2 The essence of chaos*

Chaos theory concerns deterministic systems whose behaviour can, in principle, be predicted. Chaotic systems are predictable for a while and then 'appear' to become random. Chaos theory states that within the apparent randomness of chaotic complex systems, there are underlying patterns, interconnection, constant feedback loops, repetition, self-similarity, fractals, and self-organization.

Small differences in initial conditions, such as those due to errors in measurements or due to rounding errors in numerical computation, can yield widely diverging outcomes for such dynamical systems, rendering long-term prediction of their behaviour impossible in general as seen in the case of the damped-driven pendulum and specifically in Fig.I.7. This can happen even though these systems are deterministic, meaning that their future behaviour follows a unique evolution and is fully determined by their initial conditions, with no random elements involved. In other words, the deterministic nature of these systems does not make them predictable. This behaviour is known as deterministic chaos, or simply chaos.

The theory was summarized by Edward Lorenz [I.62] as:

Chaos: When the present determines the future, but the approximate present does not approximately determine the future.

Chaotic behaviour exists in many natural systems, including fluid flow, heartbeat irregularities, weather, and climate. This behaviour can be studied through the analysis of a chaotic mathematical model, or through analytical techniques such as recurrence plots and Poincare maps.

One of the most well-known chaotic systems is the Lorenz system. In 1963 Edward Lorenz developed a simplified mathematical model for atmospheric convection [I.62].

$$\frac{dx}{dt} = \sigma(y - x) \tag{I.29.A}$$

$$\frac{dy}{dt} = x(\rho - z) - y \tag{I.29.B}$$

$$\frac{dz}{dt} = xy - \beta z \tag{I.29.C}$$

where $x$ is proportional to the rate of convection, $y$ to the horizontal temperature variation, and $z$ to the vertical temperature variation. The constants $\sigma$, $\rho$, and $\beta$ are system parameters proportional to the Prandtl number, Rayleigh number, and certain physical dimensions of the layer itself.

In order to investigate the chaotic behaviour of the Lorenz system a case study according to the parameters of Table I.3 will be considered

**Table I.3: Case study parameters**

| | |
|---|---|
| $\sigma$ | 10 |
| $\beta$ | 8/3 |
| $(x, y, z, t = 0)$ | (1,1,1) |

Different values of ρ will be given and the response of the system after 100 seconds will be calculated. In Fig.I.9 the solutions for different values of ρ are presented.

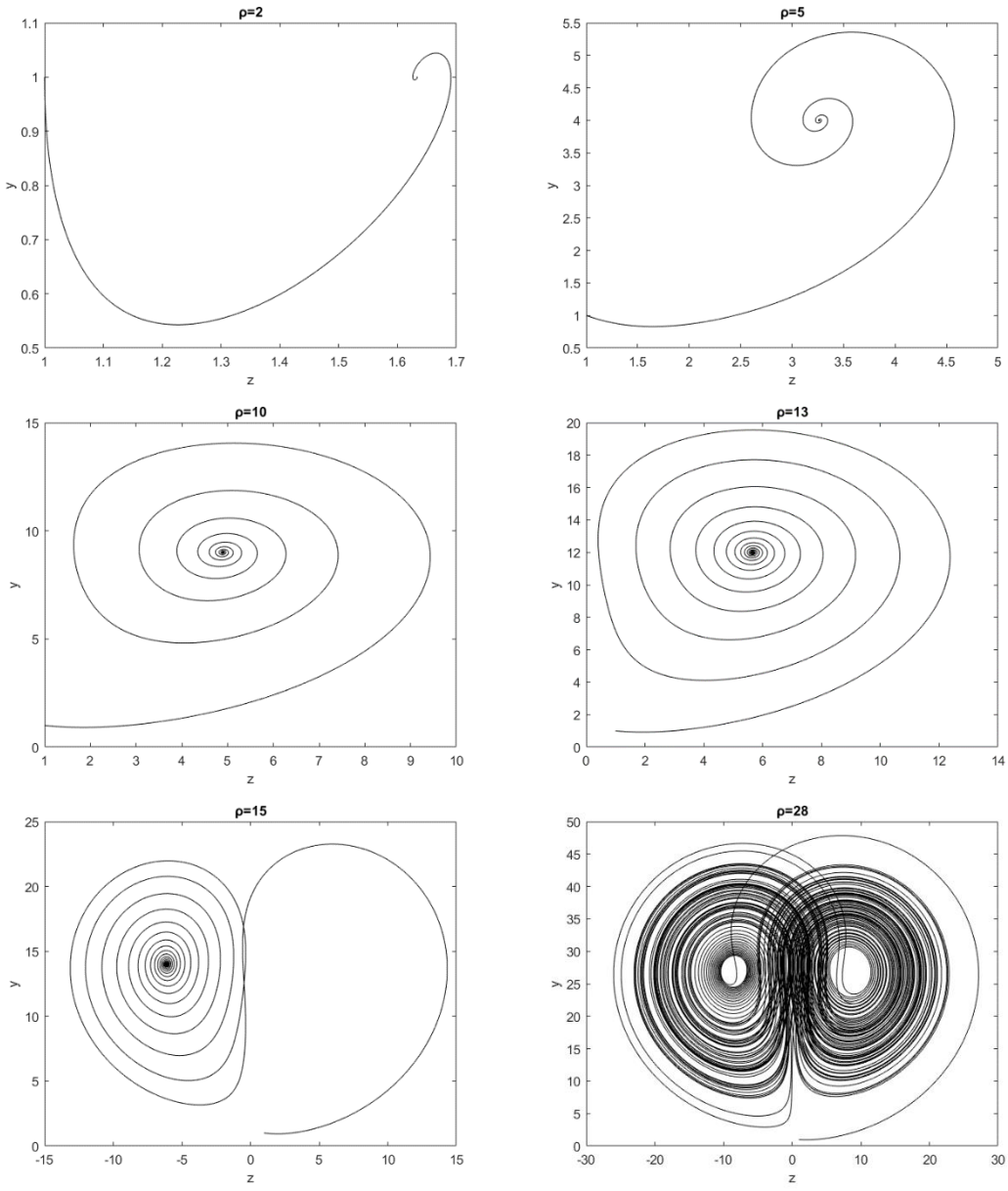


**Figure I.9: Lorenz solution for different values of ρ**

For small values of ρ the system is stable and evolves to one of two fixed point attractors. However, when ρ becomes large the fixed points become repulsors and the system trajectory is repelled by them in a very complex way. For $\rho = 28$, the

behaviour of the system is chaotic and almost all initial points will tend to an invariant set the Lorentz strange attractor.

One additional system that has chaotic behaviour, yet described by a very simple equation is the logistic map equation.

$$x_{n+1} = rx_n(1 - x_n) \tag{I.30}$$

where $x_n$ is a number between zero and one, which represents the ratio of existing population to the maximum possible population. This nonlinear difference equation is intended to capture two effects:

- reproduction, where the population will increase at a rate proportional to the current population when the population size is small
- starvation (density-dependent mortality), where the growth rate will decrease at a rate proportional to the value obtained by taking the theoretical "carrying capacity" of the environment less the current population.

The usual values of interest for the parameter $r$ are those in the interval [0, 4], so that $x_n$ remains bounded on [0, 1].

In Fig.I.10 the bifurcation diagram of the logistic map is presented. The horizontal axis shows the possible values of the parameter $r$ while the vertical axis shows the set of values of $x$ visited asymptotically from almost all initial conditions by the iterates of the logistic equation with that $r$ value.

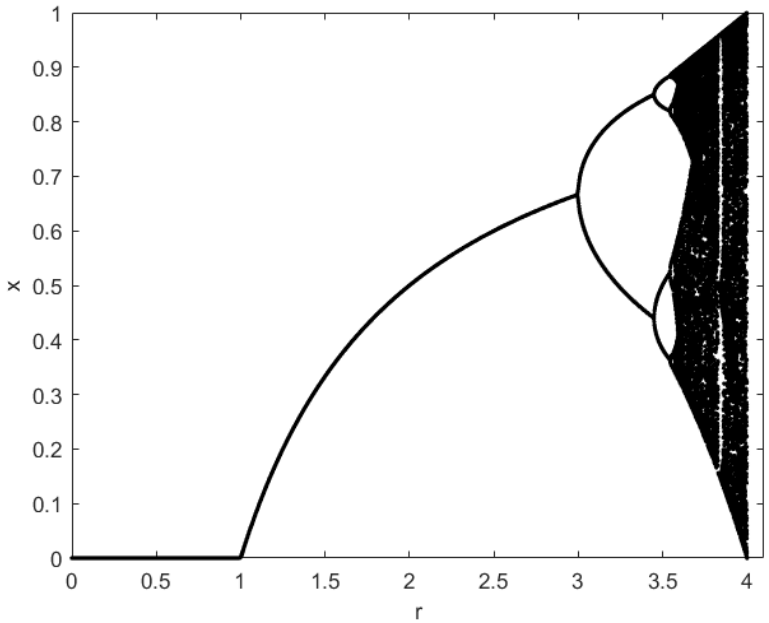


**Figure I.10: Bifurcation diagram of the logistic map for different values of $r$**

Bifurcation theory is the mathematical study of changes in the qualitative or topological structure of a given family of curves, such as the integral curves of a family

of vector fields, and the solutions of a family of differential equations. Most commonly applied to the mathematical study of dynamical systems, a bifurcation occurs when a small smooth change made to the parameter values (the bifurcation parameters) of a system causes a sudden 'qualitative' or topological change in its behaviour.

Bifurcations can be divided into two principal classes:

- Local bifurcations, which can be analysed entirely through changes in the local stability properties of equilibria, periodic orbits or other invariant sets as parameters cross through critical thresholds

- Global bifurcations, which often occur when larger invariant sets of the system 'collide' with each other, or with equilibria of the system. They cannot be detected purely by a stability analysis of the fixed points.

From Fig.I.10 it can be observed that after a certain value of $r$ the system will experience consecutive period doublings (at a rate according to the Feigenbaum constant) until chaotic behaviour emerges.

From the different dynamical systems presented it is evident that chaotic behaviour could arise even in simple mathematical and physical problems. The dynamical response of coaxial magnetic gears as will be demonstrated in Chapter 3 will showcase chaotic behaviour. Therefore, the understanding of chaos theory and its principles is important in order to investigate the fascinating dynamics that could arise during the operation of coaxial magnetic gears.

## *Appendix AI.1*

The integral of Eq.(I.22) can be simplified as follows:

Using the trigonometric identity:

$$\cos\theta = 1 - 2\sin^2\frac{\theta}{2}$$

we obtain:

$$T = 4\sqrt{\frac{l}{2g}}\int_0^{\theta_0}\frac{d\theta}{\sqrt{2}\sqrt{\sin^2\frac{\theta_0}{2} - \sin^2\frac{\theta}{2}}} \qquad (AI.\,1.1)$$

By letting:

$$\sin u = \frac{\sin\frac{\theta}{2}}{\sin\frac{\theta_0}{2}} \qquad (AI.\,1.2)$$

We obtain that:

$$\cos u\,du = \frac{\cos\frac{\theta}{2}d\theta}{2\sin\frac{\theta_0}{2}} \Rightarrow$$

$$2\sin\frac{\theta_0}{2}\cos u\,du = \sqrt{1 - \sin^2\frac{\theta}{2}}\,d\theta \Rightarrow$$

$$d\theta = \frac{2\sin\frac{\theta_0}{2}\cos u}{\sqrt{1 - \sin^2\frac{\theta_0}{2}\sin^2 u}}\,du \qquad (AI.\,1.3)$$

Therefore, the integral (AI.I.1) takes the following form:

$$T = 4\sqrt{\frac{l}{2g}}\int_0^{\pi/2}\frac{1}{\sqrt{2}\sqrt{\sin^2\frac{\theta_0}{2} - \sin^2\frac{\theta_0}{2}\sin^2 u}}\frac{2\sin\frac{\theta_0}{2}\cos u}{\sqrt{1 - \sin^2\frac{\theta_0}{2}\sin^2 u}}\,du \Rightarrow$$

$$T = 4\sqrt{\frac{l}{g}}\int_0^{\pi/2}\frac{\sin\frac{\theta_0}{2}\cos u}{\sin\frac{\theta_0}{2}\sqrt{1 - \sin^2 u}}\frac{1}{\sqrt{1 - \sin^2\frac{\theta_0}{2}\sin^2 u}}\,du \Rightarrow$$

$$T = 4\sqrt{\frac{l}{g}}\int_0^{\pi/2} \frac{1}{\sqrt{1-\sin^2\frac{\theta_0}{2}\sin^2 u}}\,du \Rightarrow$$

$$T = 4\sqrt{\frac{l}{g}}K(k) \qquad (AI.\,1.4)$$

where $K(k)$ is the complete elliptic integral of the first kind defined as:

$$K(k) = \int_0^{\frac{\pi}{2}} \frac{1}{\sqrt{1-k^2\sin^2 u}}\,du \qquad (AI.\,1.5)$$

and $k = \sin\frac{\theta_0}{2}$

## *Appendix AI.2*

In order to approximate the complete elliptic integral of the first kind:

$$K(k) = \int_0^{\frac{\pi}{2}} \frac{1}{\sqrt{1 - k^2 \sin^2 u}}\, du \qquad (AI.\ 2.1)$$

We will evaluate the Taylor series expansion of the following function:

$$f(x) = (1 - x)^{\frac{1}{2}} \qquad (AI.\ 2.2)$$

where

$$x = k^2 \sin^2 u \qquad (AI.\ 2.3)$$

It relatively easy to show that the $n^{th}$ derivative of f will have the following form:

$$f^{(n)}(x) = \frac{(2n-1)!!}{2^n}(1 - x)^{-\frac{2n-1}{2}}$$

where $n!!$ denotes the double factorial and

$$f^{(n)}(0) = \frac{(2n-1)!!}{2^n}$$

Therefore, the Taylor series expansion will have the following form:

$$f(x) = \sum_{n=0}^{\infty} \frac{(2n-1)!!}{n!\, 2^n} x^n \qquad (AI.\ 2.4)$$

Therefore the complete elliptic integral (AI.2.1) take the following form:

$$K(k) = \int_0^{\pi/2} \sum_{n=0}^{\infty} \frac{(2n-1)!!}{n!\, 2^n} k^{2n} \sin^{2n} u\ du \Rightarrow$$

$$K(k) = \sum_{n=0}^{\infty} \frac{(2n-1)!!}{n!\, 2^n} k^{2n} \int_0^{\frac{\pi}{2}} \sin^{2n} u\ du \qquad (AI.\ 2.5)$$

since the series converges. Therefore, the complete elliptic integral has the following form:

$$K(k) = \sum_{n=0}^{\infty} \frac{(2n-1)!!}{n!\, 2^n} k^{2n} I \qquad (AI.\ 2.6)$$

where I is:

$$I = \int_0^{\pi/2} \sin^{2n} u\ du \qquad (AI.\ 2.7)$$

The integral I can be calculated with the use of betta and gamma function.

$$B(x,y) = \frac{\Gamma(x)\Gamma(y)}{\Gamma(x+y)} = 2\int_0^{\pi/2} \sin^{2x-1} t \cos^{2y-1} t \; dt \qquad (AI.\,2.8)$$

which yields that:

$$I = \frac{\Gamma\left(\frac{2n+1}{2}\right)\Gamma(\frac{1}{2})}{2\Gamma(n+1)} \qquad (AI.\,2.9)$$

By definition:

$$\Gamma\left(\frac{1}{2}\right) = \sqrt{\pi} \qquad (AI.\,2.10)$$

$$\Gamma(n+1) = n! \qquad (AI.\,2.11)$$

In order to calculate $\Gamma\left(\frac{2n+1}{2}\right)$ we use the following property of the gamma function

$$\Gamma(n+1) = n\Gamma(n)$$

and since $\Gamma\left(\frac{1}{2}\right) = \sqrt{\pi}$ we obtain:

$$\Gamma\left(\frac{2n+1}{2}\right) = \frac{\sqrt{\pi}(2n-1)!!}{2^n} \qquad (AI.\,2.12)$$

and a consequence:

$$I = \frac{1}{2}\frac{\frac{\pi(2n-1)!!}{2^n}}{n!} \Rightarrow$$

$$I = \frac{\pi}{2}\frac{(2n-1)!!}{2^n n!} \qquad (AI.\,2.13)$$

Furthermore, since

$$n!\,2^n = (2n)!!$$

We obtain that the complete elliptic integral can be approximated by the following formula:

$$K(k) = \frac{\pi}{2}\sum_{n=0}^{\infty}\left(\frac{(2n-1)!!}{(2n)!!}k^n\right)^2 \qquad (AI.\,2.14)$$

## *Introduction-References*

[I.1] Wang, Y., Filippini, M., Bianchi, N., & Alotto, P. (2019). A review on magnetic gears: Topologies, computational models, and design aspects. IEEE Transactions on Industry Applications, 55(5), 4557-4566.

[I.2] Praslicka, B., Gardner, M. C., Johnson, M., & Toliyat, H. A. (2021). Review and analysis of coaxial magnetic gear pole pair count selection effects. *IEEE Journal of Emerging and Selected Topics in Power Electronics*, *10*(2), 1813-1822.

[I.3] Asnani, V., Scheidler, J., & Tallerico, T. F. (2018, May). Magnetic gearing research at NASA. In *American Helicopter Society International Annual Forum & Technology Display* (No. GRC-E-DAA-TN54810).

[I.4] Scheidler, J. J., Asnani, V. M., & Tallerico, T. F. (2018, July). NASA's magnetic gearing research for electrified aircraft propulsion. In *2018 AIAA/IEEE Electric Aircraft Technologies Symposium (EATS)* (pp. 1-12). IEEE.

[I.5] Tallerico, T. F., Cameron, Z. A., Scheidler, J. J., & Hasseeb, H. (2020, August). Outer stator magnetically-geared motors for electrified urban air mobility vehicles. In *2020 AIAA/IEEE Electric Aircraft Technologies Symposium (EATS)* (pp. 1-25). IEEE.

[I.6] Kjaer, A. B., Korsgaard, S., Nielsen, S. S., Demsa, L., & Rasmussen, P. O. (2019). Design, fabrication, test, and benchmark of a magnetically geared permanent magnet generator for wind power generation. *IEEE Transactions on Energy Conversion*, *35*(1), 24-32.

[I.7] Li, K., Modaresahmadi, S., Williams, W. B., Wright, J. D., Som, D., & Bird, J. Z. (2019). Designing and experimentally testing a magnetic gearbox for a wind turbine demonstrator. *IEEE Transactions on Industry Applications*, *55*(4), 3522-3533.

[I.8] Li, K., Modaresahmadi, S., Williams, W. B., Bird, J. Z., Wright, J. D., & Barnett, D. (2019). Electromagnetic analysis and experimental testing of a flux focusing wind turbine magnetic gearbox. *IEEE Transactions on Energy Conversion*, *34*(3), 1512-1521.

[I.9] Klimina, L., Dosaev, M., & Selyutskiy, Y. (2017). Asymptotic analysis of the mathematical model of a wind-powered vehicle. *Applied Mathematical Modelling*, *46*, 691-697.

[I.10] Johnson, M., Gardner, M. C., Toliyat, H. A., Englebretson, S., Ouyang, W., & Tschida, C. (2018). Design, construction, and analysis of a large-scale inner stator radial flux magnetically geared generator for wave energy conversion. *IEEE Transactions on Industry Applications*, *54*(4), 3305-3314.

[I.11] Frandsen, T. V., Rasmussen, P. O., & Jensen, K. K. (2012, September). Improved motor intergrated permanent magnet gear for traction applications. In *2012 IEEE Energy Conversion Congress and Exposition (ECCE)* (pp. 3332-3339). IEEE.

[I.12] Esnoz-Larraya, J., Valiente-Blanco, I., Cristache, C., Sanchez-Garcia-Casarrubios, J., Rodriguez-Celis, F., Diez-Jimenez, E., & Perez-Diaz, J. L. (2017). Optimagdrive: High-performance magnetic gears development for space applications. *Proceedings of the ESMATS*.

[I.13] Armstrong, C. G. (1901). Power transmitting device. Unites States Patent Office, No. 687, 292, 26^.

[I.14] H. Faus, “Magnet gearing,” May 27 1941, US Patent 2,243,555.

[I.15] Martin Jr, T. B. (1968). Magnetic transmission. US Pat. 3378710.

[I.16] Atallah, K., & Howe, D. (2001). A novel high-performance magnetic gear. *IEEE Transactions on magnetics*, *37*(4), 2844-2846.

[I.17] Huang, C. C., Tsai, M. C., Dorrell, D. G., & Lin, B. J. (2008). Development of a magnetic planetary gearbox. IEEE transactions on magnetics, 44(3), 403-412.

[I.18] Jørgensen, F. T., Andersen, T. O., & Rasmussen, P. O. (2006, October). The cycloid permanent magnetic gear. In Conference Record of the 2006 IEEE Industry Applications Conference Forty-First IAS Annual Meeting (Vol. 1, pp. 373-378). IEEE.

[I.19] Rens, J., Atallah, K., Calverley, S. D., & Howe, D. (2009). A novel magnetic harmonic gear. IEEE Transactions on Industry Applications, 46(1), 206-212.

[I.20] Pakdelian, S., Frank, N. W., & Toliyat, H. A. (2012, September). Analysis and design of the trans-rotary magnetic gear. In 2012 IEEE Energy Conversion Congress and Exposition (ECCE) (pp. 3340-3347). IEEE.

[I.21] Atallah, K., Calverley, S. D., & Howe, D. (2004). Design, analysis and realisation of a high-performance magnetic gear. IEE Proceedings-Electric Power Applications, 151(2), 135-143.

[I.22] Gouda, E., Mezani, S., Baghli, L., & Rezzoug, A. (2010). Comparative study between mechanical and magnetic planetary gears. IEEE transactions on magnetics, 47(2), 439-450.

[I.23] Matthee, A., Gerber, S., & Wang, R. J. (2015, January). A high performance concentric magnetic gear. In Proc. Southern Afr. Univ. Power Eng. Conf. (pp. 203-207).

[I.24] Rasmussen, P. O., Andersen, T. O., Jorgensen, F. T., & Nielsen, O. (2005). Development of a high-performance magnetic gear. IEEE transactions on industry applications, 41(3), 764-770.

[I.25] Uppalapati, K., & Bird, J. (2012, March). A flux focusing ferrite magnetic gear. In 6th IET International Conference on Power Electronics, Machines and Drives (PEMD 2012) (pp. 1-6). IET.

[I.26] Uppalapati, K. K., & Bird, J. Z. (2014). An iterative magnetomechanical deflection model for a magnetic gear. IEEE Transactions on Magnetics, 50(2), 245-248.

[I.27] Uppalapati, K. K., Calvin, M. D., Wright, J. D., Pitchard, J., Williams, W. B., & Bird, J. Z. (2017). A magnetic gearbox with an active region torque density of 239 N· m/L. IEEE Transactions on Industry Applications, 54(2), 1331-1338.

[I.28] Frank, N. W., & Toliyat, H. A. (2011). Analysis of the concentric planetary magnetic gear with strengthened stator and interior permanent magnet inner rotor. IEEE transactions on industry applications, 47(4), 1652-1660.

[I.29] Liu, X., Chau, K. T., Jiang, J. Z., & Yu, C. (2009). Design and analysis of interior-magnet outer-rotor concentric magnetic gears. Journal of applied physics, 105(7).

[I.30] Jian, L., & Chau, K. T. (2010). A coaxial magnetic gear with Halbach permanent-magnet arrays. IEEE Transactions on Energy conversion, 25(2), 319-328.

[I.31] Scheidler, J. J., Asnani, V. M., & Tallerico, T. F. (2018, July). NASA's magnetic gearing research for electrified aircraft propulsion. In 2018 AIAA/IEEE Electric Aircraft Technologies Symposium (EATS) (pp. 1-12). IEEE.

[I.32] Fujita, T., Ando, Y., Nagaya, K., Oka, M., Todaka, T., Enokizono, M., & Sugiura, K. (2013). Surface magnet gears with a new magnet arrangement and optimal shape of stationary pole pieces.

[I.33] Gardner, M. C., Janak, D. A., & Toliyat, H. A. (2018, September). A parameterized linear magnetic equivalent circuit for air core radial flux coaxial magnetic gears with Halbach arrays. In 2018 IEEE Energy Conversion Congress and Exposition (ECCE) (pp. 2351-2358). IEEE.

[I.34] Aiso, K., Akatsu, K., & Aoyama, Y. (2019). A novel reluctance magnetic gear for high-speed motor. IEEE Transactions on Industry Applications, 55(3), 2690-2699.

[I.35] Abdel-Khalik, A. S., Ahmed, S., & Massoud, A. (2014). A bearingless coaxial magnetic gearbox. Alexandria Engineering Journal, 53(3), 573-582.

[I.36] Liu, Y., Ho, S. L., & Fu, W. N. (2014). A novel magnetic gear with intersecting axes. IEEE Transactions on Magnetics, 50(11), 1-4.

[I.37] Mezani, S., Atallah, K., & Howe, D. (2006). A high-performance axial-field magnetic gear. Journal of applied physics, 99(8).

[I.38] Johnson, M., Gardner, M. C., & Toliyat, H. A. (2015, May). Analysis of axial field magnetic gears with Halbach arrays. In 2015 IEEE International Electric Machines & Drives Conference (IEMDC) (pp. 108-114). IEEE.

[I.39] Tsai, M. C., & Ku, L. H. (2015). 3-D printing-based design of axial flux magnetic gear for high torque density. IEEE transactions on magnetics, 51(11), 1-4.

[I.40] Yin, X., Pfister, P. D., & Fang, Y. (2015). A novel magnetic gear: toward a higher torque density. IEEE Transactions on Magnetics, 51(11), 1-4.

[I.41] Peng, S., Fu, W. N., & Ho, S. L. (2014). A novel triple-permanent-magnet-excited hybrid-flux magnetic gear and its design method using 3-D finite element method. IEEE Transactions on Magnetics, 50(11), 1-4.

[I.42] Atallah, K., Wang, J., & Howe, D. (2005). A high-performance linear magnetic gear. Journal of Applied Physics, 97(10).

[I.43] Li, W., Chau, K. T., & Li, J. (2010). Simulation of a tubular linear magnetic gear using HTS bulks for field modulation. IEEE Transactions on Applied Superconductivity, 21(3), 1167-1170.

[I.44] Li, K., & Bird, J. Z. (2018, September). A review of the volumetric torque density of rotary magnetic gear designs. In 2018 XIII International Conference on Electrical Machines (ICEM) (pp. 2016-2022). IEEE.

[I.45] Zhang, X., Liu, X., Wang, C., & Chen, Z. (2014). Analysis and design optimization of a coaxial surface-mounted permanent-magnet magnetic gear. *Energies*, *7*(12), 8535-8553.

[I.46] Neves, C. G. C., & Flores, Á. F. (2014, October). Coaxial magnetic gear analysis and optimization. In *2014 International Conference on Renewable Energy Research and Application (ICRERA)* (pp. 91-97). IEEE.

[I.47] Filippini, M., & Alotto, P. (2017). Coaxial magnetic gear design and optimization. *IEEE Transactions on Industrial Electronics*, *64*(12), 9934-9942.

[I.48] Gardner, M. C., Praslicka, B., Johnson, M., & Toliyat, H. A. (2021). Optimization of coaxial magnetic gear design and magnet material grade at different temperatures and gear ratios. *IEEE Transactions on Energy Conversion*, *36*(3), 2493-2501.

[I.49] Zhu, Z. Q., & Howe, D. (2000). Influence of design parameters on cogging torque in permanent magnet machines. *IEEE Transactions on energy conversion*, *15*(4), 407-412.

[I.50] Jian, L., & Chau, K. T. (2009). Analytical calculation of magnetic field distribution in coaxial magnetic gears. *Progress In Electromagnetics Research*, *92*, 1-16.

[I.51] Jian, L., Deng, Z., Shi, Y., Wei, J., & Chan, C. C. (2019). The mechanism how coaxial magnetic gear transmits magnetic torques between its two rotors: Detailed analysis of torque distribution on modulating ring. *IEEE/ASME Transactions on Mechatronics*, *24*(2), 763-773.

[I.52] Niguchi, N., & Hirata, K. (2011). Cogging torque analysis of magnetic gear. *IEEE transactions on industrial electronics*, *59*(5), 2189-2197.

[I.53] Liu, X., Zhao, Y., Zhang, X., Gao, J., & Huang, S. (2017, August). Investigation of the dynamic characteristics of a coaxial magnetic gear under loading condition based on analytical model. In *2017 20th International Conference on Electrical Machines and Systems (ICEMS)* (pp. 1-5). IEEE.

[I.54] Chau, K. T., Zhang, D., Jiang, J. Z., & Jian, L. (2008). Transient analysis of coaxial magnetic gears using finite element comodeling. *Journal of Applied Physics*, *103*(7), 07F101.

[I.55] Wu, Y. C., & Jian, B. S. (2015). Magnetic field analysis of a coaxial magnetic gear mechanism by two-dimensional equivalent magnetic circuit network method and finite-element method. *Applied Mathematical Modelling*, *39*(19), 5746-5758.

[I.56] Tsurumoto, K., & Kikuchi, S. (1987). A new magnetic gear using permanent magnet. *IEEE Transactions on Magnetics*, *23*(5), 3622-3624.

[I.57] Frandsen, T. V., & Rasmussen, P. O. (2015, October). Slip torque investigation and magnetic redesign of motor integrated permanent magnet gear. In *2015 18th International Conference on Electrical Machines and Systems (ICEMS)* (pp. 929-935). IEEE.

[I.58] Montague, R., Bingham, C., & Atallah, K. (2011). Servo control of magnetic gears. *IEEE/Asme Transactions on Mechatronics*, *17*(2), 269-278.

[I.59] Montague, R. G., Bingham, C., & Atallah, K. (2012). Magnetic gear pole-slip prevention using explicit model predictive control. *IEEE/ASME Transactions on Mechatronics*, *18*(5), 1535-1543.

[I.60] Desvaux, M., Multon, B., Sire, S., & Ahmed, H. B. (2017, May). Analytical iron loss model for the optimization of magnetic gear. In 2017 IEEE International Electric Machines and Drives Conference (IEMDC) (pp. 1-8). IEEE.

[I.61] Strogatz, S. H. (2018). Nonlinear dynamics and chaos with student solutions manual: With applications to physics, biology, chemistry, and engineering. CRC press.

[I.62] Lorenz, E. N., & Haman, K. (1996). The essence of chaos. Pure and Applied Geophysics, 147(3), 598-599.

[I.63] Hastings, S. P., & McLeod, J. B. (1993). Chaotic motion of a pendulum with oscillatory forcing. The American mathematical monthly, 100(6), 563-572.

[I.64] Van Dooren, R. (1996). Chaos in a pendulum with forced horizontal support motion: a tutorial. Chaos, Solitons & Fractals, 7(1), 77-90.

# 1 2D Analytical Modelling of Coaxial Magnetic Gears

## 1.1 Magnetic Potential Calculation

The Coaxial Magnetic Gear (CMG) consists of three parts: the inner rotor, the outer rotor and the flux modulator ring. The modulator ring consists of N ferromagnetic segments, where:

$$N = p_{in} + p_{out} \tag{1.1}$$

The CMG could operate with two different alternatives. Without loss of generality it is considered that the inner rotor is the input of the system (clockwise rotation). In the first case of operation (Case A), the modulator ring is fixed and outer rotor is free to rotate (counter-clockwise), while in the second case (Case B) the outer rotor is fixed and the modulator ring is free to rotate (clockwise). The equivalent gear ratio is:

$$i_A = \frac{p_{out}}{p_{in}}, \text{ Case A} \tag{1.2}$$

$$i_B = \frac{N}{p_{in}} = i_A + 1 \text{ , Case B} \tag{1.3}$$

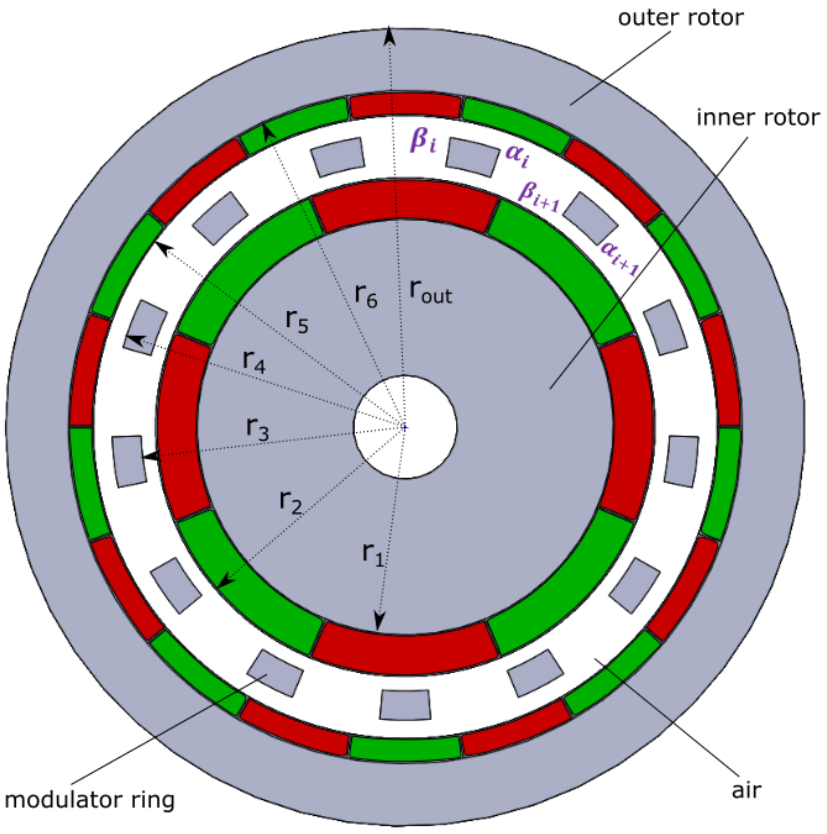


**Figure 1.1: Coaxial Magnetic Gear**

In the standard CMG, the polarity of the two rotor's PMs is alternating. As presented in Fig. 1.1, $r_1, r_2, r_3, r_4, r_5, r_6, r_{out}$ are the radii of the inner iron yoke, the inner PMs, the inner modulator ring's side, the outer modulator ring's side, the outer PMs, the outer iron yoke and the outer side of the CMG respectively. In addition, $\alpha_j$ and $\beta_j$ are the right and left border of the $j^{th}$ ferromagnetic segment.

The analytical model that will be developed, neglects edge effect phenomena in the CMG, and thus is a 2D model that assumes infinite length. The developed model can only be derived assuming cylindrical sector geometries in all the parts of the CMG. Furthermore, the magnetic materials are assumed to be linear, while infinite permeability of the iron yokes and the ferromagnetic segments is considered [1.1].

The total magnetic induction created by the permanent magnets (PMs) can be calculated as a superposition of the magnetic inductions created by the PMs of each rotor separately [1.1]. Therefore, two models are constructed: one without the outer rotor's magnets and one without the inner rotor's magnets.

The fundamental equations used to develop the analytical model are the Maxwell's equations (Gauss and Ampere Law):

$$\nabla \cdot \mathbf{B} = 0 \tag{1.4}$$

$\nabla \times \mathbf{H} = 0$ , since no currents are present (1.5)

where **B** is the magnetic induction vector and **H** is the magnetic field intensity vector. As a consequence, **H** can be written in the following form:

$$\mathbf{H} = -\nabla\varphi \tag{1.6}$$

where $\varphi$ is the scalar magnetic potential

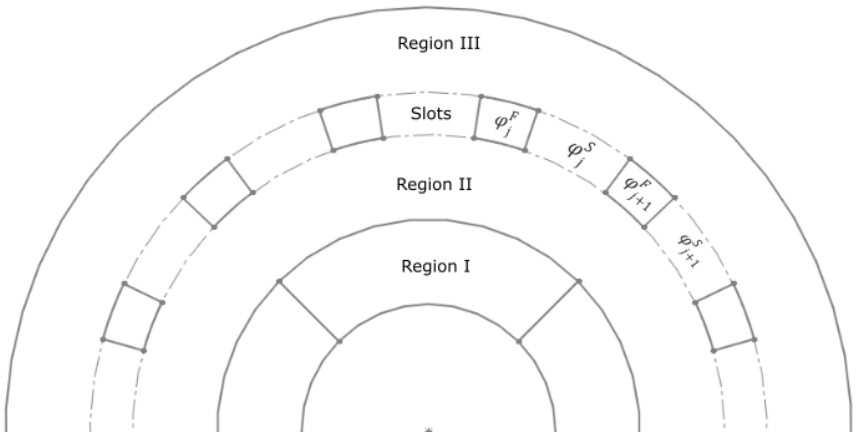


**Figure 1.2: Regions of the analytical model**

In Fig. 1.2, the first model -without the outer rotor's PMs- is illustrated. Region I represents the PMs of the inner rotor, Region II is the airgap below the modulator ring and Region III is the space between the above side of the modulator ring and the outer rotor's back iron. The correlation of the magnetic induction vector and the magnetic field intensity vector, in each region can be expressed as:

$$\mathbf{B} = \mu_0\mu_r\mathbf{H} + \mu_0\mathbf{M}\,, \qquad \text{in Region I} \tag{1.7}$$

$$\mathbf{B} = \mu_0\mathbf{H} \qquad \text{in Region II, III and slots} \tag{1.8}$$

where $\mu_0$ is the vacuum permeability, $\mu_r$ is the relative permeability of the PMs and $\mathbf{M}$ is the residual magnetization vector of the PMs.

From Eq. (1.4)-(1.8) the partial differential equation (PDE) can be obtained for each region:

$$\nabla^2\varphi^{I}(r,\theta) = \frac{\mathrm{div}\mathbf{M}}{\mu_r} \qquad \text{in Region I} \tag{1.9}$$

$$\nabla^2\varphi^{II,III}(r,\theta) = 0 \qquad \text{in Regions II, III} \tag{1.10}$$

$$\nabla^2\varphi^{S}(r,\theta) = 0 \qquad \text{in the slots} \tag{1.11}$$

The PDE in the Regions $II, III$ can be solved as follows as shown in more detail in Appendix A1.1:

$$\varphi^{II}(r,\theta) = \sum_{n=1}^{\infty}[(E_n r^n + F_n r^{-n})\cos(n\theta) + (G_n r^n + H_n r^{-n})\sin(n\theta)] + E_0 \ln r + F_0 \tag{1.12}$$

$$\varphi^{III}(r,\theta) = \sum_{n=1}^{\infty}[(I_n r^n + J_n r^{-n})\cos(n\theta) + (K_n r^n + L_n r^{-n})\sin(n\theta)] + I_0 \ln r + J_0 \tag{1.13}$$

The solution of the PDE in the slots, although is similar to the PDE in the Regions II and III that has been solved above, cannot be solved with the method of the separation of variables, since the boundary conditions are not zero. Therefore, the PDE can be solved as a sum of two solutions:

$$\varphi^{S}(r,\theta) = \varphi_1(\theta) + \varphi_2(r,\theta) \tag{1.14}$$

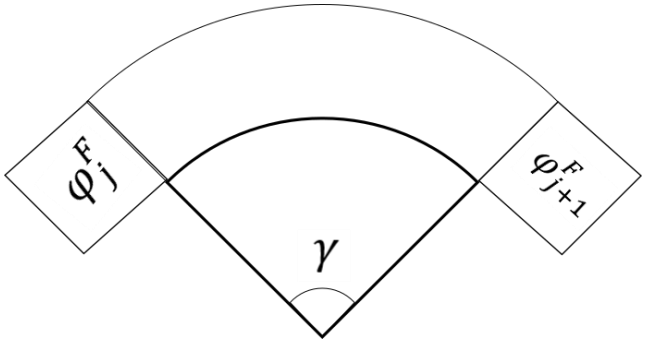


**Figure 1.3: Boundary conditions in the slot region**

Where $\varphi_{j+1}^F$ and $\varphi_j^F$ are the magnetic potential of the two consecutive ferromagnetic segments, $a_j$ is the global angle of $\varphi_j^F$ and $\gamma$ is the central angle between the ferromagnetic segments as shown in Fig. 1.3.

$\varphi_1$ derives from linear interpolation between $\varphi_j^F$ and $\varphi_{j+1}^F$:

$$\varphi_1(\theta) = \frac{\varphi_{j+1}^F - \varphi_j^F}{\gamma}\left(\theta - \alpha_j\right) + \varphi_j^F \tag{1.15}$$

Therefore, the PDE for $\varphi_2(r,\theta)$ is:

$$\nabla^2\varphi_2(r,\theta) = 0 \tag{1.16}$$

and the boundary conditions are as shown in Fig.1.4:

$$\varphi_j^F = 0 \tag{1.17}$$

$$\varphi_{j+1}^F = 0 \tag{1.18}$$

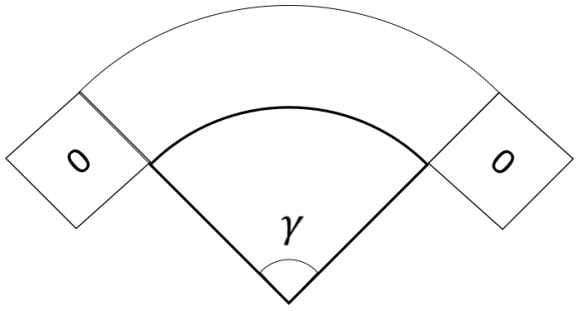


**Figure 1.4: Zero Boundary conditions for $\varphi_2$ in the slot region**

The system of Eq.(1.16)-(1.18) can be solved with the separation of variables method that yields the following:

$$r^2R'' + rR' - \lambda R = 0 \tag{1.19}$$

$$\Theta'' + \frac{n\pi}{\gamma}\Theta = 0 \tag{1.20}$$

From the boundary conditions: $\Theta(0) = \Theta(\gamma) = 0$

Which yields that the general solution of Eq.(1.16) is:

$$\varphi_2(r,\theta) = \sum_{n=1}^{\infty}\left(X_n r^{\frac{n\pi}{\gamma}} + Y_n r^{-\frac{n\pi}{\gamma}}\right)\sin\left(\frac{n\pi}{\gamma}(\theta-\alpha_j)\right) \tag{1.21}$$

Therefore, the general solution of the magnetic potential in the slots is:

$$\varphi^S(r,\theta) = \frac{\varphi_{j+1}^F - \varphi_j^F}{\gamma}(\theta-\alpha_j) + \varphi_j^F + \sum_{n=1}^{\infty}\left(X_{jn} r^{\frac{n\pi}{\gamma}} + Y_{jn} r^{-\frac{n\pi}{\gamma}}\right)\sin\left(\frac{n\pi}{\gamma}(\theta-\alpha_j)\right) \tag{1.22}$$

The scalar magnetic potential $\varphi$ is governed by the Poisson equation in Region I. According to the superposition principle, the solution of the Poisson equation in Region I consists of the general solution of the Laplace equation (the same as the Regions II, III) and a special solution. In order to obtain the special solution, the magnetization distribution, shown in Fig.1.5, should be expressed in an analytical and continuous function [1.1].

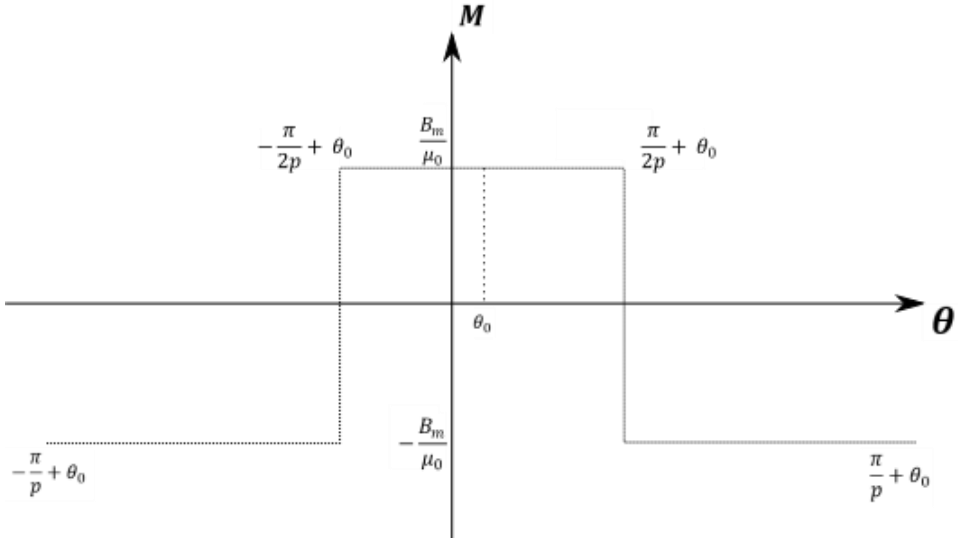


**Figure 1.5: Magnetization distribution in Region I**

where p is the number of pole pairs, $\theta_0$ is the angle of rotation of the inner rotor and $B_m$ is the residual magnetism of the PM.

The magnetization vector can be written as follows:

$$\mathbf{M} = M_r\mathbf{r} + M_\theta\boldsymbol{\theta} \tag{1.23}$$

with $M_\theta = 0$ (since no tangential component of the magnetization is present).

The magnetization can be described in an analytical and continuous form with Fourier series as shown in Appendix A1.2 as:

$$M_r(\theta) = \sum_{k=1}^{\infty} M_k[\cos(pk\theta_0)\cos(pk\theta) + \sin(pk\theta_0)\sin(pk\theta)] \tag{1.24}$$

where :

$$M_k = \frac{4B_m}{\pi\mu_0 k}\sin\left(\frac{k\pi}{2}\right) \tag{1.25}$$

Therefore:

$$\frac{\mathrm{div}\mathbf{M}}{\mu_r} = \frac{1}{\mu_r}\left[\frac{1}{r}\frac{\partial}{\partial r}(rM_r) + \frac{1}{r}\frac{\partial}{\partial\theta}(M_\theta)\right] = \frac{M_r(\theta)}{\mu_r r} \tag{1.26}$$

As a result, the PDE of Region I is:

$$\varphi_{rr} + \frac{1}{r}\varphi_r + \frac{1}{r^2}\varphi_{\theta\theta} = \frac{M_r(\theta)}{\mu_r r} \tag{1.27}$$

The special solution of Eq.(1.27) will have the following form:

$$\varphi_s(r,\theta) = \sum_{k=1}^{\infty} W_k(r)[\cos(pk\theta_0)\cos(pk\theta) + \sin(pk\theta_0)\sin(pk\theta)] \tag{1.28}$$

Therefore Eq.(1.27) takes the following form:

$$\ddot{W}_k(r) + \frac{1}{r}\dot{W}_k(r) - \frac{(pk)^2}{r^2}W_k(r) = \frac{M_k}{\mu_r} \tag{1.29}$$

The solution of Eq.(1.29) is:

$$W_k(r) = \begin{cases} \dfrac{M_k r}{\mu_r(1-(pk)^2)}, & \text{if } pk \neq 1 \\ \dfrac{M_1 r \ln r}{2\mu_r}, & \text{if } p = k = 1 \end{cases} \tag{1.30}$$

In order to obtain a more compact solution of the general PDE in Region I we let $pk = n$. Therefore:

$$\varphi_s(r,\theta) = \sum_{n=1}^{\infty} W_n(r)[\cos(n\theta_0)\cos(n\theta) + \sin(n\theta_0)\sin(n\theta)] \tag{1.31}$$

where:

$$W_n(r) = \begin{cases} \dfrac{M_n r}{\mu_r(1-n^2)}, & \text{if } n = pk, \;\; k = 1,3,5,\ldots \\ \dfrac{M_1 r \ln r}{2\mu_r}, & \text{if } n = pk = 1 \end{cases} \tag{1.32}$$

$$M_n(r) = \begin{cases} \dfrac{4B_m}{\pi\mu_0 k}\sin\left(\dfrac{n\pi}{2p}\right), & \text{if } n = pk, \;\; k = 1,3,5,\ldots \\ 0, & \text{otherwise} \end{cases} \tag{1.33}$$

Therefore, the general solution in Region I is:

$$\begin{aligned} \varphi^I(r,\theta) = \sum_{n=1}^{\infty} & [(A_n r^n + B_n r^{-n} + W_n(r)\cos(n\theta_0))\cos(n\theta) \\ & + (C_n r^n + D_n r^{-n} + W_n(r)\sin(n\theta_0))\sin(n\theta)] + A_0 \ln r + B_0 \end{aligned} \tag{1.34}$$

The magnetic potential in the N slots can be expressed as:

$$\varphi^S(r,\theta) = \begin{cases} \varphi_1^F & 0 \le \theta \le \alpha_1 \\ \varphi_j^S & a_j \le \theta \le \beta_{j+1} \\ \varphi_j^F & \beta_j \le \theta \le \alpha_j \\ \varphi_1^F & \beta_{N+1} \le \theta \le 2\pi \end{cases} \tag{1.35}$$

In order to calculate the unknown coefficients of Eq. (1.12), (1.13), (1.22), (1.34) and (1.35), the magnetic potential at the modulator ring must be described in an analytical and continuous form, so the Fourier Series method is implemented as shown in Appendix A1.3.

The Fourier Series expansion of $\varphi^S$ is:

$$\varphi^S(r,\theta) = a_0 + \sum_{k=1}^{\infty}(a_k \cos(kx) + b_k \sin(kx)) \tag{1.36}$$

where:

$$a_0 = \frac{1}{\pi}\left[\sum_{j=1}^{N}\sum_{n=1}^{\infty}\frac{\gamma(1-\cos(n\pi))\left(X_{jn} r^{\frac{n\pi}{\gamma}} + \Upsilon_{jn} r^{\frac{-n\pi}{\gamma}}\right)}{n\pi} + \sum_{j=1}^{N}(\gamma+\delta)\varphi_j^F\right] \tag{1.37}$$

$$a_k = \sum_{j=1}^{N}\sum_{n=1}^{\infty}\frac{\tau_{knj}}{\pi}\left(X_{jn}r^{\frac{n\pi}{\gamma}} + \Upsilon_{jn}r^{\frac{-n\pi}{\gamma}}\right) - \sum_{j=1}^{N}\frac{2\left(\varphi_j^F + \varphi_{j+1}^F\right)}{\pi\gamma k^2}\sin\left(\frac{k\gamma}{2}\right)\sin\left(k\frac{\beta_{j+1}+\alpha_j}{2}\right) \quad (1.38)$$

$$b_k = \sum_{j=1}^{N}\sum_{n=1}^{\infty}\frac{\omega_{knj}}{\pi}\left(X_{jn}r^{\frac{n\pi}{\gamma}} + \Upsilon_{jn}r^{\frac{-n\pi}{\gamma}}\right) + \sum_{j=1}^{N}\frac{2\left(\varphi_j^F + \varphi_{j+1}^F\right)}{\pi\gamma k^2}\sin\left(\frac{k\gamma}{2}\right)\cos\left(k\frac{\beta_{j+1}+\alpha_j}{2}\right) \quad (1.39)$$

where:

$$\tau_{nkj} = \begin{cases} \dfrac{\frac{n\pi}{\gamma}\left[\cos(n\pi)\cos\left(k\beta_{j+1}\right) - \cos\left(k\alpha_j\right)\right]}{k^2 - \frac{n^2\pi^2}{\gamma^2}} & k \neq \dfrac{n\pi}{\gamma} \\ -\dfrac{\gamma}{2}\sin\left(k\alpha_j\right) & k = \dfrac{n\pi}{\gamma} \end{cases} \quad (1.39)$$

$$\omega_{nkj} = \begin{cases} \dfrac{\frac{n\pi}{\gamma}\left[\cos(n\pi)\sin\left(k\beta_{j+1}\right) - \sin\left(k\alpha_j\right)\right]}{k^2 - \frac{n^2\pi^2}{\gamma^2}} & k \neq \dfrac{n\pi}{\gamma} \\ \dfrac{\gamma}{2}\cos\left(k\alpha_j\right) & k = \dfrac{n\pi}{\gamma} \end{cases} \quad (1.39)$$

## *1.2 Boundary Conditions*

For the coefficients determination of Eq. (1.12), (1.13), (1.22), (1.34) and (1.36), the boundary conditions are applied in each case [1.1].

1. At the radius of the inner yoke $(r = r_1)$:

$$\varphi^I(r_1, \theta) = 0 \quad (1.40)$$

Therefore:

$$A_n r_1^n + B_n r_1^{-n} + W_n(r_1)\cos(n\theta_0) = 0 \quad (1.41)$$

$$C_n r_1^n + D_n r_1^{-n} + W_n(r_1)\sin(n\theta_0) = 0 \quad (1.42)$$

$$A_0 \ln r_1 + B_0 = 0 \quad (1.43)$$

2. On the surface of the inner rotor PMs ($r = r_2$), from the continuity of the magnetic potential and its derivative the following equations are derived:

$$\varphi^{I}(r_2, \theta) = \varphi^{II}(r_2, \theta) \quad (1.43)$$

$$\mu_r \left.\frac{\partial \varphi^{II}}{\partial r}\right|_{r=r_2} = \mu_r \left.\frac{\partial \varphi^{I}}{\partial r}\right|_{r=r_1} - M_r \quad (1.44)$$

Therefore:

$$A_n r_2^n + B_n r_2^{-n} + W_n(r_2)\cos(n\theta_0) = E_n r_2^n + F_n r_2^{-n} \quad (1.45)$$

$$C_n r_2^n + D_n r_2^{-n} + W_n(r_2)\sin(n\theta_0) = G_n r_2^n + H_n r_2^{-n} \quad (1.46)$$

$$A_0 \ln r_2 + B_0 = E_0 \ln r_2 + F_0 \quad (1.47)$$

$$nE_n r_2^n - nF_n r_2^{-n} = nA_n r_2^n - nB_n r_2^{-n} + r_2 W_n(r_2)\cos(n\theta_0) - \frac{r_2}{\mu_r} M_n \cos(n\theta_0) \quad (1.48)$$

$$nG_n r_2^n - nH_n r_2^{-n} = nC_n r_2^n - nD_n r_2^{-n} + r_2 W_n(r_2)\sin(n\theta_0) - \frac{r_2}{\mu_r} M_n \sin(n\theta_0) \quad (1.49)$$

$$A_0 = E_0 \quad (1.50)$$

3. At the radius of the outer iron yoke ($r = r_6$):

$$\varphi^{III}(r_6, \theta) = 0 \quad (1.51)$$

Therefore:

$$I_n r_5^n + J_n r_5^{-n} = 0 \quad (1.52)$$

$$K_n r_5^n + L_n r_5^{-n} = 0 \quad (1.53)$$

$$I_0 \ln r_5 + I_0 = 0 \quad (1.53)$$

Furthermore, the magnetic potential has already been described as a continuous Fourier Series in the slots.

The coefficients of Fourier Series are $c_0, c_n, d_n$ and $e_0, e_n, f_n$ for the cases of $r = r_3$ and $r = r_4$ respectively. Consequently, the following relations can be obtained:

4. From the continuity of the magnetic potential at the radius $r = r_3$:

$$\varphi^{II}(r_3, \theta) = \varphi_j^S(r_3, \theta) \tag{1.54}$$

Therefore:

$$E_0 \ln r_3 + F_0 = \frac{c_0}{2} \tag{1.55}$$

$$E_n r_3^n + F_n r_3^{-n} = c_n \tag{1.56}$$

$$G_n r_3^n + H_n r_3^{-n} = d_n \tag{1.57}$$

5. From the continuity of the magnetic potential at the radius $r = r_4$:

$$\varphi^{III}(r_4, \theta) = \varphi_j^S(r_4, \theta) \tag{1.58}$$

Therefore:

$$I_0 \ln r_4 + J_0 = \frac{e_0}{2} \tag{1.59}$$

$$I_n r_4^n + J_n r_4^{-n} = e_n \tag{1.60}$$

$$K_n r_4^n + L_n r_4^{-n} = f_n \tag{1.61}$$

6. From the continuity of the induction at the radius $r = r_3$:

$$\left.\frac{\partial \varphi^{II}}{\partial r}\right|_{r=r_3} = \left.\frac{\partial \varphi_j^S}{\partial r}\right|_{r=r_3} \tag{1.62}$$

Therefore, the following equation must be satisfied for every slot:

$$\int_{\alpha_j}^{\beta_{j+1}} \left.\frac{\partial \varphi_j^S}{\partial r}\right|_{r=r_3} \sin\left(\frac{n\pi}{\gamma}(\theta - \alpha_j)\right) d\theta = \int_{\alpha_j}^{\beta_{j+1}} \left.\frac{\partial \varphi^{II}}{\partial r}\right|_{r=r_3} \sin\left(\frac{n\pi}{\gamma}(\theta - \alpha_j)\right) d\theta \tag{1.63}$$

which yields:

$$\frac{m\pi}{2}\left(X_{jm}r_3^{\frac{m\pi}{\gamma}} - Y_{jm}r_3^{-\frac{m\pi}{\gamma}}\right) = \sum_{n=1}^{\infty} n[(E_n r_3^n - F_n r_3^{-n})\tau_{nmj} + (G_n r_3^n - H_n r_3^{-n})\omega_{nmj}] + \frac{\gamma(1-\cos(m\pi))E_0}{m\pi} \quad (1.64)$$

where $m = 1, \dots, n$

Following a similar procedure, the following equation can be obtained for $r = r_4$:

$$\frac{m\pi}{2}\left(X_{jm}r_4^{\frac{m\pi}{\gamma}} - Y_{jm}r_4^{-\frac{m\pi}{\gamma}}\right) = \sum_{n=1}^{\infty} n[(I_n r_4^n - J_n r_4^{-n})\tau_{nmj} + (K_n r_4^n - L_n r_4^{-n})\omega_{nmj}] + \frac{\gamma(1-\cos(m\pi))I_0}{m\pi} \quad (1.65)$$

In addition, the continuity of the magnetic flux across the ferromagnetic segments should also be satisfied, so the flow through the inside and outside surface should be equal:

$$\oint \left.\frac{\partial \varphi^{II}}{\partial r}\right|_{r=r_3} r d\theta = \oint \left.\frac{\partial \varphi^{III}}{\partial r}\right|_{r=r_4} r d\theta \quad (1.66)$$

Evaluating both sides of Eq.(1.66), the following relation is derived:

$$E_0 = I_0 \quad (1.67)$$

Finally, the flux flowing into the ferromagnetic segment should be equal to the flux flowing out, thus:

$$\int_{\beta_j}^{\alpha_j} \left.\frac{\partial \varphi^{II}}{\partial r}\right|_{r=r_3} r d\theta + \int_{r_3}^{r_4} \left.\frac{\partial \varphi_{j-1}^{S}}{r\,\partial\theta}\right|_{\theta=\beta_j} dr = \int_{\beta_j}^{\alpha_j} \left.\frac{\partial \varphi^{III}}{\partial r}\right|_{r=r_4} r d\theta + \int_{r_3}^{r_4} \left.\frac{\partial \varphi_{j}^{S}}{r\,\partial\theta}\right|_{\theta=\alpha_j} dr \quad (1.68)$$

After simplifications Eq.(1.69) is derived.

$$\sum_{n=1}^{\infty} 2\sin\left(n\frac{\delta}{2}\right)\Bigg[(E_n r_3^n - F_n r_3^{-n} - I_n r_4^n + J_n r_4^{-n})\cos\left(n\frac{\alpha_j+\beta_j}{2}\right) + (G_n r_3^n$$
$$- H_n r_3^{-n} - K_n r_4^n + L_n r_4^{-n})\sin\left(n\frac{\alpha_j+\beta_j}{2}\right)\Bigg]$$
$$= \sum_{n=1}^{\infty}\Bigg[(X_{jn} - X_{(j-1)n}\cos(n\pi))\left(r_4^{\frac{n\pi}{\gamma}} - r_3^{\frac{n\pi}{\gamma}}\right) - (Y_{jn} \quad (1.69)$$
$$- Y_{(j-1)n}\cos(n\pi))\left(r_4^{-\frac{n\pi}{\gamma}} - r_3^{-\frac{n\pi}{\gamma}}\right)\Bigg]$$
$$+ \left(\frac{\varphi_{j+1}^F - 2\varphi_j^F + \varphi_{j-1}^F}{\gamma}\right)\ln\frac{r_4}{r_3}$$

Therefore, from the boundary conditions, a linear system of $(2Nn + N + 12n + 6)$ equations is derived, where $n$ is the number of solutions of the general solutions of the PDE of the system, from which the unknown coefficients: $A_n, B_n, C_n, D_n, E_n, F_n, G_n, H_n, I_n, J_n, K_n, L_n, A_0, B_0, E_0, F_0, I_0, J_0, X_{jn}, Y_{jn}, \varphi_j^F$ can be calculated.

Therefore, the radial and tangential components of magnetic induction can be obtained:

$$B_r = -\mu_0\frac{\partial\varphi}{\partial r} \quad (1.70)$$

$$B_\theta = -\frac{\mu_0}{r}\frac{\partial\varphi}{\partial\theta} \quad (1.71)$$

Following the same methodology, the respective coefficients of the second model -without the inner rotor's PMs- can be calculated.

## *1.3 Torque Calculation*

In order to evaluate the tangential force and therefore the resulting torque at the two rotors of the CMG, the Maxwell Stress Tensor will be constructed. The Maxwell Stress Tensor is derived through the Lorentz force [1.2], [1.3]:

$$\mathbf{F} = q(\mathbf{E} + \mathbf{v}\times\mathbf{B}) \quad (1.72)$$

where $\mathbf{F}$ is the force, $q$ is the charge, $\mathbf{v}$ is the velocity of the charge, $\mathbf{E}$ is the applied electric intensity field and $\mathbf{B}$ is the applied magnetic induction. The Lorentz force in differential form is:

$$\mathbf{f} = \rho(\mathbf{E} + \mathbf{v}\times\mathbf{B}) \quad (1.73)$$

where $\mathbf{f}$ is the force density and $\rho$ is the charge density per unit volume.

Furthermore, since $\mathbf{J} = \rho\mathbf{v}$:

$$\mathbf{f} = \rho\mathbf{E} + \mathbf{J} \times \mathbf{B} \tag{1.74}$$

From Maxwell laws the following relation is obtained as shown in Appendix A1.4:

$$\mathbf{f} = \mathrm{E}_0\left[(\nabla \cdot \mathbf{E})\mathbf{E} + (\mathbf{E} \cdot \nabla)\mathbf{E} - \frac{1}{2}\nabla\mathbf{E}^2\right] + \frac{1}{\mu_0}\left[(\nabla \cdot \mathbf{B})\mathbf{B} + (\mathbf{B} \cdot \nabla)\mathbf{B} - \frac{1}{2}\nabla\mathbf{B}^2\right] - \mathrm{E}_0\frac{\partial}{\partial \mathrm{t}}(\mathbf{E} \times \mathbf{B}) \tag{1.75}$$

Hence, the Maxwell Stress Tensor can be introduced as:

$$\nabla \cdot \overleftrightarrow{\mathbf{T}} = \mathbf{f} + \mathrm{E}_0\mu_0\frac{\partial \mathbf{S}}{\partial \mathrm{t}} \tag{1.76}$$

Where $\overleftrightarrow{\mathbf{T}}$ is the Maxwell Stress Tensor and $\mathbf{S}$ is the Poynting vector:

$$\mathbf{S} = \frac{1}{\mu_0}\mathbf{E} \times \mathbf{B} \tag{1.77}$$

$\overleftrightarrow{\mathbf{T}}$ can be written as:

$$\mathrm{T}_{\mathrm{ij}} = \mathrm{E}_0\mathrm{E}_\mathrm{i}\mathrm{E}_\mathrm{j} + \frac{1}{\mu_0}\mathrm{B}_\mathrm{i}\mathrm{B}_\mathrm{j} - \frac{1}{2}\left(\mathrm{E}_0\mathrm{E}^2 + \frac{1}{\mu_0}\mathrm{B}^2\right)\delta_{\mathrm{ij}} \tag{1.78}$$

Where $\delta_{ij}$ is the Kronecker delta:

$$\delta_{\mathrm{ij}} = \begin{cases} 1\ , & \mathrm{i} = \mathrm{j} \\ 0\ , & \mathrm{i} \neq \mathrm{j} \end{cases} \tag{1.79}$$

And $\mathrm{i}, \mathrm{j}$ are the $\mathrm{r}, \theta, \mathrm{z}$ coordinates.

Furthermore:

$$\left(\mathbf{a_i} \cdot \overleftrightarrow{\mathbf{T}_{\mathbf{ij}}}\right)_\mathbf{j} = \sum_{\mathrm{i=r,\theta,z}} \mathrm{a}_\mathrm{i}\mathrm{T}_{\mathrm{ij}} \tag{1.80}$$

Following the simplifications shown in Appendix A1.5 the Maxwell Stress Tensor is obtained from:

$$\overleftrightarrow{\mathbf{T}} = \frac{1}{\mu_0}\begin{bmatrix} \dfrac{\mathrm{B}_\mathrm{r}^2 - \mathrm{B}_\theta^2}{2} & \mathrm{B}_\mathrm{r}\mathrm{B}_\theta \\ \mathrm{B}_\theta\mathrm{B}_\mathrm{r} & \dfrac{\mathrm{B}_\theta^2 - \mathrm{B}_\mathrm{r}^2}{2} \end{bmatrix} \tag{1.81}$$

Therefore, the force can be calculated from:

$$\mathbf{F} = \mathrm{L}\int_{0}^{2\pi} \overleftrightarrow{\mathbf{T}}\, \mathrm{d}\mathbf{a}\, \mathrm{ds} \tag{1.82}$$

where $\mathrm{L}$ is the effective length of the coaxial magnetic gear in the z-direction. At a radius $\mathrm{r}$ it can be written as:

$$\mathbf{F}(\mathrm{r}) = \mathrm{L}\int_{0}^{2\pi} \frac{1}{\mu_0}\begin{bmatrix} \frac{\mathrm{B_r^2} - \mathrm{B_\theta^2}}{2} & \mathrm{B_r B_\theta} \\ \mathrm{B_\theta B_r} & \frac{\mathrm{B_\theta^2} - \mathrm{B_r^2}}{2} \end{bmatrix}\begin{bmatrix} 1 \\ 0 \end{bmatrix} \mathrm{r}\, \mathrm{d}\theta \tag{1.83}$$

that yields:

$$\mathbf{F}(\mathrm{r}) = \frac{\mathrm{Lr}}{\mu_0}\int_{0}^{2\pi} \begin{bmatrix} \frac{\mathrm{B_r^2} - \mathrm{B_\theta^2}}{2} \\ \mathrm{B_\theta B_r} \end{bmatrix} \mathrm{d}\theta \tag{1.84}$$

Therefore, the tangential force at the radius $\mathrm{r}$ is:

$$\mathrm{F_\theta}(\mathrm{r}) = \frac{\mathrm{Lr}}{\mu_0}\int_{0}^{2\pi} \mathrm{B_\theta B_r}\, \mathrm{d}\theta \tag{1.85}$$

As a result, the torque is:

$$\mathrm{M}(\mathrm{r}) = \frac{\mathrm{Lr^2}}{\mu_0}\int_{0}^{2\pi} \mathrm{B_\theta B_r}\, \mathrm{d}\theta \tag{1.86}$$

The torque at the inner rotor can be obtained, after the superposition of the magnetic induction of inner and outer rotor, as follows [1.4]:

$$\mathrm{M_{in}}(\mathrm{r_2}) = \frac{\mathrm{Lr_2^2}}{\mu_0}\int_{0}^{2\pi} \big(\mathrm{B_{\theta,in}}(\mathrm{r_2}) + \mathrm{B_{\theta,out}}(\mathrm{r_2})\big)\big(\mathrm{B_{r,in}}(\mathrm{r_2}) + \mathrm{B_{r,out}}(\mathrm{r_2})\big)\mathrm{d}\theta \tag{1.87}$$

The integrals $\int_0^{2\pi} \mathrm{B_{\theta,in}}(\mathrm{r_2})\mathrm{B_{r,in}}(\mathrm{r_2})\mathrm{d}\theta$ and $\int_0^{2\pi} \mathrm{B_{\theta,out}}(\mathrm{r_2})\mathrm{B_{r,out}}(\mathrm{r_2})\mathrm{d}\theta$ are zero.

The integral of Eq.(1.87) can be solved analytically as shown in Appendix A1.6 which yields that:

$$\mathrm{M_{in}}(\mathrm{r_2}) = \pi\mu_0 \mathrm{Lr_2^2}\sum_{\mathrm{n=1}}^{\infty}[\,(\mathrm{P_{n,out}S_{n,in}} + \mathrm{Q_{n,out}R_{n,in}}) + (\mathrm{P_{n,in}S_{n,out}} + \mathrm{Q_{n,in}R_{n,out}})] \tag{1.88.A}$$

where:

$$P_{n,in} = n(E_{n,in}r_2^{n-1} - F_{n,in}r_2^{-n-1}) \quad (1.88.B)$$

$$Q_{n,in} = n(G_{n,in}r_2^{n-1} - H_{n,in}r_2^{-n-1}) \quad (1.88.C)$$

$$R_{n,in} = -n(E_{n,in}r_2^{n-1} + F_{n,in}r_2^{-n-1}) \quad (1.88.D)$$

$$S_{n,in} = n(G_{n,in}r_2^{n-1} + H_{n,in}r_2^{-n-1}) \quad (1.88.E)$$

$$P_{n,out} = n(E_{n,out}r_2^{n-1} - F_{n,out}r_2^{-n-1}) \quad (1.88.F)$$

$$Q_{n,out} = n(G_{n,out}r_2^{n-1} - H_{n,out}r_2^{-n-1}) \quad (1.88.G)$$

$$R_{n,out} = -n(E_{n,out}r_2^{n-1} + F_{n,out}r_2^{-n-1}) \quad (1.88.H)$$

$$S_{n,out} = n(G_{n,out}r_2^{n-1} + H_{n,out}r_2^{-n-1}) \quad (1.88.I)$$

## *1.4 Torque as a function of rotation*

The contributing terms to the calculation of $M_{in}$ are the harmonics of the inner rotor's pole pairs [1.5] which can be written in the form of $m = (2k-1)p_{in}$ where $k$ a positive integer. If the contributing terms have been calculated for a given angle of the inner rotor, an analytical equation correlating $M_{in}$ at every position of the inner rotor can be derived, using these terms [1.4].

If the inner rotor's angle of rotation is $\theta_{in}$ and the outer rotor is at a given position $\theta_{out}$ implementing a similar process as this described for the Eq. (1.87), $M_{in}$ is obtained as follows:

$$\int_0^{2\pi} B_{\theta,in}(r_2)B_{r,out}(r_2)d\theta = \sum_m \pi\left[U_{1,m}\sin(m\theta_{in}) + V_{1,m}\cos(m\theta_{in})\right] \quad (1.89.A)$$

where:

$$U_{1,m} = S_{m,in}Q_{m,out} - R_{m,in}P_{m,out} \quad (1.89.B)$$

$$V_{1,m} = P_{m,out}S_{m,in} + R_{m,in}Q_{m,out} \quad (1.89.C)$$

In addition,

$$\int_0^{2\pi} B_{r,in}(r_2)B_{\theta,out}(r_2)d\theta = \sum_m \pi\left[U_{2,m}\sin(m\theta_{in}) + V_{2,m}\cos(m\theta_{in})\right] \quad (1.90.A)$$

where:

$$U_{2,m} = P_{m,in}R_{m,out} - Q_{m,in}S_{m,out} \quad (1.90.B)$$

$$V_{2,m} = P_{m,in}S_{m,out} + Q_{m,in}R_{m,out} \quad (1.90.C)$$

As a consequence, from Eq.(1.89.A) and Eq. (1.90.A) the induced torque at the inner rotor is:

$$M_{in}(r_2) = \pi\mu_0 L r_2^2 \sum_m \left[(U_{1,m} + U_{2,m})\sin(m\theta_{in}) + (V_{1,m} + V_{2,m})\cos(m\theta_{in})\right] \quad (1.91)$$

Eq. (1.91) can be further simplified to:

$$M_{in}(r_2) = \sum_{k=1}^{\infty} \xi_{(2k-1)p_{in},in} \sin[(2k-1)p_{in}\theta_{in} + (2k-1)p_{out}\theta_{out}] \quad (1.92)$$

where $\xi_{(2k-1)p_{in},in}$ is the amplitude of each contributing term that can be determined as follows:

$$\xi_{(2k-1)p_{in},in} = \pi\mu_0 L r_2^2 \sqrt{\left(U_{1,(2k-1)p_{in}} + U_{2,(2k-1)p_{in}}\right)^2 + \left(V_{1,(2k-1)p_{in}} + V_{2,(2k-1)p_{in}}\right)^2} \quad (1.93)$$

It should be noted that $U_{1,m}, V_{1,m}, U_{2,m}$ and $V_{2,m}$ are dependent on the position of the outer rotor and independent of the position of the inner rotor due to its harmonics. However, the amplitude of each contributing term $\xi_{(2k-1)p_{in},in}$ is constant and independent of the angle of rotation of the rotors [1.4].

A similar form for the torque at the outer rotor can be obtained following the same process. Therefore, analytical expressions for the induced torque at the two rotors for every angle of rotation are derived, hence there is no requirement to solve the system of $(2Nn + N + 12n + 6)$ linear equations at every position.

From Eq. (1.92) it can be observed that the induced torque is a sum of infinite sinusoidal terms of decreasing amplitude that generate torque ripples that are also observed in the literature [1.5]. The torque ripples are significant especially in low pole-pairs number configurations of CMGs, due to its low contributing harmonics.

The torque ripples approach zero in high pole-pairs numbers and the induced torque can be simplified to:

$$M_{in} = M_{stall,in}\sin(p_{in}\theta_{in} + p_{out}\theta_{out}) \quad (1.95.A)$$

$$M_{out} = -M_{stall,out}\sin(p_{in}\theta_{in} + p_{out}\theta_{out}) \quad (1.95.B)$$

where $M_{stall}$ is the stall torque.

## *1.5 Validation of the analytical model with FEA*

For the calculation of the coefficients an algorithm was developed in MATLAB. The resulting magnetic induction and the induced torques in the two rotors were calculated. The results obtained from the analytical model was compared with those obtained from a 2D FE model.

Ansys Maxwell was used to perform the validation of the analytical model due to its high degree of parametrization of the geometry inputs and its consistency at every angle of rotation and configuration of the CMG drive. A convergence rate of 0.01% was set, while the automatic generated mesh was refined in every pass by 30%.

A case study was performed for the developed model with the following parameters presented in Table 1.1.

**Table 1.1: Parameters of the CMG**

| | |
|---|---|
| $p_{in}$ | 4 |
| $p_{out}$ | 10 |
| $r_1$ [mm] | 80 |
| $r_2$ [mm] | 100 |
| $r_3$ [mm] | 105 |
| $r_4$ [mm] | 125 |
| $r_5$ [mm] | 130 |
| $r_6$ [mm] | 150 |
| $r_{out}$ [mm] | 170 |
| L [mm] | 100 |
| $\delta$ [deg] | 15 |
| $B_r$ [T] | 1.44 |

The analytical solutions were derived taking into account the first 100 solutions of the PDEs.

In Figs.1.6-1.8 the scalar magnetic potential produced from the inner rotor PMS at some critical radii is presented when $\theta_{in} = 0$ and $\theta_{out} = 0$.

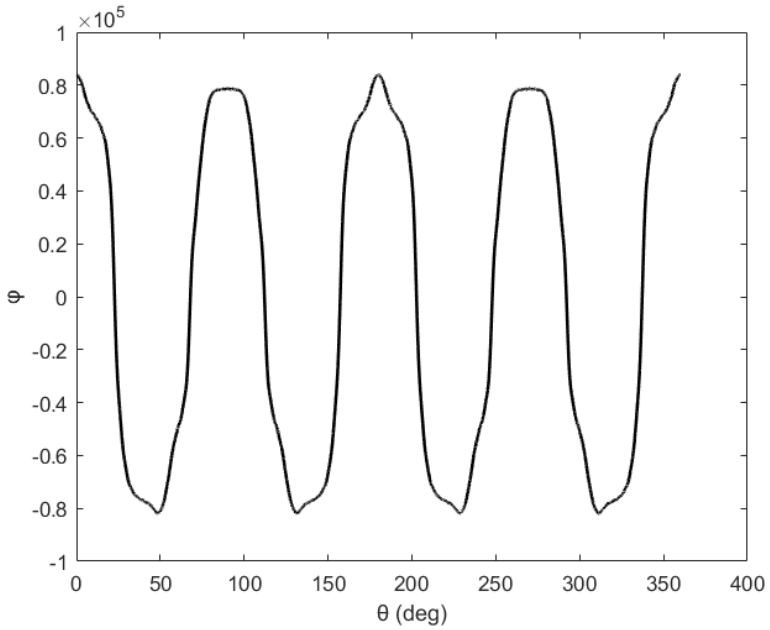


**Figure 1.6: Scalar magnetic potential generated from the inner rotor PMs at $\mathbf{r_2}$ when $\boldsymbol{\theta_{in} = 0}$ and $\boldsymbol{\theta_{out} = 0}$**

From Fig.1.6 it can be observed that the scalar magnetic potential at $r_2$ has four periods (as expected since the inner rotor has four pole-pairs) and alternates between a positive and negative value. The small difference in the value of the scalar magnetic potential at some peaks is attributed to the presence of the modulator ring.

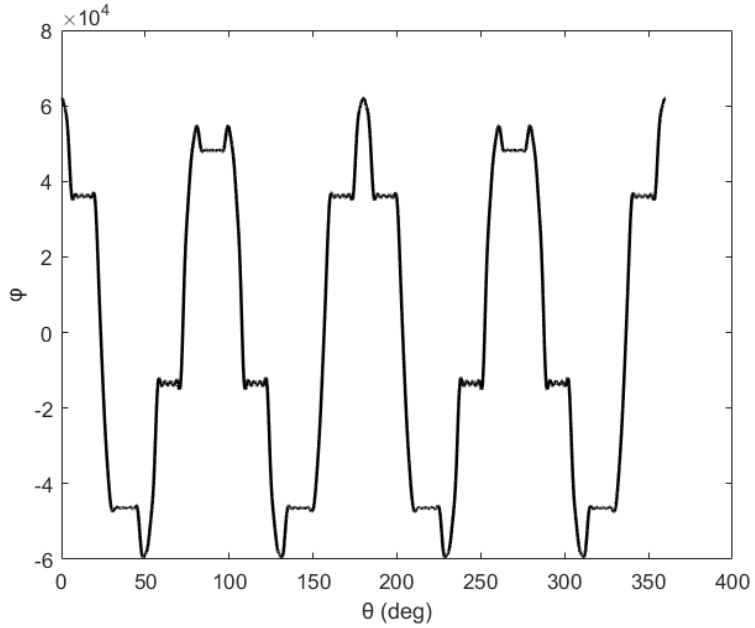


**Figure 1.7: Scalar magnetic potential generated from the inner rotor PMs at $\mathbf{r_3}$ when $\boldsymbol{\theta_{in} = 0}$ and $\boldsymbol{\theta_{out} = 0}$**

From Fig.1.7 it can be observed that the scalar magnetic potential at $r_3$ in the fourteen ferromagnetic segments are clearly shown to be equipotential as expected from Eq.(1.35). Furthermore, it is demonstrated that the first 100 solutions of PDE yield an accurate result.

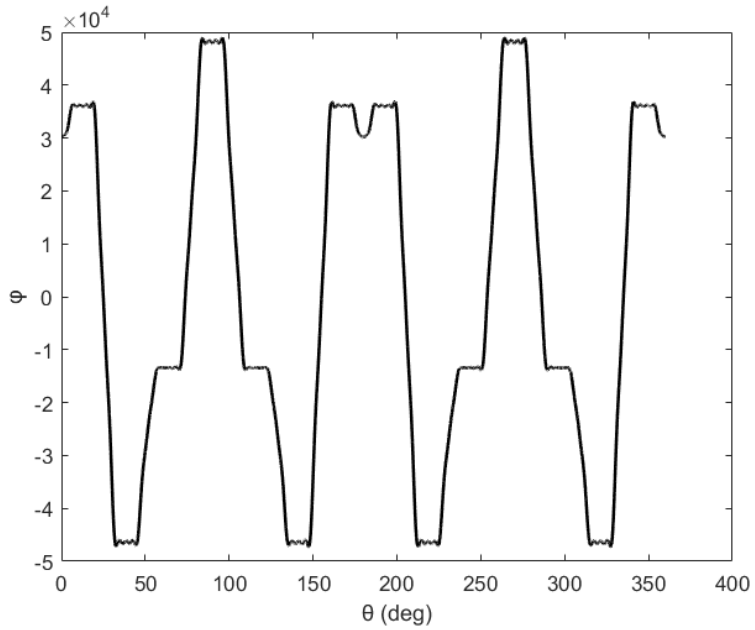


**Figure 1.8: Scalar magnetic potential generated from the inner rotor PMs at $\mathbf{r_4}$ when $\boldsymbol{\theta_{in} = 0}$ and $\boldsymbol{\theta_{out} = 0}$**

From Fig.1.8 it can be observed that the scalar magnetic potential at $\mathrm{r}_4$ in the fourteen ferromagnetic segments are clearly shown to be equipotential as expected from Eq.(1.35). Furthermore, it is demonstrated that the first 100 solutions of PDE yield an accurate result.

In Figs.1.9-1.11 the scalar magnetic potential produced from the outer rotor PMS at some critical radii is presented when $\theta_{\mathrm{in}} = 0$ and $\theta_{\mathrm{out}} = 0$.

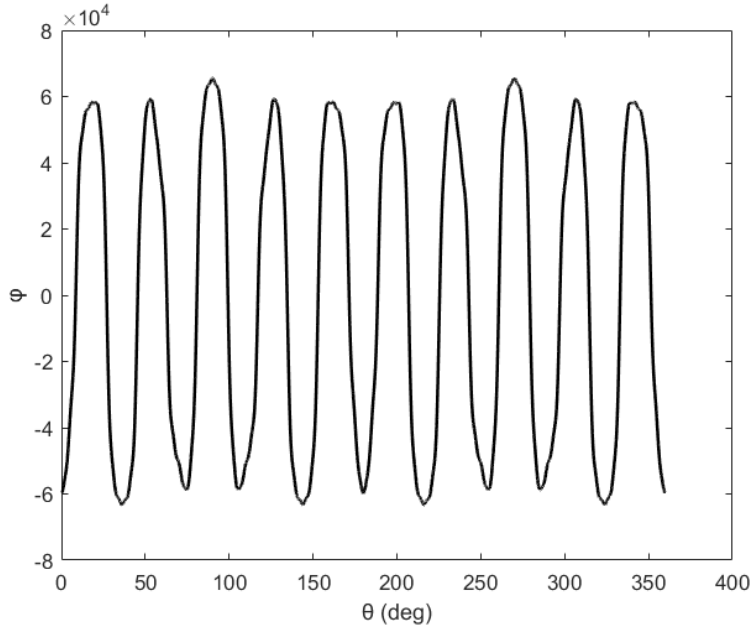


**Figure 1.9: Scalar magnetic potential generated from the outer rotor PMs at $\mathbf{r_5}$ when $\boldsymbol{\theta_{in} = 0}$ and $\boldsymbol{\theta_{out} = 0}$**

From Fig.1.9 it can be observed that the scalar magnetic potential at $\mathrm{r}_5$ has ten periods (as expected since the outer rotor has ten pole-pairs) and alternates between a

positive and negative value. The small difference in the value of the scalar magnetic potential at some peaks is attributed to the presence of the modulator ring.

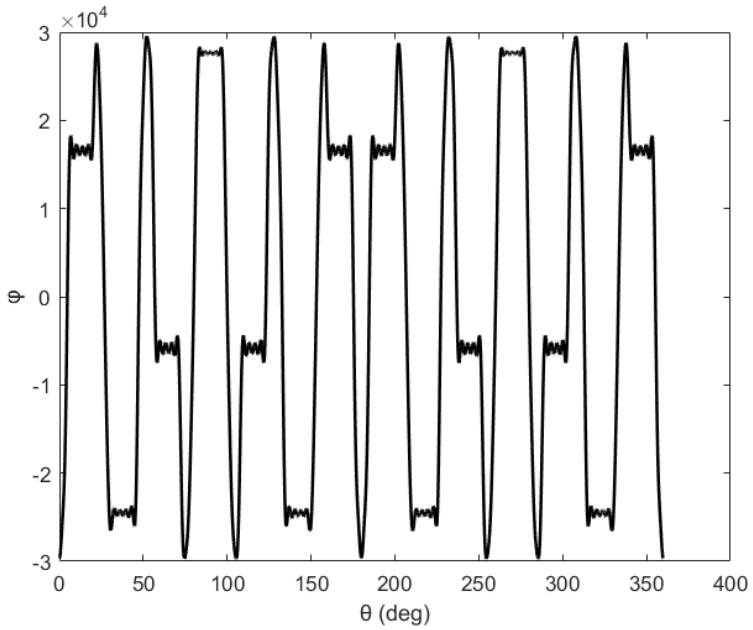


**Figure 1.10: Scalar magnetic potential generated from the outer rotor PMs at $\mathbf{r_4}$ when $\boldsymbol{\theta_{in} = 0}$ and $\boldsymbol{\theta_{out} = 0}$**

From Fig.1.10 it can be observed that the scalar magnetic potential at $r_4$ in the fourteen ferromagnetic segments are clearly shown to be equipotential as expected from Eq.(1.35). Furthermore, it is demonstrated that the first 100 solutions of PDE yield an accurate result.

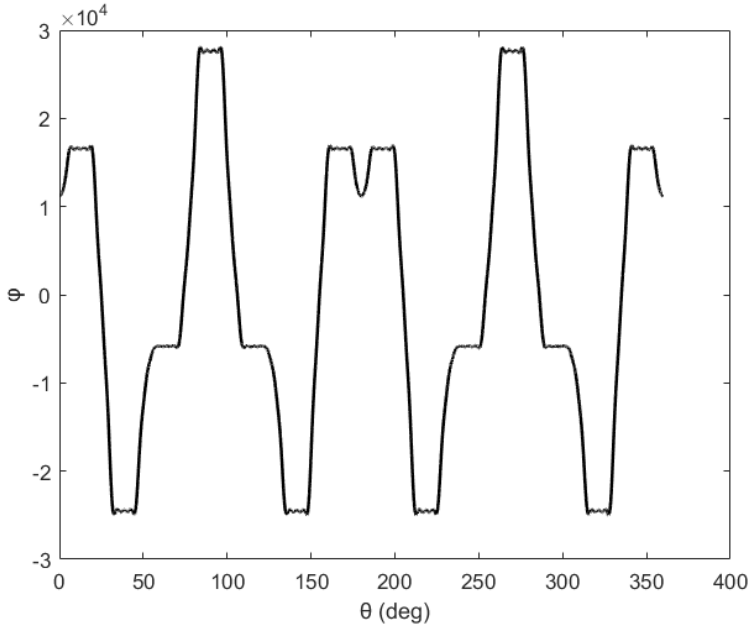


**Figure 1.11: Scalar magnetic potential generated from the outer rotor PMs at $\mathbf{r_3}$ when $\boldsymbol{\theta_{in} = 0}$ and $\boldsymbol{\theta_{out} = 0}$**

From Fig.1.11 it can be observed that the scalar magnetic potential at $\mathrm{r}_3$ in the fourteen ferromagnetic segments are clearly shown to be equipotential as expected from Eq.(1.35). Furthermore, it is demonstrated that the first 100 solutions of PDE yield an accurate result.

In Fig.1.12 the radial and tangential magnetic induction at the radius $\mathrm{r}_3$ is presented.

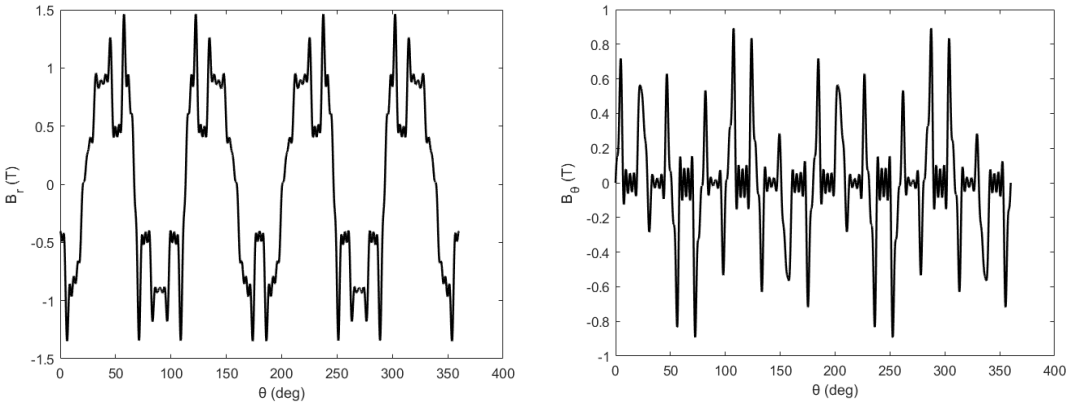


**(a)** **(b)**

**Figure 1.12: Radial (a) and tangential (b) magnetic induction at $\mathbf{r_3}$ when $\boldsymbol{\theta_{in} = 0}$ and $\boldsymbol{\theta_{out} = 0}$**

It is observed that both the radial and tangential magnetic induction at $\mathrm{r}_3$ have a $180°$ symmetry. Furthermore, it can be observed that the tangential magnetic induction in the modulator ring is zero (the fluctuations exist due to the finite solutions considered) which is expected since the ferromagnetic segments are equipotential and Eq.(1.71).

In Fig.1.13 the radial and tangential magnetic induction at the radius $\mathrm{r}_4$ is presented.

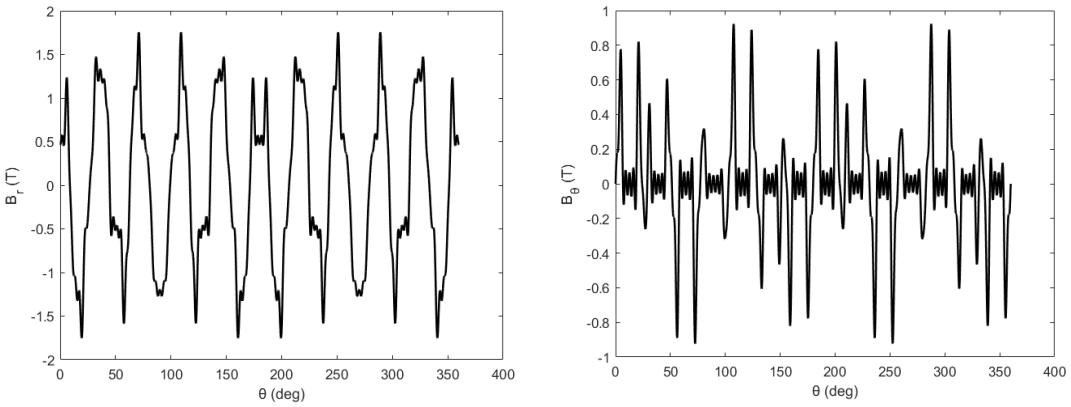


**(a)** **(b)**

**Figure 1.13: Radial (a) and tangential (b) magnetic induction at $\mathbf{r_4}$ when $\boldsymbol{\theta_{in} = 0}$ and $\boldsymbol{\theta_{out} = 0}$**

It is observed that both the radial and tangential magnetic induction at $\mathrm{r}_4$ have a $180°$ symmetry. Furthermore, it can be observed that the tangential magnetic induction in

the modulator ring is zero (the fluctuations exist due to the finite solutions considered) which is expected since the ferromagnetic segments are equipotential and Eq.(1.71).

The induced toques in the inner and outer rotor for the case of $\theta_{\mathrm{in}} = 0$ and $\theta_{\mathrm{out}} = 0$ are zero. Therefore, for $\theta_{\mathrm{in}} = 0$ and $\theta_{\mathrm{out}} = 0$ no torques are induced to the CMG.

In Figs.1.14-1.16 the scalar magnetic potential produced from the inner rotor PMS at some critical radii is presented when $\theta_{\mathrm{in}} = 22.5°$ and $\theta_{\mathrm{out}} = 0$.

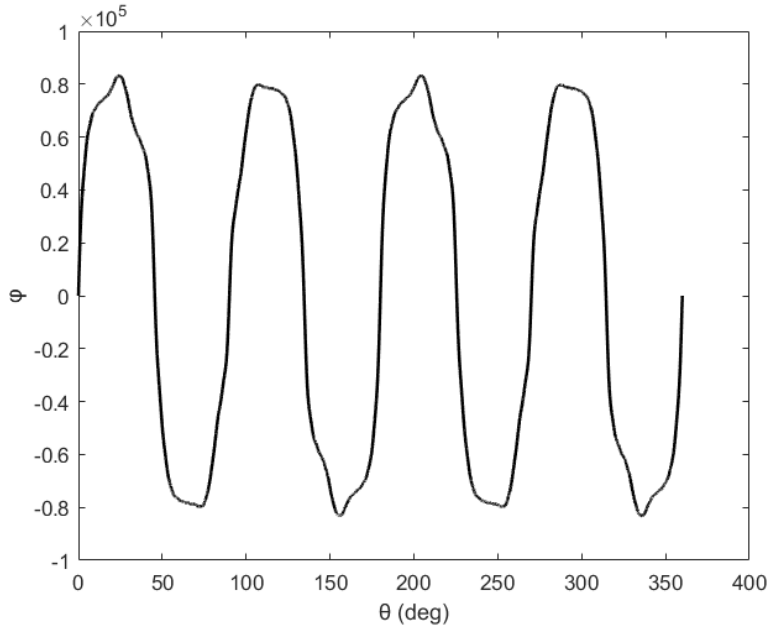


**Figure 1.14: Scalar magnetic potential generated from the inner rotor PMs at $\mathbf{r_2}$ when $\boldsymbol{\theta_{\mathrm{in}} = 22.5°}$ and $\boldsymbol{\theta_{\mathrm{out}} = 0}$**

From Fig.1.14 it can be observed that the scalar magnetic potential at $r_2$ has four periods (as expected since the inner rotor has four pole-pairs) and alternates between a positive and negative value. The small difference in the value of the scalar magnetic potential at some peaks is attributed to the presence of the modulator ring.

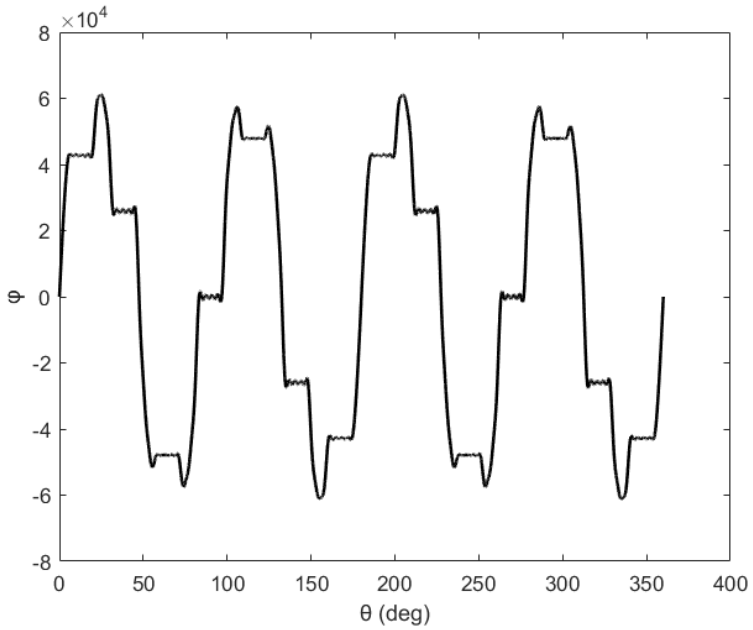


**Figure 1.15: Scalar magnetic potential generated from the inner rotor PMs at $\mathbf{r_3}$ when $\boldsymbol{\theta_{in} = 22.5°}$ and $\boldsymbol{\theta_{out} = 0}$**

From Fig.1.15 it can be observed that the scalar magnetic potential at $r_3$ in the fourteen ferromagnetic segments are clearly shown to be equipotential as expected from Eq.(1.35). Furthermore, it is demonstrated that the first 100 solutions of PDE yield an accurate result.

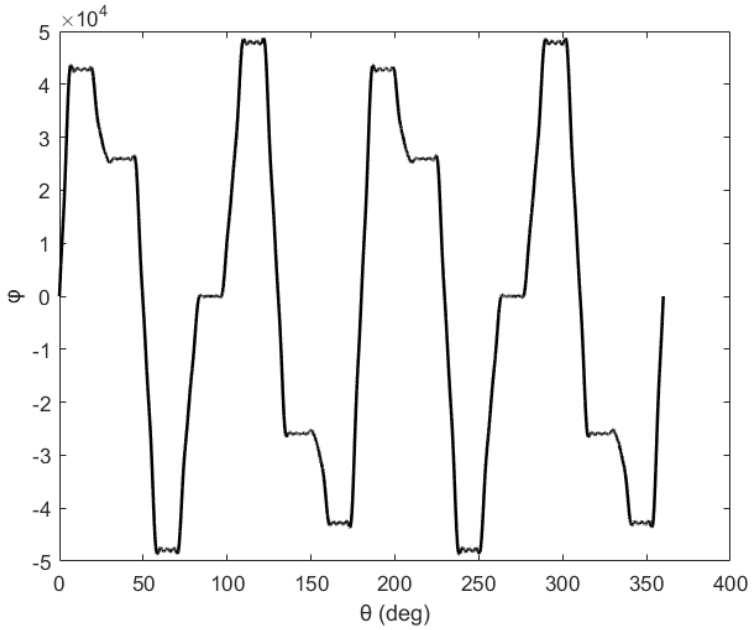


**Figure 1.16: Scalar magnetic potential generated from the inner rotor PMs at $\mathbf{r_4}$ when $\boldsymbol{\theta_{in} = 22.5°}$ and $\boldsymbol{\theta_{out} = 0}$**

From Fig.1.16 it can be observed that the scalar magnetic potential at $r_4$ in the fourteen ferromagnetic segments are clearly shown to be equipotential as expected from Eq.(1.35). Furthermore, it is demonstrated that the first 100 solutions of PDE yield an accurate result.

In Figs.1.17-1.19 the scalar magnetic potential produced from the outer rotor PMS at some critical radii is presented when $\theta_{in} = 22.5°$ and $\theta_{out} = 0$.

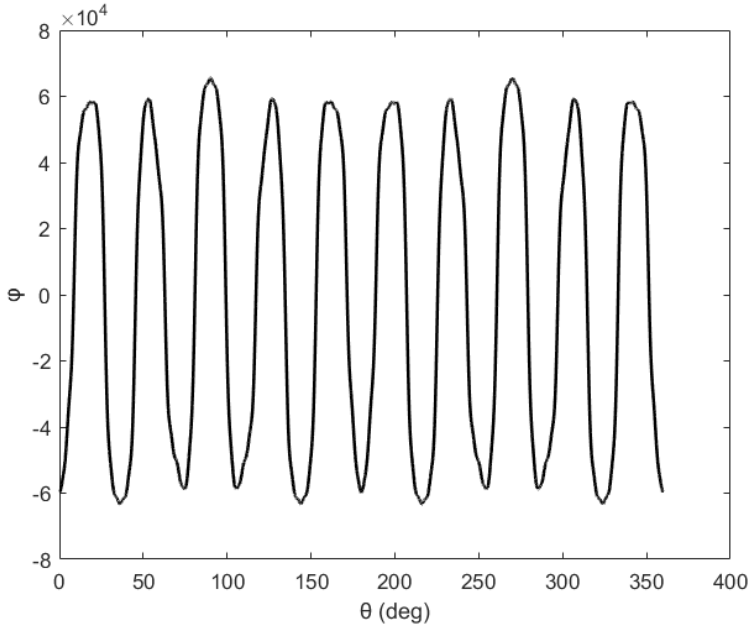


**Figure 1.17: Scalar magnetic potential generated from the outer rotor PMs at $r_5$ when $\theta_{in} = 22.5°$ and $\theta_{out} = 0$**

From Fig.1.17 it can be observed that the scalar magnetic potential at $r_5$ has ten periods (as expected since the outer rotor has ten pole-pairs) and alternates between a positive and negative value. The small difference in the value of the scalar magnetic potential at some peaks is attributed to the presence of the modulator ring.

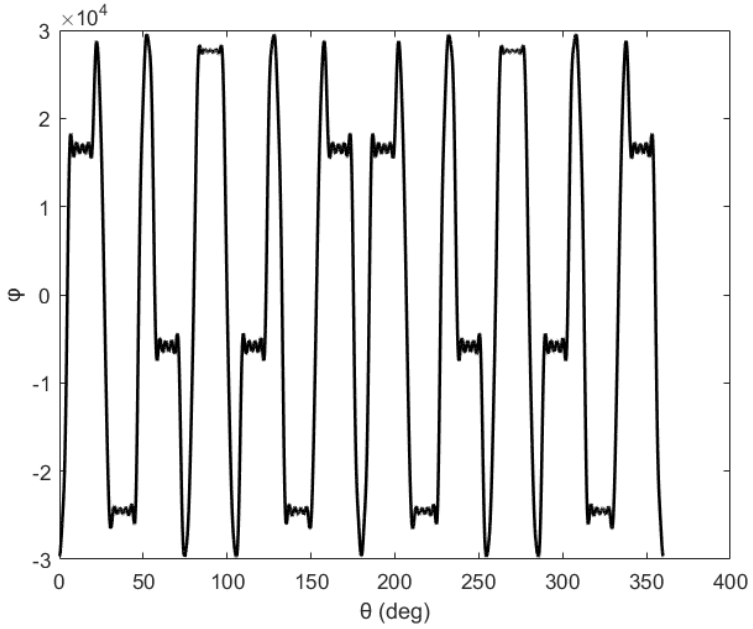


**Figure 1.18: Scalar magnetic potential generated from the outer rotor PMs at $r_4$ when $\theta_{in} = 22.5°$ and $\theta_{out} = 0$**

From Fig.1.18 it can be observed that the scalar magnetic potential at $r_4$ in the fourteen ferromagnetic segments are clearly shown to be equipotential as expected from Eq.(1.35). Furthermore, it is demonstrated that the first 100 solutions of PDE yield an accurate result.

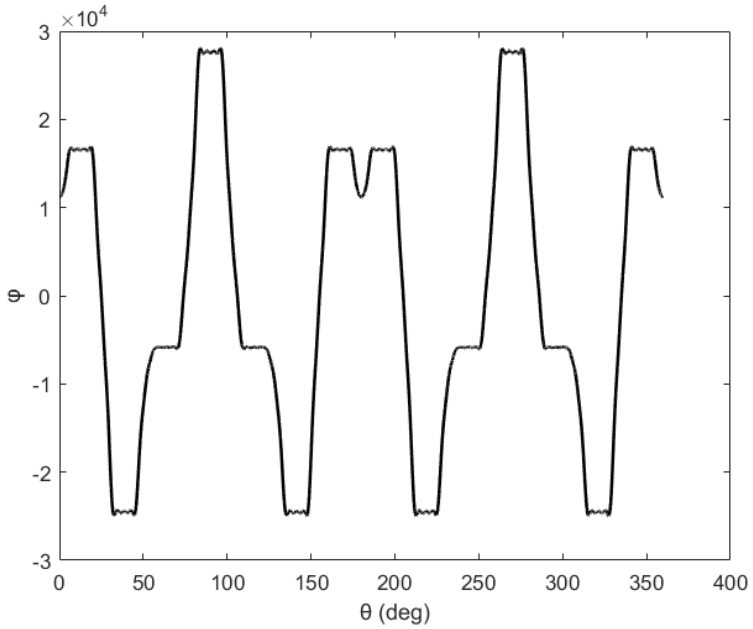


**Figure 1.19: Scalar magnetic potential generated from the outer rotor PMs at $r_3$ when $\theta_{in} = 22.5°$ and $\theta_{out} = 0$**

From Fig.1.19 it can be observed that the scalar magnetic potential at $r_3$ in the fourteen ferromagnetic segments are clearly shown to be equipotential as expected from Eq.(1.35). Furthermore, it is demonstrated that the first 100 solutions of PDE yield an accurate result.

In Fig.1.20 the radial and tangential magnetic induction at the radius $r_3$ is presented.

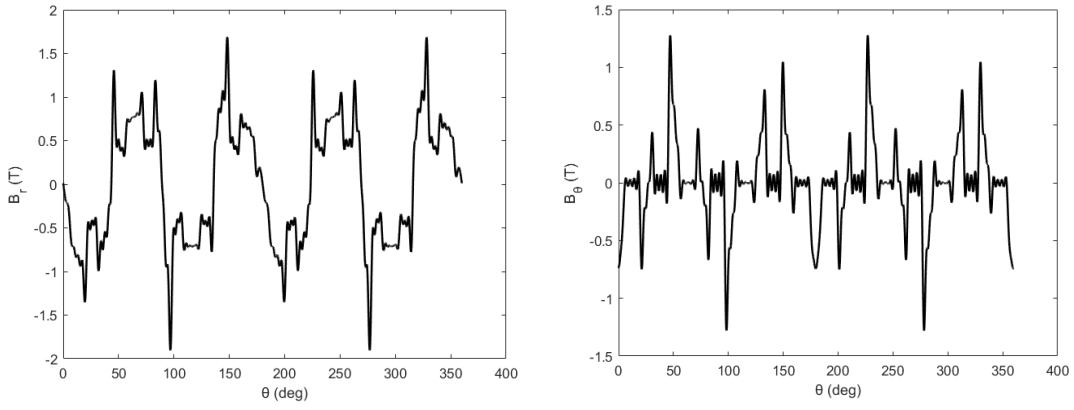


**(a)** **(b)**

**Figure 1.20: Radial (a) and tangential (b) magnetic induction at $r_3$ when $\theta_{in} = 22.5°$ and $\theta_{out} = 0$**

It is observed that both the radial and tangential magnetic induction at $\mathrm{r}_3$ have a $180°$ symmetry. Furthermore, it can be observed that the tangential magnetic induction in the modulator ring is zero (the fluctuations exist due to the finite solutions considered) which is expected since the ferromagnetic segments are equipotential and Eq.(1.71).

In Fig.1.21 the radial and tangential magnetic induction at the radius $\mathrm{r}_4$ is presented.

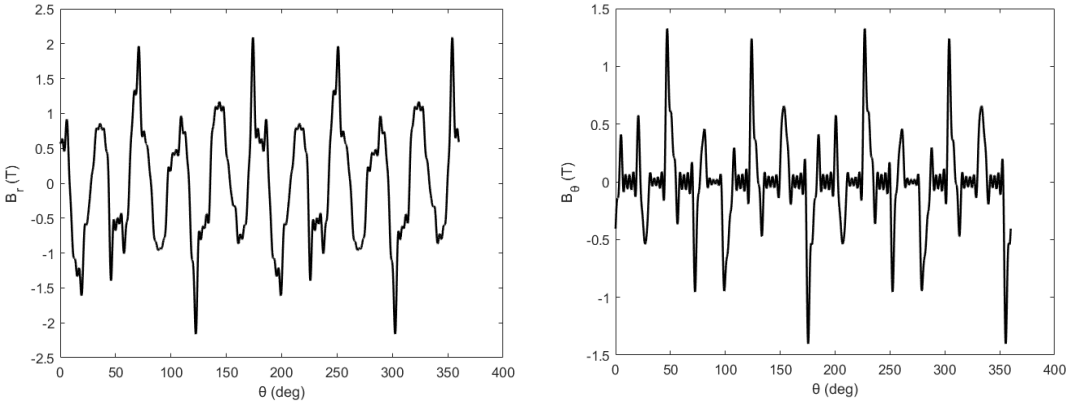


**(a)** **(b)**

**Figure 1.21: Radial (a) and tangential (b) magnetic induction at $\mathbf{r_4}$ when $\boldsymbol{\theta_{in} = 22.5°}$ and $\boldsymbol{\theta_{out} = 0}$**

It is observed that both the radial and tangential magnetic induction at $\mathrm{r}_4$ have a $180°$ symmetry. Furthermore, it can be observed that the tangential magnetic induction in the modulator ring is zero (the fluctuations exist due to the finite solutions considered) which is expected since the ferromagnetic segments are equipotential and Eq.(1.71).

The induced toques in the inner and outer rotor for the case of $\theta_{\mathrm{in}} = 22.5°$ and $\theta_{\mathrm{out}} = 0$ are $333.81\ \mathrm{Nm}$ and $832.98\ \mathrm{Nm}$. Therefore, for $\theta_{\mathrm{in}} = 22.5°$ and $\theta_{\mathrm{out}} = 0$ the maximum induced torque in the rotors can be applied. This is expected from Eq.(1.95.A) and Eq.(1.95.B).

In order to demonstrate the accuracy of the developed model two cases were considered. In the first case, the outer rotor was held stationary and the inner rotor made a full rotation, while in the second case the inner rotor was held stationary and the outer rotor made a full rotation respectively. In Fig.1.22 the results of the described case studies are presented.

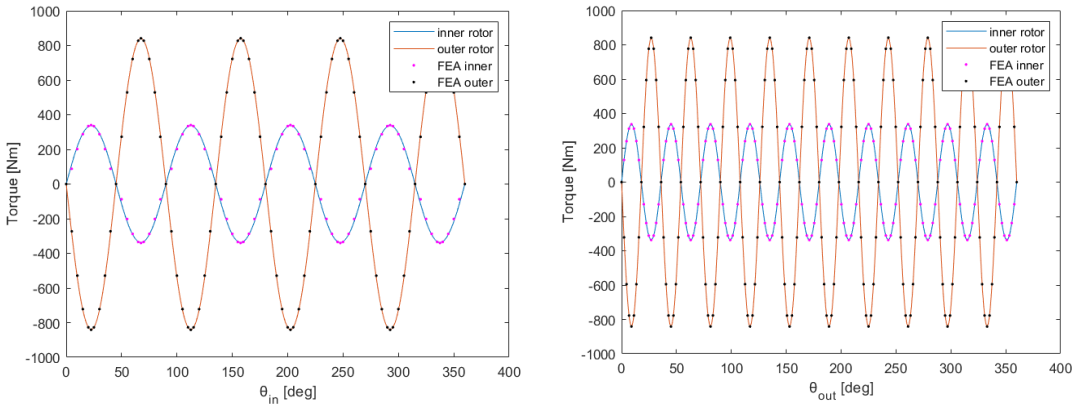


**Figure 1.22: Torque at the rotors with (a) the inner rotor rotating and the outer rotor stationary, (b) the outer rotor rotating and the inner rotor stationary**

The results were confirmed with ANSYS Maxwell, since the values obtained are within 1% of the analytical torque values.

In terms of computational time, there is a significant difference between FEA and the analytical model. FEA requires 23 minutes for the convergence of the torque values. On the other hand, for the analytical model the exact solution is obtained in 11 seconds which is 125 times faster compared to the FE model. Both models ran on a laptop with Intel i5 7th Gen processor, 8 GB of RAM and 2.5 GHz max clocking speed. In Table 1.2 the amplitude of each conributing harmonic is presented for the inner and outer rotor.

**Table 1.2: Amplitude of contributing harmonics**

| Amplitude of inner rotor harmonics (Nm) | | Amplitude of outer rotor harmonics (Nm) | |
|---|---|---|---|
| $\xi_4$ | 333.81 | $\xi_{10}$ | 832.98 |
| $\xi_{12}$ | 1.25 | $\xi_{30}$ | 3.26 |
| $\xi_{20}$ | 0.02 | $\xi_{50}$ | 0.05 |

The stall torque of the inner and outer rotor is calculated from the amplitude of the first contributing harmonic. Therefore the stall torques are:

**Table 1.3**: **Stall torques as calculated from analytical model and FEA**

| Analytical model | FEA |
|---|---|
| $M_{stall,in} = 333.81$ Nm | $M_{stall,in} = 337.15$ Nm |
| $M_{stall,out} = 832.98$ Nm | $M_{stall,out} = 841.31$ Nm |

It can be observed that in both rotors the second contributing harmonic introduces a torque ripple of about $0.37\%$ to the CMG drive. In both rotors the amplitude of the third and higher harmonics is small and could be neglected.

It can be observed that in both rotors the second contributing harmonic introduces a torque ripple of about $0.5\%$ to the CMG drive. In both rotors the amplitude of the third and higher harmonics is small and could be neglected.

Furthermore, the equivalent gear ratio, that can be determined as the quotient of the torque in the outer rotor and the torque in the inner rotor, is $2.4953$ with a deviation of $0.01\%$ for every angle of rotors' rotation, which is within $0.19\%$ of the nominal gear ratio.

## *1.6 Influence of modulator ring in torque density*

For a defined application of the CMG drive, the modulator ring affects significantly the torque density of the CMG drive. To demonstrate this effect, the stall torque was calculated for different configurations of the modulator ring. The parameters described in Table 1.1 remain the same except for the dimensions of the ferromagnetic segments of the modulator ring. These are given as the fill percentages of the air space in the radial and tangential direction respectively:

$$\text{Radial fill percentage} = \frac{r_4 - r_3}{r_5 - r_2} \tag{1.96.A}$$

$$\text{Tangential fill percentage} = \frac{N\delta}{2\pi} \tag{1.96.B}$$

A case study was performed where the above percentages ranged from $40\%$ to $90\%$ and $25\%$ to $75\%$ in the radial and tangential direction respectively. The stall torque calculated in each configuration is presented in the contour map of Fig.1.23.

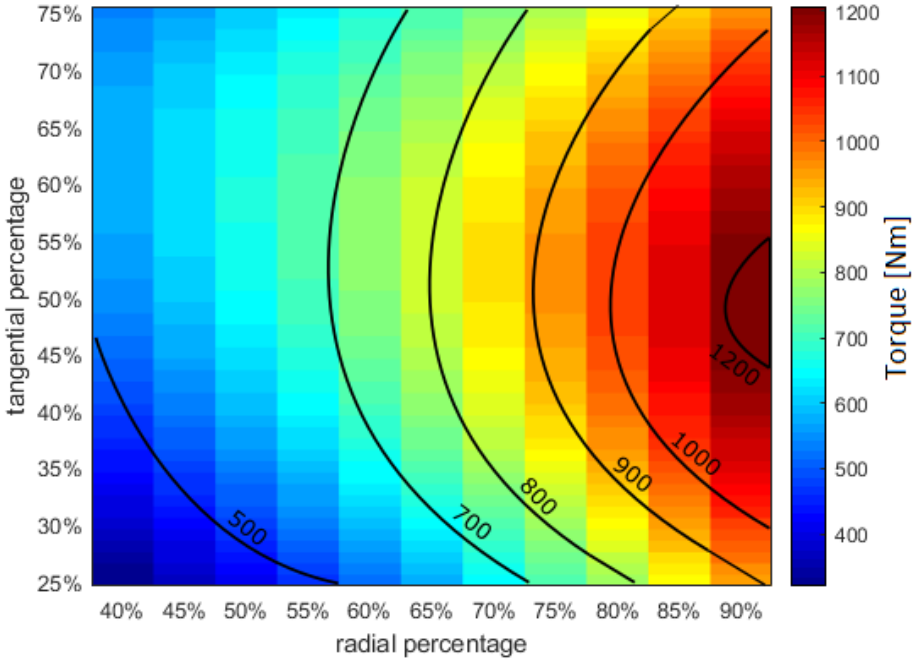


**Figure 1.23: Contour map of stall torque at each configuration of the modulator ring**

The stall torque increases proportionaly with the radial percentage, as expected due to lower magnetic resistance, while in the tangential direction a saturation can be observed above 60%. Therefore, the central angle ($\delta$) of each ferromagnetic segment requires a thorough investigation in every design process of a CMG drive.

## *Chapter 1-Conclusions*

In the present chapter a novel analytical 2D model was developed for the calculation of the torque in the inner and outer rotor in the CMG drive for every angle of their rotation using the Maxwell Stress Tensor. In addition, the torque ripple of CMGs caused by the contributing terms of higher harmonics is calculated analytically with the proposed model. The developed system requires only one calculation of the inner and outer torque at a given angle of their rotation and therefore the computational time of the dynamical response is significantly reduced since it is not essential to calculate the torque at each time step implementing the Gauss elimination algorithm that requires a non-negligible computational cost. A case study was performed where 4 and 10 pole pairs were mounted in the inner and outer rotor respectively. The torque at the inner and outer rotor was calculated for different angle of rotation of the two rotors. The obtained results were compared to a FE simulation that was developed in order to validate the proposed model, which showed a convergence of 1.1%. In addition, a torque ripple of 0.37% was calculated for the CMG drive. However, the analytical model obtained the torque results 125 times faster compared to FEA. In addition, the equivalent gear ratio was within 0.19% of the theoretical gear ratio for every combination of the angle of their respective rotation. The above difference between the two models could be attributed to the assumption of equipotential ferromagnetic segments and linearity of the PMs in that are necessary in order to obtain an analytical solution. However, the above deviation is very small and will not affect the optimization process of a CMG drive and will have a little effect on the accuracy of the dynamical response during transient operation.

## *Appendix A1.1*

The solution of the Laplace PDE in polar coordinates can be calculated as follows:

$$\nabla^2\varphi(r,\theta) = 0 \Rightarrow \varphi_{rr} + \frac{1}{r}\varphi_r + \frac{1}{r^2}\varphi_{\theta\theta} = 0 \qquad (A1.1.1)$$

There are values $\rho_0$ and $\rho$ such as, for $\rho_0 \leq r \leq \rho$:

$$\varphi(\rho_0,\theta) = g(\theta) \quad \text{and} \quad \varphi(\rho,\theta) = f(\theta)$$

So, we implement the separation of variables method:

$$\varphi(r,\theta) = R(r)\Theta(\theta) \qquad (A1.1.2)$$

The above PDE can be written as:

$$R''\Theta + R'\frac{\Theta}{r} + R\frac{\Theta''}{r^2} = 0 \Rightarrow$$
$$r^2R''\Theta + rR'\Theta + R\Theta'' = 0 \Rightarrow$$
$$(r^2R'' + rR')\Theta = -R\Theta'' \Rightarrow$$
$$\frac{r^2R'' + rR'}{R} = -\frac{\Theta''}{\Theta} = \lambda \qquad (A1.1.3)$$

Therefore:

$$\begin{cases} r^2R'' + rR' - \lambda R = 0 \\ \Theta'' + \lambda\Theta = 0 \end{cases} \qquad (A1.1.4)$$

and also: $\Theta(\pi) = \Theta(-\pi), \Theta'(\pi) = \Theta'(-\pi)$

For $\lambda = 0$:

$\Theta_0'' = 0 \Rightarrow \Theta_0' = c_1 \Rightarrow \Theta_0 = c_1\theta + c_2$

From the boundary conditions:

$c_1\pi + c_2 = c_1(-\pi) + c_2 \Rightarrow c_1 = 0$

Therefore:

$\Theta_0(\theta) = c_2$

Therefore $\lambda_0 = 0$ is an eigenvalue of the equation and the eigenfunction is:

$$\Theta_0 = 1 \qquad (A1.1.5)$$

Also, for $\lambda_0 = 0$ we obtain:

$r^2R_0'' + rR_0' = 0 \Rightarrow$

$\frac{R_0''}{R_0'} = -\frac{1}{r} \Rightarrow$

$\ln(R_0') = -\ln r + c_1 \Rightarrow$

$\ln(R_0') = \ln(e^{c_1}) - \ln(r) \Rightarrow$

$\ln(R_0') = \ln\left(\frac{e^{c_1}}{r}\right) \Rightarrow$

$R_0' = \frac{c}{r} \Rightarrow$

$$R_0(r) = c\ln(r) + c_2 \qquad \text{(A1.1.6)}$$

For $n = 1,2,3, \ldots$ : $\lambda_n = n^2$, so:

$$\Theta'' + n^2\Theta = 0 \qquad \text{(A1.1.7)}$$

The solution of this equation is:

$$\Theta(\theta) = a_n\cos(n\theta) + b_n\sin(n\theta) \qquad \text{(A1.1.8)}$$

Furthermore:

$$r^2R_n'' + rR_n' - n^2R_n = 0 \qquad \text{(A1.1.9)}$$

The solution of the above equation implementing the Frobenius method is:

$R_n = r^s$, so $R_n' = sr^{s-1}$, and $R_n'' = s(s-1)r^{s-2}$

Therefore:

$r^2s(s-1)r^{s-2} + rsr^{s-1} - n^2r^s = 0 \Rightarrow$

$s(s-1) + s - n^2 = 0 \Rightarrow$

$s = \pm n$

As a consequence:

$$R_n(r) = c_1r^n + c_3r^{-n} \qquad \text{(A1.1.10)}$$

As a result, the general solution of the PDE is:

$$\varphi(r,\theta) = R_0\Theta_0 + \sum_{n=1}^{\infty} R_n\Theta_n \qquad \text{(A1.1.11)}$$

## *Appendix A1.2*

For the formation of the magnetization vector in a Fourier Series form the following methodology is implemented:

The period of magnetization is:

$$T_0 = \frac{2\pi}{p} \tag{A1.2.1}$$

Therefore the magnetization vector can be expressed as:

$$M_r(\theta) = \sum_{-\infty}^{+\infty} a_k e^{-i2\pi k f_0 \theta} \tag{A1.2.2}$$

where:

$$a_k = \frac{1}{T_0} \int_{T_0} M_r e^{-i2\pi k f_0 \theta}\, d\theta = \frac{p}{2\pi} \int_{T_0} M_r e^{-ipk\theta}\, d\theta \tag{A1.2.3}$$

If $k = 0$:

$$a_0 = \frac{p}{2\pi} \int_{T_0} M_r e^{0}\, d\theta \Rightarrow a_0 = 0 \tag{A1.2.4}$$

If $k \neq 0$:

$$a_k = \frac{p}{2\pi}\left[\int_{-\frac{\pi}{p}}^{-\frac{\pi}{2p}} -\frac{B_m}{\mu_0} e^{-ipk\theta} d\theta + \int_{-\frac{\pi}{2p}}^{\frac{\pi}{2p}} \frac{B_m}{\mu_0} e^{-ipk\theta} d\theta + \int_{\frac{\pi}{2p}}^{\frac{\pi}{p}} -\frac{B_m}{\mu_0} e^{-ipk\theta} d\theta\right] \Rightarrow$$

$$a_k = \frac{B_m}{\pi\mu_0 k}\left[2\sin\left(\frac{k\pi}{2}\right) - \sin(k\pi)\right]$$

For $k = \pm 1, \pm 2, \pm 3, \ldots : \sin(k\pi) = 0$, so:

$$a_k = \frac{2B_m}{\pi\mu_0 k} \tag{A1.2.5}$$

It can be observed that $a_k = a_{-k}$ , therefore:

$$M_r(\theta) = \sum_{-\infty}^{\infty} a_k e^{ikp\theta} = \sum_{k=1}^{\infty} a_k\left(e^{ipk\theta} + e^{-ipk\theta}\right) \Rightarrow$$

$$M_r(\theta) = \sum_{k=1}^{\infty} \frac{4B_m}{\pi\mu_0 k} \sin\left(\frac{k\pi}{2}\right)\cos(pk\theta) \tag{A1.2.6}$$

$$M_r(\theta) = \sum_{k=1}^{\infty} M_k \cos(pk\theta) \tag{A1.2.7}$$

where:

$$M_k = \frac{4B_m}{\pi\mu_0 k} \sin\left(\frac{k\pi}{2}\right) \tag{A1.2.8}$$

In case of an initial phase angle $\theta_0$ of the inner rotor, the Fourier Series can be written as:

$$M_r(\theta) = \sum_{k=1}^{\infty} M_k \cos\big(pk(\theta - \theta_0)\big) \Rightarrow$$

$$M_r(\theta) = \sum_{k=1}^{\infty} M_k[\cos(pk\theta_0)\cos(pk\theta) + \sin(pk\theta_0)\sin(pk\theta)] \tag{A1.2.9}$$

## *Appendix A1.3*

The Fourier series expansion in the slots has the following form:

$$\varphi^{S}(r,\theta) = a_0 + \sum_{k=1}^{\infty}(a_k \cos(kx) + b_k \sin(kx)) \tag{A1.3.1}$$

which can take the following form:

$$f(x) = a_0 + \sum_{k=1}^{\infty} c_k e^{ikx} \tag{A1.3.2}$$

where:

$$c_k = \begin{cases} a_0, & k = 0 \\ \dfrac{a_k - ib_k}{2}, & k = 1,2,3,\dots \\ \dfrac{a_k + ib_k}{2}, & k = -1,-2,-3,\dots \end{cases} \tag{A1.3.3}$$

Therefore:

$$a_k = 2\mathrm{Re}(c_k) \tag{A1.3.4}$$

$$b_k = -2\mathrm{Im}(c_k) \tag{A1.3.5}$$

The coefficients $a_k$ and $b_k$ will be evaluated for each domain separately.

For $[\alpha_j, \beta_{j+1}]$ the magnetic potential is obtained from the solutions $\varphi_1(r,\theta)$ and $\varphi_2(r,\theta)$ that was previously calculated. The Fourier Series for $\varphi_2(r,\theta)$ can be derived as follows:

For $k = 0$:

$$c_0 = \frac{1}{2\pi}\int_{\alpha_j}^{\beta_{j+1}} \sin\left(\frac{n\pi}{\gamma}(\theta - \alpha_j)\right) e^{-i0\theta} d\theta \Rightarrow$$

$$c_0 = \frac{\gamma}{2n\pi^2}[1 - \cos(n\pi)], \qquad n \in \mathbb{Z} \tag{A1.3.6}$$

since $\gamma = \beta_{j+1} - \alpha_j$. The term $X_n r^{\frac{n\pi}{\gamma}} + Y_n r^{-\frac{n\pi}{\gamma}}$ has been neglected because it is constant and will be added in the end.

For $k \neq \frac{n\pi}{\gamma}$:

$$c_k = \frac{1}{2\pi}\int_{\alpha_j}^{\beta_{j+1}} \sin\left(\frac{n\pi}{\gamma}(\theta - \alpha_j)\right) e^{-ik\theta} d\theta \Rightarrow$$

$$c_k = \frac{\frac{n\pi}{\gamma k^2}\left[\cos(n\pi)\cos\left(k\beta_{j+1}\right) - \cos\left(k\alpha_j\right) - i\left(\cos(n\pi)\sin\left(k\beta_{j+1}\right) - \sin\left(k\alpha_j\right)\right)\right]}{2\pi\left(1 - \frac{n^2\pi^2}{\gamma^2 k^2}\right)} \quad \text{(A1.3.7)}$$

Therefore:

$$a_k = 2\mathrm{Re}(c_k) = \frac{\frac{n\pi}{\gamma}\left[\cos(n\pi)\cos\left(k\beta_{j+1}\right) - \cos\left(k\alpha_j\right)\right]}{\pi\left(k^2 - \frac{n^2\pi^2}{\gamma^2}\right)} \quad \text{(A1.3.8)}$$

$$\beta_k = -2\mathrm{Im}(c_k) = \frac{\frac{n\pi}{\gamma}\left[\cos(n\pi)\sin\left(k\beta_{j+1}\right) - \sin\left(k\alpha_j\right)\right]}{\pi\left(k^2 - \frac{n^2\pi^2}{\gamma^2}\right)} \quad \text{(A1.3.9)}$$

For $k = \pm\frac{n\pi}{\gamma}$:

$$c_k = \frac{1}{2\pi}\int_{\alpha_j}^{\beta_{j+1}} \sin\left(\frac{n\pi}{\gamma}\left(\theta - \alpha_j\right)\right)e^{-ik\theta}d\theta \Rightarrow$$

$$c_k = -\frac{\gamma}{4\pi}\left(\sin\left(k\alpha_j\right) + i\cos\left(k\alpha_j\right)\right) \quad \text{(A1.3.10)}$$

Therefore:

$$a_k = 2\mathrm{Re}(c_k) = -\frac{\gamma}{2\pi}\sin\left(k\alpha_j\right) \quad \text{(A1.3.11)}$$

$$b_k = -2\mathrm{Im}(c_k) = \frac{\gamma}{2\pi}\cos\left(k\alpha_j\right) \quad \text{(A1.3.12)}$$

So, $\varphi_2(r,\theta)$ can be expanded in Fourier Series in all domains, so as a continuous function to be derived:

$$\varphi_2(r,\theta) = \frac{a_0}{2} + \sum_{k=1}^{\infty}\left(a_k\cos(k\theta) + b_k\sin(k\theta)\right) \quad \text{(A1.3.13)}$$

$a_0, a_k, b_k$ can be evaluated from the following equations:

$$a_0 = \sum_{j=1}^{N}\sum_{n=1}^{\infty}\frac{\gamma(1-\cos(n\pi))\left(X_{jn}r^{\frac{n\pi}{\gamma}} + Y_{jn}r^{\frac{-n\pi}{\gamma}}\right)}{n\pi^2} \quad \text{(A1.3.14)}$$

$$a_k = \sum_{j=1}^{N}\sum_{n=1}^{\infty}\frac{\tau_{knj}\left(X_{jn}r^{\frac{n\pi}{\gamma}} + Y_{jn}r^{\frac{-n\pi}{\gamma}}\right)}{\pi} \quad \text{(A1.3.15)}$$

$$b_k = \sum_{j=1}^{N} \sum_{n=1}^{\infty} \frac{\omega_{knj} \left( X_{jn} r^{\frac{n\pi}{\gamma}} + Y_{jn} r^{\frac{-n\pi}{\gamma}} \right)}{\pi} \tag{A1.3.16}$$

where:

$$\tau_{nkj} = \begin{cases} \dfrac{\frac{n\pi}{\gamma} [\cos(n\pi) \cos(k\beta_{j+1}) - \cos(k\alpha_j)]}{k^2 - \frac{n^2\pi^2}{\gamma^2}} & k \neq \frac{n\pi}{\gamma} \\ -\frac{\gamma}{2} \sin(k\alpha_j) & k = \frac{n\pi}{\gamma} \end{cases} \tag{A1.3.17}$$

$$\omega_{nkj} = \begin{cases} \dfrac{\frac{n\pi}{\gamma} [\cos(n\pi) \sin(k\beta_{j+1}) - \sin(k\alpha_j)]}{k^2 - \frac{n^2\pi^2}{\gamma^2}} & k \neq \frac{n\pi}{\gamma} \\ \frac{\gamma}{2} \cos(k\alpha_j) & k = \frac{n\pi}{\gamma} \end{cases} \tag{A1.3.18}$$

Additionally, $\varphi_1(r, \theta)$ and $\varphi_j^F$ can be expanded into Fourier Series as follows:

For $k = 0$:

$$c_{0,j} = \frac{1}{2\pi} \int_{\alpha_j}^{\beta_{j+1}} \left[ \frac{\varphi_{j+1}^F - \varphi_j^F}{\gamma} (\theta - \alpha_j) + \varphi_j^F \right] d\theta + \int_{\beta_j}^{\alpha_j} \varphi_j^F d\theta \tag{A1.3.19}$$

$$c_{0,j} = \frac{\varphi_{j+1}^F + \varphi_j^F}{4\pi} \gamma + \varphi_j^F \delta \tag{A1.3.20}$$

The sum for N slots yields:

$$c_0 = \frac{1}{2\pi} \sum_{j=1}^{N} \varphi_j^F (\gamma + \delta) \tag{A1.3.21}$$

For $k \neq 0$, $\varphi_1(r, \theta)$ can be expanded in Fourier Series as follows:

$$c_{k,j} = \frac{1}{2\pi} \int_{\alpha_j}^{\beta_{j+1}} \left( \frac{\varphi_{j+1}^F - \varphi_j^F}{\gamma} (\theta - \alpha_j) + \varphi_j^F \right) e^{-ik\theta} d\theta \Rightarrow$$

$$c_{k,j} = \frac{\varphi_{j+1}^F}{2\pi k}\left[i\cos\left(k\beta_{j+1}\right) + \sin\left(k\beta_{j+1}\right)\right] - \frac{\varphi_j^F}{2\pi k}\left[\sin\left(k\alpha_j\right) + i\cos\left(k\alpha_j\right)\right]$$
$$- \frac{\varphi_{j+1}^F - \varphi_j^F}{\gamma k^2}\left[2\sin\left(\frac{k\gamma}{2}\right)\sin\left(k\frac{\beta_{j+1}+\alpha_j}{2}\right)\right.$$
$$\left. + 2i\sin\left(\frac{k\gamma}{2}\right)\cos\left(k\frac{\beta_{j+1}+\alpha_j}{2}\right)\right] \qquad \text{(A1.3.22)}$$

Following the same process, the Fourier Series coefficients for the ferromagnetic segments ($\varphi_j^F$) can be calculated:

$$c_{k,j} = \frac{1}{2\pi}\int_{\beta_j}^{\alpha_j} \varphi_j^F e^{-ik\theta} d\theta \Rightarrow$$

$$c_{k,j} = \frac{\varphi_j^F}{2k\pi}\left(\sin\left(k\alpha_j\right) + i\cos\left(k\alpha_j\right) - \sin\left(k\beta_j\right) - i\cos\left(k\beta_j\right)\right) \qquad \text{(A1.3.23)}$$

From the sum of the coefficients of $\varphi_1(r,\theta)$ and $\varphi_j^F$ in the ferromagnetic segments we obtain:

$$c_k = \sum_{j=1}^{N} \frac{\varphi_j^F - \varphi_{j+1}^F}{2\pi\gamma k^2}\left[2\sin\left(\frac{k\gamma}{2}\right)\sin\left(k\frac{\beta_{j+1}+\alpha_j}{2}\right)\right.$$
$$\left. + 2i\sin\left(\frac{k\gamma}{2}\right)\cos\left(k\frac{\beta_{j+1}+\alpha_j}{2}\right)\right] \qquad \text{(A1.3.24)}$$

Therefore:

$$a_k = 2\mathrm{Re}(c_k) = \sum_{j=1}^{N} \frac{2\left(\varphi_j^F - \varphi_{j+1}^F\right)}{\pi\gamma k^2}\sin\left(\frac{k\gamma}{2}\right)\sin\left(k\frac{\beta_{j+1}+\alpha_j}{2}\right) \qquad \text{(A1.3.25)}$$

$$b_k = -2\mathrm{Im}(c_k) = \sum_{j=1}^{N} \frac{2\left(\varphi_j^F - \varphi_{j+1}^F\right)}{\pi\gamma k^2}\sin\left(\frac{k\gamma}{2}\right)\cos\left(k\frac{\beta_{j+1}+\alpha_j}{2}\right) \qquad \text{(A1.3.26)}$$

Overall, the coefficients $a_0$, $a_k$ and $b_k$ for the expansion of the magnetic potential the slots, in Fourier Series can be calculated as the sum of the coefficients for $\varphi_2(r,\theta)$, $\varphi_1(r,\theta)$ and $\varphi_j^F$:

$$a_0 = \frac{1}{\pi}\left[\sum_{j=1}^{N}\sum_{n=1}^{\infty} \frac{\gamma(1-\cos(n\pi))\left(X_{jn} r^{\frac{n\pi}{\gamma}} + Y_{jn} r^{\frac{-n\pi}{\gamma}}\right)}{n\pi} + \sum_{j=1}^{N}(\gamma+\delta)\varphi_j^F\right] \qquad \text{(A1.3.27)}$$

$$a_k = \sum_{j=1}^{N}\sum_{n=1}^{\infty}\frac{\tau_{knj}}{\pi}\left(X_{jn}r^{\frac{n\pi}{\gamma}} + Y_{jn}r^{\frac{-n\pi}{\gamma}}\right) - \sum_{j=1}^{N}\frac{2\left(\varphi_j^F + \varphi_{j+1}^F\right)}{\pi\gamma k^2}\sin\left(\frac{k\gamma}{2}\right)\sin\left(k\frac{\beta_{j+1}+\alpha_j}{2}\right) \quad \text{(A1.3.28)}$$

$$b_k = \sum_{j=1}^{N}\sum_{n=1}^{\infty}\frac{\omega_{knj}}{\pi}\left(X_{jn}r^{\frac{n\pi}{\gamma}} + Y_{jn}r^{\frac{-n\pi}{\gamma}}\right) + \sum_{j=1}^{N}\frac{2\left(\varphi_j^F + \varphi_{j+1}^F\right)}{\pi\gamma k^2}\sin\left(\frac{k\gamma}{2}\right)\cos\left(k\frac{\beta_{j+1}+\alpha_j}{2}\right) \quad \text{(A1.3.29)}$$

where:

$$\tau_{nkj} = \begin{cases} \dfrac{\frac{n\pi}{\gamma}\left[\cos(n\pi)\cos\left(k\beta_{j+1}\right) - \cos\left(k\alpha_j\right)\right]}{k^2 - \frac{n^2\pi^2}{\gamma^2}} & k \neq \dfrac{n\pi}{\gamma} \\ -\dfrac{\gamma}{2}\sin\left(k\alpha_j\right) & k = \dfrac{n\pi}{\gamma} \end{cases} \quad \text{(A1.3.30)}$$

$$\omega_{nkj} = \begin{cases} \dfrac{\frac{n\pi}{\gamma}\left[\cos(n\pi)\sin\left(k\beta_{j+1}\right) - \sin\left(k\alpha_j\right)\right]}{k^2 - \frac{n^2\pi^2}{\gamma^2}} & k \neq \dfrac{n\pi}{\gamma} \\ \dfrac{\gamma}{2}\cos\left(k\alpha_j\right) & k = \dfrac{n\pi}{\gamma} \end{cases} \quad \text{(A1.3.31)}$$

## *Appendix A1.4*

From the Lorenz force equation:

$$\mathbf{f} = \rho\mathbf{E} + \mathbf{J} \times \mathbf{B} \tag{A1.4.1}$$

and from the Maxwell laws:

$$\nabla \cdot \mathbf{E} = \frac{\rho}{\mathrm{E}_0} \Rightarrow \rho = \mathrm{E}_0(\nabla \cdot \mathbf{E}) \tag{A1.4.2}$$

and:

$$\nabla \cdot \mathbf{B} = \mu_0\mathbf{J} + \mu_0\mathrm{E}_0\frac{\partial \mathbf{E}}{\partial \mathrm{t}} \Rightarrow$$

$$\mathbf{J} = \frac{\nabla \times \mathbf{B}}{\mu_0} - \mathrm{E}_0\frac{\partial \mathbf{E}}{\partial \mathrm{t}} \tag{A1.4.3}$$

From Eq.(A1.4.1)-(A1.4.3) the following relation is obtained:

$$\mathbf{f} = \mathrm{E}_0(\nabla \cdot \mathbf{E})\mathbf{E} + \frac{1}{\mu_0}(\nabla \times \mathbf{B}) \times \mathbf{B} - \mathrm{E}_0\frac{\partial \mathbf{E}}{\partial \mathrm{t}} \times \mathbf{B} \tag{A1.4.4}$$

Furthermore:

$$\frac{\partial}{\partial \mathrm{t}}(\mathbf{E} \times \mathbf{B}) = \frac{\partial \mathbf{E}}{\partial \mathrm{t}} \times \mathbf{B} + \mathbf{E} \times \frac{\partial \mathbf{B}}{\partial \mathrm{t}} \Rightarrow$$

$$\frac{\partial}{\partial \mathrm{t}}(\mathbf{E} \times \mathbf{B}) = \frac{\partial \mathbf{E}}{\partial \mathrm{t}} \times \mathbf{B} - \mathbf{E} \times (\nabla \times \mathbf{E}) \tag{A1.4.5}$$

Therefore from Eq.(A1.4.4) and Eq.(A1.4.5):

$$\mathbf{f} = \mathrm{E}_0(\nabla \cdot \mathbf{E})\mathbf{E} + \frac{1}{\mu_0}(\nabla \times \mathbf{B}) \times \mathbf{B} - \mathrm{E}_0\frac{\partial}{\partial \mathrm{t}}(\mathbf{E} \times \mathbf{B}) - \mathrm{E}_0\mathbf{E}(\nabla \times \mathbf{E}) \Rightarrow$$

$$\mathbf{f} = \mathrm{E}_0\left[(\nabla \cdot \mathbf{E})\mathbf{E} + (\mathbf{E} \cdot \nabla)\mathbf{E} - \frac{1}{2}\nabla\mathbf{E}^2\right] + \frac{1}{\mu_0}\left[(\nabla \cdot \mathbf{B})\mathbf{B} + (\mathbf{B} \cdot \nabla)\mathbf{B} - \frac{1}{2}\nabla\mathbf{B}^2\right]$$
$$- \mathrm{E}_0\frac{\partial}{\partial \mathrm{t}}(\mathbf{E} \times \mathbf{B}) \tag{A1.4.6}$$

## *Appendix A1.5*

The divergence of the Maxwell Stress Tensor on the i component is:

$$\left(\nabla_i \cdot \overleftrightarrow{\mathbf{T}}_{\mathbf{ij}}\right)_j = \sum_{i=r,\theta,z} \nabla_i T_{ij} = \sum_{i=r,\theta,z} \nabla_i \left[E_0 \left(E_i E_j - \frac{1}{2}\delta_{ij}E^2\right) + \frac{1}{\mu_0}\left(B_i B_j - \frac{1}{2}\delta_{ij}B^2\right)\right] \Rightarrow$$

$$\left(\nabla_i \cdot \overleftrightarrow{\mathbf{T}}_{\mathbf{ij}}\right)_j = E_0 \left[(\nabla \cdot \mathbf{E})E_j + (\mathbf{E} \cdot \nabla)E_j - \frac{1}{2}\nabla_j \mathbf{E}^2\right]$$

$$+ \frac{1}{\mu_0}\left[(\nabla \cdot \mathbf{B})B_j + (\mathbf{B} \cdot \nabla)B_j - \frac{1}{2}\nabla_j \mathbf{B}^2\right] \quad \text{(A1.5.1)}$$

And as a consequence:

$$\left(\nabla \cdot \overleftrightarrow{\mathbf{T}}\right) = E_0 \left[(\nabla \cdot \mathbf{E})\mathbf{E} + (\mathbf{E} \cdot \nabla)\mathbf{E} - \frac{1}{2}\nabla \mathbf{E}^2\right]$$

$$+ \frac{1}{\mu_0}\left[(\nabla \cdot \mathbf{B})\mathbf{B} + (\mathbf{B} \cdot \nabla)\mathbf{B} - \frac{1}{2}\nabla \mathbf{B}^2\right] \quad \text{(A1.5.2)}$$

Therefore:

$$\mathbf{f} = \nabla \cdot \overleftrightarrow{\mathbf{T}} - E_0 \mu_0 \frac{\partial \mathbf{S}}{\partial t} \quad \text{(A1.5.3)}$$

The force can be calculated as:

$$\mathbf{F} = \int_V \mathbf{f}\, dV = \int_V \nabla \cdot \overleftrightarrow{\mathbf{T}}\, dV - E_0 \mu_0 \int_V \frac{\partial \mathbf{S}}{\partial t} dV \quad \text{(A1.5.4)}$$

Using the Gauss theorem of divergence:

$$\mathbf{F} = \oint_S \overleftrightarrow{\mathbf{T}} d\mathbf{a} - E_0 \mu_0 \int_V \frac{\partial \mathbf{S}}{\partial t} dV \quad \text{(A1.5.5)}$$

Since the model is in 2D and $\mathbf{E} = 0$. As a consequence, the Maxwell Stress Tensor is:

$$T_{ij} = \frac{1}{\mu_0} B_i B_j - \frac{1}{2\mu_0} B^2 \delta_{ij} \quad \text{(A1.5.6)}$$

where:

$$B^2 = B_r^2 + B_\theta^2 \quad \text{(A1.5.7)}$$

Hence, the Maxwell Stress Tensor can be written as:

$$\overleftrightarrow{\mathbf{T}} = \frac{1}{\mu_0}\begin{bmatrix} \frac{B_r^2 - B_\theta^2}{2} & B_r B_\theta \\ B_\theta B_r & \frac{B_\theta^2 - B_r^2}{2} \end{bmatrix} \quad \text{(A1.5.8)}$$

## *Appendix A1.6*

The calculation of the torque in the inner and outer rotor respectively consists of two sums of integrals in the following form:

$$I = \mu_0^2 \int_0^{2\pi} \left\{ \sum_{n=1}^{\infty} P_n \cos(n\theta) + Q_n \sin(n\theta) + \frac{E_0}{\ln r_2} \right\} \left\{ \sum_{n=1}^{\infty} R_n \sin(n\theta) + S_n \cos(n\theta) \right\} d\theta \quad \text{(A1.6.1)}$$

Since:

$$B_r = -\mu_0 \left\{ \sum_{n=1}^{\infty} P_n \cos(n\theta) + Q_n \sin(n\theta) + \frac{E_0}{\ln r_2} \right\} \quad \text{(A1.6.2)}$$

$$B_\theta = -\mu_0 \left\{ \sum_{n=1}^{\infty} R_n \sin(n\theta) + S_n \cos(n\theta) \right\} \quad \text{(A1.6.3)}$$

The above integral can be simplified to:

$$I = \pi \mu_0 L r_2^2 \sum_{n=1}^{\infty} (P_n S_n + Q_n R_n) \quad \text{(A1.6.4)}$$

since:

$$\int_0^{2\pi} \cos(n\theta) \sin(m\theta)\, d\theta = 0 \quad \forall\, n, m \quad \text{(A1.6.5)}$$

$$\int_0^{2\pi} \cos(n\theta) \cos(m\theta)\, d\theta = \begin{cases} 0, & n \neq m \\ \pi, & n = m \end{cases} \quad \text{(A1.6.6)}$$

$$\int_0^{2\pi} \sin(n\theta) \sin(m\theta)\, d\theta = \begin{cases} 0, & n \neq m \\ \pi, & n = m \end{cases} \quad \text{(A1.6.7)}$$

$$\int_0^{2\pi} [\cos(n\theta) + \sin(n\theta)] d\theta = 0 \quad \forall\, n \quad \text{(A1.6.8)}$$

Therefore the analytical form of $M_{in}(r_2)$ is:

$$M_{in}(r_2) = \pi \mu_0 L r_2^2 \sum_{n=1}^{\infty} [\, (P_{n,out} S_{n,in} + Q_{n,out} R_{n,in}) + (P_{n,in} S_{n,out} + Q_{n,in} R_{n,out})] \quad \text{(A1.6.9)}$$

where:

$$P_{n,in} = n(E_{n,in} r_2^{n-1} - F_{n,in} r_2^{-n-1}) \quad \text{(A1.6.10)}$$

$$Q_{n,in} = n(G_{n,in}r_2^{n-1} - H_{n,in}r_2^{-n-1}) \quad \text{(A1.6.11)}$$

$$R_{n,in} = -n(E_{n,in}r_2^{n-1} + F_{n,in}r_2^{-n-1}) \quad \text{(A1.6.12)}$$

$$S_{n,in} = n(G_{n,in}r_2^{n-1} + H_{n,in}r_2^{-n-1}) \quad \text{(A1.6.13)}$$

$$P_{n,out} = n(E_{n,out}r_2^{n-1} - F_{n,out}r_2^{-n-1}) \quad \text{(A1.6.14)}$$

$$Q_{n,out} = n(G_{n,out}r_2^{n-1} - H_{n,out}r_2^{-n-1}) \quad \text{(A1.6.15)}$$

$$R_{n,out} = -n(E_{n,out}r_2^{n-1} + F_{n,out}r_2^{-n-1}) \quad \text{(A1.6.16)}$$

$$S_{n,out} = n(G_{n,out}r_2^{n-1} + H_{n,out}r_2^{-n-1}) \quad \text{(A1.6.17)}$$

## *Chapter 1-References*

[1.1] Jian, L., & Chau, K. T. (2009). Analytical calculation of magnetic field distribution in coaxial magnetic gears. *Progress In Electromagnetics Research*, *92*, 1-16.

[1.2] Elia, S., Pasquali, M., Remigi, G., Sabene, M. V., & Santini, E. (2001). A modified Maxwell stress tensor method for the evaluation of electromagnetic torque. WIT Transactions on Engineering Sciences, 31.

[1.3] Ye, Q., & Lin, H. (2017). On deriving the Maxwell stress tensor method for calculating the optical force and torque on an object in harmonic electromagnetic fields. European Journal of Physics, 38(4), 045202.

[1.4] Tzouganakis, P., Gakos, V., Kalligeros, C., Tsolakis, A., & Spitas, V. (2023). Fast and efficient simulation of the dynamical response of coaxial magnetic gears through direct analytical torque modelling. Simulation Modelling Practice and Theory, 123, 102699.

[1.5] Jian, L., & Chau, K. T. (2010). A coaxial magnetic gear with Halbach permanent-magnet arrays. IEEE Transactions on Energy conversion, 25(2), 319-328.

# 2 Halbach-Array Coaxial Magnetic Gears

CMG performance can be further improved if the permanent magnets (PMs) are placed in a specific arrangement called Halbach-array [2.1]-[2.4]. Halbach-arrays can create a strong magnetic field [2.5] due to their inherent capability to generate one-sided magnetic field [2.6]. The Halbach-array CMG (HAL-CMG) drive has higher torque density, superior dynamical response under load and good self-shielding magnetization [2.7]-[2.10]. However these drives, insert further parameters in the optimization process, making the problem of increasing the torque density computationally intensive. Therefore, an analytical calculation of the torque would significantly reduce the computational cost required to achieve optimal torque density for a given configuration of the HAL-CMG drive and in general would facilitate the design of application-specific HAL-CMG drives.

In the present chapter a novel analytical 2D model for the calculation of the magnetic potential for every rotation angle, geometry configuration and constitutive parameters of the magnets of the HAL-CMG drive has been derived. The applied torque on the two rotors and the torque ripple were calculated analytically from the Maxwell Stress Tensor. A case study was performed for a 4 pole pair inner rotor and a 10 pole pair outer rotor in a standard CMG and an optimised HAL-CMG with the same geometrical and parameters of the PMs. The stall torque and the amplitude of the harmonics contributing to the torque ripple were calculated and compared for the two drives. In addition, the obtained torques were verified with Finite Element Analysis (FEA). The stall torque of the HAL-CMG was 14.3% higher than the standard CMG's while the amplitudes of the torque contributing harmonics which generate torque ripple were slightly reduced.

## 2.1 Analytical model of Halbach-array CMG drives

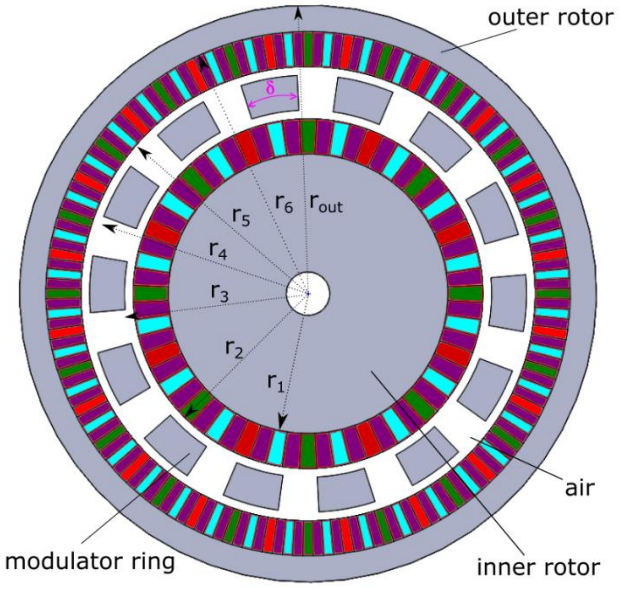


**Figure 2.1: Halbach-array Coaxial Magnetic Gear**

The three components of the HAL-CMG are: the inner rotor, the outer rotor and the flux modulator ring. As shown in Fig.2.1, $r_1, r_2, r_3, r_4, r_5, r_6, r_{out}$ are the radii of the inner iron yoke, the inner PMs, the inner and the outer side of the modulator ring, the outer PMs, the outer iron yoke and the external side of the HAL-CMG respectively. In addition, $\alpha_j$ and $\beta_j$ are the right and left border of the $j^{th}$ ferromagnetic segment. The basic geometric parameters of the HAL-CMG are therefore similar to the standard CMG. The different colors of the PMs represent the different orientations of the magnets.

In Fig.2.2, a linear analogue of the HAL-CMG shown in Fig.2.1 with PMs only on the inner rotor is presented.

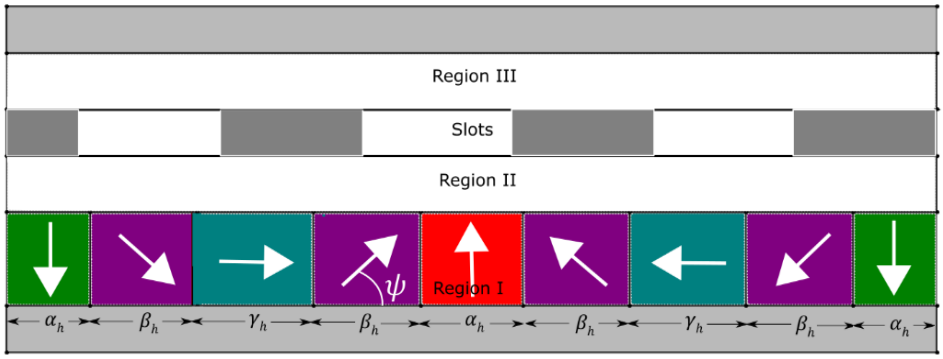


**Figure 2.2: Linear analogue of a section of HAL-CMG (one pole-pair)**

The magnetic induction of the HAL-CMG is obtained as a superposition of the magnetic inductions generated by the PMs of the inner and outer rotor separately. In order to obtain an analytical solution, infinite permeability of the iron yokes and the ferromagnetic segments is assumed, similar to the standard CMG.

The only difference in terms of modelling between the standard and Halbach-array CMG is at the magnetization vector of the PMs and as a result at the general solution of the Region I for the magnetic potential. The magnetization vector in this case can be written as:

$$\mathbf{M} = M_r \mathbf{r} + M_\theta \boldsymbol{\theta} \tag{2.1}$$

In order to obtain the special solution, the magnetization distribution should be expressed in an analytical and continuous function. $M_r$ (radial) and $M_\theta$ (tangential) magnetization distributions are presented in Fig.2.3 and Fig. 2.4.

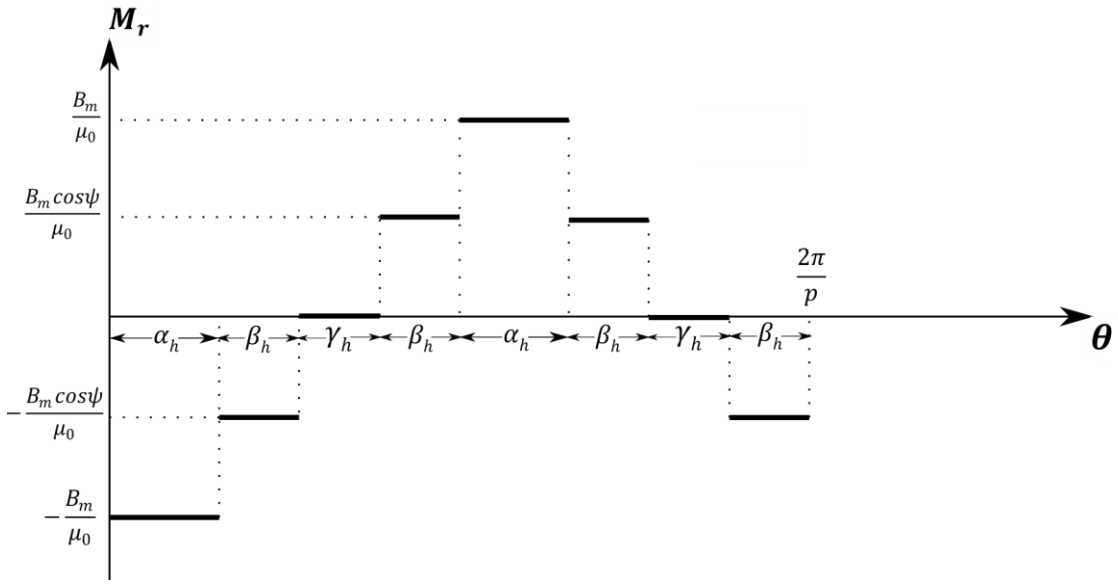


**Figure 2.3: Radial magnetization distribution in Region I**

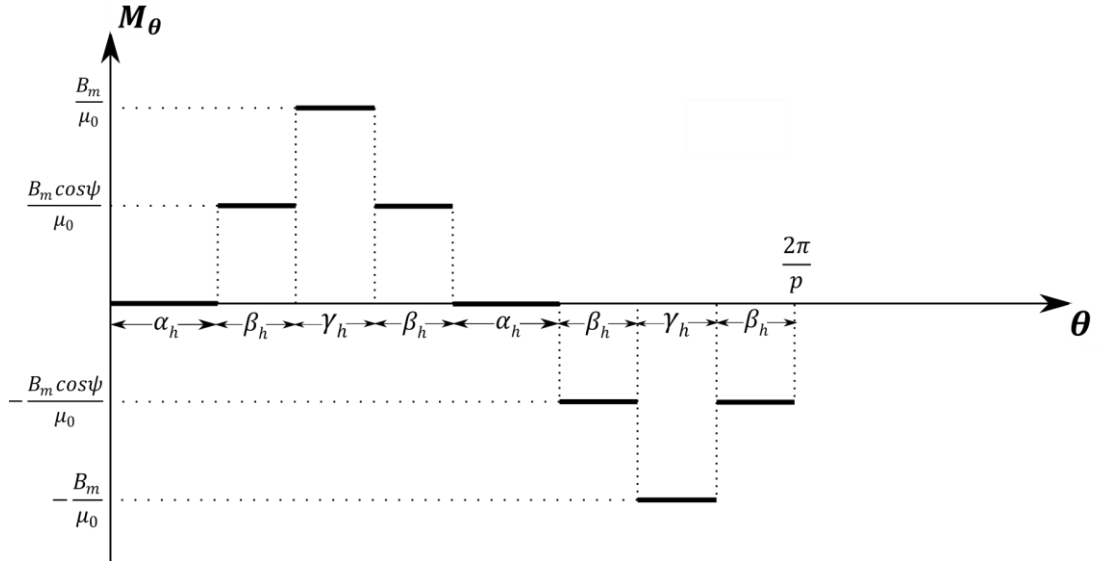


**Figure 2.4: Tangential magnetization distribution in Region I**

where p is the number of pole pairs, $B_m$ is the residual magnetism of the PM and $\alpha_h, \beta_h, \gamma_h, \psi$ are the PMs' angles of Fig. 2.2.

The magnetization can be described in an analytical and continuous form with Fourier series as shown in Appendix A2.1. Therefore, the magnetization can be obtained from:

$$M_r(\theta) = \sum_{k=1}^{\infty} a_k \cos\big(pk(\theta - \theta_0)\big) + b_k \sin\big(pk(\theta - \theta_0)\big) \quad (2.2)$$

$$M_\theta(\theta) = \sum_{k=1}^{\infty} d_k \cos\big(pk(\theta - \theta_0)\big) + e_k \sin\big(pk(\theta - \theta_0)\big) \quad (2.3)$$

where $\theta_0$ is an initial phase angle and

$$\begin{aligned} a_k = \frac{B_m}{\pi\mu_0 k}\big[&-\sin(kp\alpha_h) - \sin\psi\big(\sin\big(kp(\alpha_h+\beta_h)\big) - \sin(kp\alpha_h)\big) \\ &+ \sin\psi\big(\sin\big(kp(\alpha_h+2\beta_h+\gamma_h)\big) - \sin\big(kp(\alpha_h+\beta_h+\gamma_h)\big)\big) \\ &+ \sin\big(kp(2\alpha_h+2\beta_h+\gamma_h)\big) - \sin\big(kp(\alpha_h+2\beta_h+\gamma_h)\big) \\ &+ \sin\psi\big(\sin\big(kp(2\alpha_h+3\beta_h+\gamma_h)\big) \\ &- \sin\big(kp(2\alpha_h+2\beta_h+\gamma_h)\big)\big) \\ &- \sin\psi\big(\sin\big(kp(2\alpha_h+4\beta_h+2\gamma_h)\big) \\ &- \sin\big(kp(2\alpha_h+3\beta_h+2\gamma_h)\big)\big)\big] \end{aligned} \tag{2.4}$$

$$\begin{aligned} b_k = -\frac{B_m}{\pi\mu_0 k}\big[&-\cos(kp\alpha_h) - \cos(0) \\ &- \sin\psi\big(\cos\big(kp(\alpha_h+\beta_h)\big) - \cos(kp\alpha_h)\big) \\ &+ \sin\psi\big(\cos\big(kp(\alpha_h+2\beta_h+\gamma_h)\big) \\ &- \cos\big(kp(\alpha_h+\beta_h+\gamma_h)\big)\big) + \cos\big(kp(2\alpha_h+2\beta_h+\gamma_h)\big) \\ &- \cos\big(kp(\alpha_h+2\beta_h+\gamma_h)\big) \\ &+ \sin\psi\big(\cos\big(kp(2\alpha_h+3\beta_h+\gamma_h)\big) \\ &- \cos\big(kp(2\alpha_h+2\beta_h+\gamma_h)\big)\big) \\ &- \sin\psi\big(\cos\big(kp(2\alpha_h+4\beta_h+2\gamma_h)\big) \\ &- \cos\big(kp(2\alpha_h+3\beta_h+2\gamma_h)\big)\big)\big] \end{aligned} \tag{2.5}$$

$$\begin{aligned} d_k = \frac{B_m}{\pi\mu_0 k}\big[&\cos\psi\big(\sin\big(kp(\alpha_h+\beta_h)\big) - \sin(kp\alpha_h)\big) \\ &+ \sin\big(kp(\alpha_h+\beta_h+\gamma_h)\big) - \sin\big(kp(\alpha_h+\beta_h)\big) \\ &+ \cos\psi\big(\sin\big(kp(\alpha_h+2\beta_h+\gamma_h)\big) - \sin\big(kp(\alpha_h+\beta_h+\gamma_h)\big)\big) \\ &- \cos\psi\big(\sin\big(kp(2\alpha_h+3\beta_h+\gamma_h)\big) \\ &- \sin\big(kp(2\alpha_h+2\beta_h+\gamma_h)\big)\big) - \sin\big(kp(2\alpha_h+3\beta_h+2\gamma_h)\big) \\ &- \sin\big(kp(2\alpha_h+3\beta_h+\gamma_h)\big) \\ &- \cos\psi\big(\sin\big(kp(2\alpha_h+4\beta_h+2\gamma_h)\big) \\ &- \sin\big(kp(2\alpha_h+3\beta_h+2\gamma_h)\big)\big)\big] \end{aligned} \tag{2.6}$$

$$
\begin{aligned}
e_k = -\frac{B_m}{\pi\mu_0 k}\big[&\cos\psi\big(\cos\big(kp(\alpha_h+\beta_h)\big)-\cos(kp\alpha_h)\big)\\
&+\cos\big(kp(\alpha_h+\beta_h+\gamma_h)\big)-\cos\big(kp(\alpha_h+\beta_h)\big)\\
&+\cos\psi\big(\cos\big(kp(\alpha_h+2\beta_h+\gamma_h)\big)\\
&-\cos\big(kp(\alpha_h+\beta_h+\gamma_h)\big)\big)\\
&-\cos\psi\big(\cos\big(kp(2\alpha_h+3\beta_h+\gamma_h)\big)\\
&-\cos\big(kp(2\alpha_h+2\beta_h+\gamma_h)\big)\big)-\cos\big(kp(2\alpha_h+3\beta_h+2\gamma_h)\big)\\
&-\cos\big(kp(2\alpha_h+3\beta_h+\gamma_h)\big)\\
&-\cos\psi\big(\cos\big(kp(2\alpha_h+4\beta_h+2\gamma_h)\big)\\
&-\cos\big(kp(2\alpha_h+3\beta_h+2\gamma_h)\big)\big)\big]
\end{aligned}
\tag{2.7}
$$

Therefore the divergence of the magnetization vector in a Halbach-array is:

$$
\frac{\mathrm{div}\mathbf{M}}{\mu_r}=\frac{1}{\mu_r}\left[\frac{1}{r}\frac{\partial}{\partial r}(rM_r)+\frac{1}{r}\frac{\partial}{\partial\theta}(M_\theta)\right] \tag{2.8}
$$

Which yields:

$$
\begin{aligned}
\frac{\mathrm{div}\mathbf{M}}{\mu_r}=\frac{1}{r\mu_r}\Bigg(&\sum_{k=1}^{\infty}[(a_k\cos(pk\theta_0)-b_k\sin(pk\theta_0))\cos(pk\theta)\\
&+(a_k\sin(pk\theta_0)+b_k\cos(pk\theta_0))\sin(pk\theta)]\\
&+\sum_{k=1}^{\infty}\{d_k[-pk\sin(pk\theta)\cos(pk\theta_0)\\
&+pk\cos(pk\theta)\sin(pk\theta_0)]\\
&+e_k[pk\cos(pk\theta)\cos(pk\theta_0)+pk\sin(pk\theta)\sin(pk\theta_0)]\}\Bigg)
\end{aligned}
\tag{2.9}
$$

Therefore, the PDE in Region I is:

$$
\varphi_{rr}+\frac{1}{r}\varphi_r+\frac{1}{r^2}\varphi_{\theta\theta}=\frac{\mathrm{div}\mathbf{M}}{\mu_r} \tag{2.10}
$$

The special solution will have the following form:

$$\varphi_s(r,\theta)=\sum_{k=1}^{\infty}\{W_k(r)[(a_k\cos(pk\theta_0)-b_k\sin(pk\theta_0)+d_k pk\sin(pk\theta_0)+e_k pk\cos(pk\theta_0))\cos(pk\theta)+(a_k\sin(pk\theta_0)+b_k\cos(pk\theta_0)-d_k\,pk\cos(pk\theta_0)+e_k\,pk\sin(pk\theta_0))\sin(pk\theta)]\} \tag{2.11}$$

Therefore, the PDE takes the following form:

$$\ddot{W}_k(r)+\frac{1}{r}\dot{W}_k(r)-\frac{(pk)^2}{r^2}W_k(r)=\frac{M_k}{\mu_r} \tag{2.12}$$

which yields that:

$$W_k(r)=\begin{cases}\dfrac{r}{\mu_r(1-(pk)^2)}, & \text{if } pk\neq 1\\ \dfrac{r\ln r}{2\mu_r}, & \text{if } p=k=1\end{cases} \tag{2.13}$$

Therefore, the general solution in Region I is:

$$\varphi^I(r,\theta)=\sum_{n=1}^{\infty}\Big[\big(A_n r^n+B_n r^{-n}+W_n(r)(a_n\cos(n\theta_0)-b_n\sin(n\theta_0)+d_n\,n\sin(n\theta_0)+e_n\,n\cos(n\theta_0))\big)\cos(n\theta)+\big(C_n r^n+D_n r^{-n}+W_n(r)(a_n\sin(n\theta_0)+b_n\cos(n\theta_0)-d_n\,n\cos(n\theta_0)+e_n\,n\sin(n\theta_0))\big)\sin(n\theta)\Big]+A_0\ln r+B_0 \tag{2.14}$$

where:

$$W_n(r)=\begin{cases}\dfrac{r}{\mu_r(1-n^2)}, & \text{if } n=pk,\ \ k=1,3,5,\ldots\\ \dfrac{r\ln r}{2\mu_r}, & \text{if } n=pk=1\end{cases} \tag{2.15}$$

The remaining of the methodology is identical to the one followed for the standard CMG. A linear system of equations is formed and the coefficients are calculated. Therefore, an analytical method for magnetic induction calculation in Halbach-array CMG drives have been developed. Then, following a similar process as in Chapter 1 the torque can be calculated in every angle of rotation of the two rotors.

## *2.2 Optimization of HAL-CMG and comparison with standard CMG*

To illustrate the improvement in the torque density that is achieved with the use of HAL-CMG drives, a case study was performed for a standard CMG and a HAL-CMG drive with the same geometrical and constitutive parameters of the PMs as it is presented in Table 2.1.

**Table 2.1: Geometrical Parameters**

| | |
|---|---|
| $p_{in}$ | 4 |
| $p_{out}$ | 10 |
| $r_1$ [mm] | 80 |
| $r_2$ [mm] | 100 |
| $r_3$ [mm] | 105 |
| $r_4$ [mm] | 125 |
| $r_5$ [mm] | 130 |
| $r_6$ [mm] | 150 |
| $r_{out}$ [mm] | 170 |
| L [mm] | 100 |
| $\delta$ [deg] | 15 |
| $B_r$ [T] | 1.44 |

The parameters of the Halbach-array for the inner and outer rotor (described in Fig.2.2) resulted from optimization of the stall torque and are presented in Table 2.2. The optimization process did not require an advanced technique since with the proposed model, the stall torque can be obtained analytically for any Halbach-array arrangement in the two rotors with a low computational cost. It should be noted that the optimal arrangement of the outer rotor, in the performed case study, is the standard CMG since the angles $\beta_h$ and $\gamma_h$of the outer rotor are equal to zero.

**Table 2.2: Parameters of the HAL-CMG drive**

| | |
|---|---|
| **Inner Rotor** | |
| $\alpha_h$ [deg] | 20 |
| $\beta_h$ [deg] | 12.5 |
| $\gamma_h$ [deg] | 12.5 |
| $\psi$ [deg] | 60 |
| **Outer Rotor** | |
| $\alpha_h$ [deg] | 18 |
| $\beta_h$ [deg] | – |
| $\gamma_h$ [deg] | – |
| $\psi$ [deg] | – |

In Fig.2.5 the applied torque in the two rotors is presented for the two drives for the case of fixed inner rotor and rotating outer rotor.

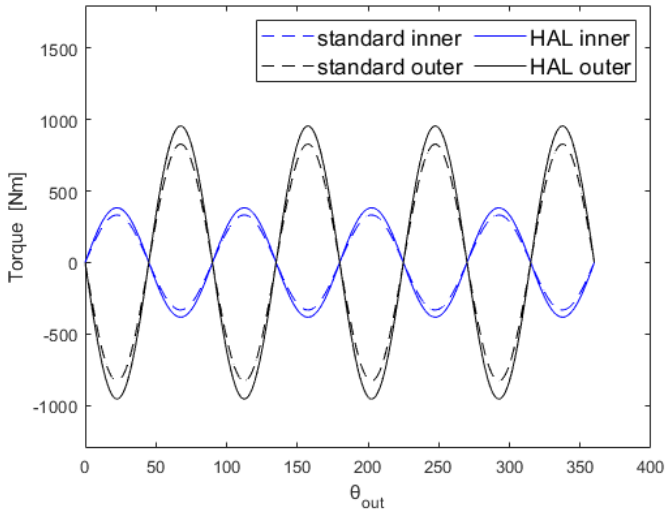


**Figure 2.5: Comparison of the torques applied on the inner and outer rotor in the standard and the HAL-CMG**

It can be observed that there is a significant improvement in the torque density with the use of HAL-CMG. More specifically, the stall torque of the HAL-CMG was 14.3% higher than the standard CMG's.

In Fig.2.6 the induced torques in the two rotors of the HAL-CMG where verified with FEA (ANSYS Maxwell). The adopted mesh type used in the FEA model is triangles with automatic meshing method that refines the mesh until convergence. A difference of 1-1.5% was observed between the analytical and FEA model, however, the analytical model was two orders of magnitude faster.

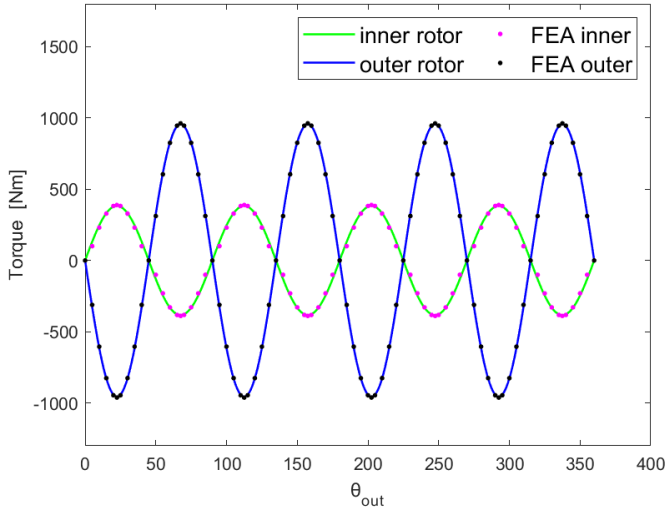


**Figure 2.6: Torque in the two rotors of the HAL-CMG as calculated from the analytical model and FEA**

Therefore, with the developed analytical model an accurate and fast calculation of torque in the two rotors of the HAL-CMG is achieved. Furthermore, with the developed model the torque ripple generated from the torque contributing harmonics

can be determined, a result that cannot immediately be obtained from FEA since only the resulting torque is calculated (sum of the contributing harmonics). In order to calculate the torque ripple from FEA it is necessary to perform a Fourier transform. The process would require additional computational time and several FEA simulations at different angles of rotation, while with the analytical model a single calculation is sufficient to determine the torque ripple.

The amplitudes of the torque-contributing harmonic terms of the two rotors for the standard and Halbach-array CMG are presented in Table 2.3.

**Table 2.3: Amplitude of contributing harmonics**

| Amplitude of inner rotor harmonic (Nm) | | | Amplitude of outer rotor harmonic (Nm) | | |
|---|---|---|---|---|---|
| | Standard CMG | HAL-CMG | | Standard CMG | HAL-CMG |
| $\xi_4$ | 333.81 | 381.89 | $\xi_{10}$ | 832.98 | 952.95 |
| $\xi_{12}$ | 1.25 | 1.09 | $\xi_{30}$ | 3.26 | 2.88 |
| $\xi_{20}$ | 0.02 | 0.001 | $\xi_{50}$ | 0.05 | 0.002 |

Due to the higher harmonics torque ripple is observed in both drives. The torque ripple of the HAL-CMG is 0.3% which is slightly lower than the torque ripple observed in the standard CMG drive. Therefore, with the use of HAL-CMG the stall torque is increased compared to the standard CMG drive without comprising the other operational characteristics.

## *Chapter 2-Conclusions*

In the present chapter a novel analytical 2D model was developed for the calculation of the magnetic potential of HAL-CMGs for every angle of rotation, geometry configuration and magnet parameters. The applied torque in the two rotors was calculated analytically from the Maxwell Stress Tensor. The induced torques in the two rotors of the HAL-CMG were verified with FEA. A case study was performed for a 4 pole pair inner rotor and a 10 pole pair outer rotor for a standard CMG and an optimised HAL-CMG with the same geometrical and constitutive parameters of the PMs. The stall torque of the HAL-CMG was improved by 14.3%. In addition, the torque ripple with the use of Halbach-arrays was slightly reduced compared to the standard CMG. Therefore, from the performed case study it can be observed that the HAL-CMG offers significant increase in torque density which is in accordance with other results in the literature. The developed model could be a valuable design tool for the optimization of HAL-CMGs since the applied torque in the two rotors can be calculated analytically thus reducing significantly the computational cost. Furthermore, the torque ripple of the HAL-CMG due to the torque contributing harmonics can be calculated analytically a result that cannot immediately be obtained from FEA since a Fourier transform is required that would increase the computational cost and FEA simulations.

## *Appendix A2.1*

The period of magnetization is:

$$T_0 = \frac{2\pi}{p} \tag{A2.1.1}$$

Therefore the magnetization vector of the HAL-CMG can be expressed as:

$$M_\theta(\theta) = \sum_{-\infty}^{+\infty} c_k e^{-i2\pi k f_0 \theta} \Rightarrow$$

$$M_\theta(\theta) = \sum_{k=1}^{\infty} d_k \cos(pk\theta) + e_k \sin(pk\theta) \tag{A2.1.2}$$

where:

$$d_k = 2\mathrm{Re}(c_k) \tag{A2.1.3}$$

$$e_k = -2\mathrm{Im}(c_k) \tag{A2.1.4}$$

If $k = 0$:

$$c_0 = \frac{p}{2\pi} \int_{T_0} M_\theta e^0 \, d\theta \Rightarrow c_0 = 0 \tag{A2.1.5}$$

If $k \neq 0$:

$$\begin{aligned} c_k = \frac{p}{2\pi} \Bigg[ & \int_{\alpha_h}^{\alpha_h+\beta_h} \frac{B_m \cos\psi}{\mu_0} e^{-ipk\theta} d\theta \\ & + \int_{\alpha_h+\beta_h}^{\alpha_h+\beta_h+\gamma_h} \frac{B_m}{\mu_0} e^{-ipk\theta} d\theta + \int_{\alpha_h+\beta_h+\gamma_h}^{\alpha_h+2\beta_h+\gamma_h} \frac{B_m \cos\psi}{\mu_0} e^{-ipk\theta} d\theta \\ & - \int_{2\alpha_h+2\beta_h+\gamma_h}^{2\alpha_h+3\beta_h+\gamma_h} \frac{B_m \cos\psi}{\mu_0} e^{-ipk\theta} d\theta - \int_{2\alpha_h+3\beta_h+\gamma_h}^{2\alpha_h+3\beta_h+2\gamma_h} \frac{B_m}{\mu_0} e^{-ipk\theta} d\theta \\ & - \int_{2\alpha_h+3\beta_h+2\gamma_h}^{2\alpha_h+4\beta_h+2\gamma_h} \frac{B_m \cos\psi}{\mu_0} e^{-ipk\theta} d\theta \Bigg] \end{aligned} \tag{A2.1.6}$$

From Euler identity:

$$c_k = \frac{B_m}{2\pi\mu_0 k}\Big[\cos\psi\Big(\sin\big(kp(\alpha_h+\beta_h)\big)-\sin(kp\alpha_h) + i\big(\cos\big(kp(\alpha_h+\beta_h)\big)-\cos(kp\alpha_h)\big)\Big)+\sin\big(kp(\alpha_h+\beta_h+\gamma_h)\big) - \sin\big(kp(\alpha_h+\beta_h)\big) + i\big(\cos\big(kp(\alpha_h+\beta_h+\gamma_h)\big)-\cos\big(kp(\alpha_h+\beta_h)\big)\big) + \cos\psi\Big(\sin\big(kp(\alpha_h+2\beta_h+\gamma_h)\big)-\sin\big(kp(\alpha_h+\beta_h+\gamma_h)\big) + i\big(\cos\big(kp(\alpha_h+2\beta_h+\gamma_h)\big)-\cos\big(kp(\alpha_h+\beta_h+\gamma_h)\big)\big)\Big) - \cos\psi\Big(\sin\big(kp(2\alpha_h+3\beta_h+\gamma_h)\big)-\sin\big(kp(2\alpha_h+2\beta_h+\gamma_h)\big) + i\big(\cos\big(kp(2\alpha_h+3\beta_h+\gamma_h)\big)-\cos\big(kp(2\alpha_h+2\beta_h+\gamma_h)\big)\big)\Big) - \sin\big(kp(2\alpha_h+3\beta_h+2\gamma_h)\big)-\sin\big(kp(2\alpha_h+3\beta_h+\gamma_h)\big) + i\big(\cos\big(kp(2\alpha_h+3\beta_h+2\gamma_h)\big)-\cos\big(kp(2\alpha_h+3\beta_h+\gamma_h)\big)\big) - \cos\psi\Big(\sin\big(kp(2\alpha_h+4\beta_h+2\gamma_h)\big)-\sin\big(kp(2\alpha_h+3\beta_h+2\gamma_h)\big) + i\big(\cos\big(kp(2\alpha_h+4\beta_h+2\gamma_h)\big) - \cos\big(kp(2\alpha_h+3\beta_h+2\gamma_h)\big)\big)\Big)\Big] \quad \text{(A2.1.7)}$$

Therefore, $d_k$ and $e_k$ are:

$$d_k = 2\mathrm{Re}(c_k) = \frac{B_m}{\pi\mu_0 k}\Big[\cos\psi\big(\sin\big(kp(\alpha_h+\beta_h)\big)-\sin(kp\alpha_h)\big) + \sin\big(kp(\alpha_h+\beta_h+\gamma_h)\big)-\sin\big(kp(\alpha_h+\beta_h)\big) + \cos\psi\big(\sin\big(kp(\alpha_h+2\beta_h+\gamma_h)\big)-\sin\big(kp(\alpha_h+\beta_h+\gamma_h)\big)\big) - \cos\psi\big(\sin\big(kp(2\alpha_h+3\beta_h+\gamma_h)\big)-\sin\big(kp(2\alpha_h+2\beta_h+\gamma_h)\big)\big) - \sin\big(kp(2\alpha_h+3\beta_h+2\gamma_h)\big)-\sin\big(kp(2\alpha_h+3\beta_h+\gamma_h)\big) - \cos\psi\big(\sin\big(kp(2\alpha_h+4\beta_h+2\gamma_h)\big) - \sin\big(kp(2\alpha_h+3\beta_h+2\gamma_h)\big)\big)\Big] \quad \text{(A2.1.8)}$$

$$e_k = -2\mathrm{Im}(c_k)$$
$$= -\frac{B_m}{\pi\mu_0 k}\left[\cos\psi\left(\cos\left(kp(\alpha_h+\beta_h)\right)-\cos(kp\alpha_h)\right)\right.$$
$$+\cos\left(kp(\alpha_h+\beta_h+\gamma_h)\right)-\cos\left(kp(\alpha_h+\beta_h)\right)$$
$$+\cos\psi\left(\cos\left(kp(\alpha_h+2\beta_h+\gamma_h)\right)-\cos\left(kp(\alpha_h+\beta_h+\gamma_h)\right)\right)$$
$$-\cos\psi\left(\cos\left(kp(2\alpha_h+3\beta_h+\gamma_h)\right)-\cos\left(kp(2\alpha_h+2\beta_h+\gamma_h)\right)\right)$$
$$-\cos\left(kp(2\alpha_h+3\beta_h+2\gamma_h)\right)-\cos\left(kp(2\alpha_h+3\beta_h+\gamma_h)\right)$$
$$-\cos\psi\left(\cos\left(kp(2\alpha_h+4\beta_h+2\gamma_h)\right)\right.$$
$$\left.\left.-\cos\left(kp(2\alpha_h+3\beta_h+2\gamma_h)\right)\right)\right] \qquad \text{(A2.1.9)}$$

Similarly, $M_r$ can be written as:

$$M_r(\theta) = \sum_{k=1}^{\infty} a_k\cos(pk\theta) + b_k\sin(pk\theta) \qquad \text{(A2.1.10)}$$

Where $\alpha_k$ and $b_k$ can be calculated similarly:

$$a_k = 2\mathrm{Re}(c_k) = \frac{B_m}{\pi\mu_0 k}\left[-\sin(kp\alpha_h)-\sin\psi\left(\sin\left(kp(\alpha_h+\beta_h)\right)-\sin(kp\alpha_h)\right)\right.$$
$$+\sin\psi\left(\sin\left(kp(\alpha_h+2\beta_h+\gamma_h)\right)-\sin\left(kp(\alpha_h+\beta_h+\gamma_h)\right)\right)$$
$$+\sin\left(kp(2\alpha_h+2\beta_h+\gamma_h)\right)-\sin\left(kp(\alpha_h+2\beta_h+\gamma_h)\right)$$
$$+\sin\psi\left(\sin\left(kp(2\alpha_h+3\beta_h+\gamma_h)\right)-\sin\left(kp(2\alpha_h+2\beta_h+\gamma_h)\right)\right)$$
$$-\sin\psi\left(\sin\left(kp(2\alpha_h+4\beta_h+2\gamma_h)\right)\right.$$
$$\left.\left.-\sin\left(kp(2\alpha_h+3\beta_h+2\gamma_h)\right)\right)\right] \qquad \text{(A2.1.11)}$$

$$b_k = -2\mathrm{Im}(c_k)$$
$$= -\frac{B_m}{\pi\mu_0 k}\left[-\cos(kp\alpha_h)-\cos(0)\right.$$
$$-\sin\psi\left(\cos\left(kp(\alpha_h+\beta_h)\right)-\cos(kp\alpha_h)\right)$$
$$+\sin\psi\left(\cos\left(kp(\alpha_h+2\beta_h+\gamma_h)\right)-\cos\left(kp(\alpha_h+\beta_h+\gamma_h)\right)\right)$$
$$+\cos\left(kp(2\alpha_h+2\beta_h+\gamma_h)\right)-\cos\left(kp(\alpha_h+2\beta_h+\gamma_h)\right)$$
$$+\sin\psi\left(\cos\left(kp(2\alpha_h+3\beta_h+\gamma_h)\right)-\cos\left(kp(2\alpha_h+2\beta_h+\gamma_h)\right)\right)$$
$$-\sin\psi\left(\cos\left(kp(2\alpha_h+4\beta_h+2\gamma_h)\right)\right.$$
$$\left.\left.-\cos\left(kp(2\alpha_h+3\beta_h+2\gamma_h)\right)\right)\right] \qquad \text{(A2.1.12)}$$

In case of an initial phase angle $\theta_0$ of the inner rotor, the Fourier Series can be written as:

$$M_r(\theta) = \sum_{k=1}^{\infty} a_k\cos\left(pk(\theta-\theta_0)\right) + b_k\sin\left(pk(\theta-\theta_0)\right) \qquad \text{(A2.1.13)}$$

$$M_\theta(\theta) = \sum_{k=1}^{\infty} d_k\cos\left(pk(\theta-\theta_0)\right) + e_k\sin\left(pk(\theta-\theta_0)\right) \qquad \text{(A2.1.14)}$$

## *Chapter 2-References*

[2.1] Baninajar, H., Modaresahmadi, S., Wong, H. Y., Bird, J., Williams, W., & Dechant, B. (2022). Designing a Halbach rotor magnetic gear for a marine hydrokinetic generator. IEEE Transactions on Industry Applications, 58(5), 6069-6080.

[2.2] L. Jian, K.T. Chau, A coaxial magnetic gear with Halbach permanent-magnet arrays, IEEE Trans. Energy Convers. 25 (2) (2010) 319–328.

[2.3] Wong, H. Y., Bird, J. Z., Barnett, D., & Williams, W. (2019, May). A high torque density Halbach rotor coaxial magnetic gear. In 2019 IEEE International Electric Machines & Drives Conference (IEMDC) (pp. 233-239). IEEE.

[2.4] Z. A. Cameron, T. Tallerico, and J. Scheidler, "Lessons learned in fabrication of a high-specific-torque concentric magnetic gear," in Proc. 5th Annu. Forum Techn. Display Vertical Flight Soc., 2019.

[2.5] Jiang, Y., Deng, Y., Zhu, P., Yang, M., & Zhou, F. (2021). Optimization on size of Halbach array permanent magnets for magnetic levitation system for permanent magnet Maglev train. IEEE Access, 9, 44989-45000.

[2.6] Hilton, J. E., & McMurry, S. M. (2012). An adjustable linear Halbach array. Journal of Magnetism and Magnetic Materials, 324(13), 2051-2056.

[2.7] Jing, L., Su, Z., Wang, T., Wang, Y., & Qu, R. (2023). Multi-objective optimization analysis of magnetic gear with HTS bulks and uneven Halbach arrays. IEEE Transactions on Applied Superconductivity.

[2.8] Z. Q. Zhu and D. Howe, "Halbach permanent magnet machines and applications: a review," Inst. Electr. Eng. Proc. Electr. Power Appl., vol. 148, no. 4, pp. 299–308, Jul. 2001.

[2.9] Jing, L., Liu, W., Tang, W., & Qu, R. (2023). Design and optimization of coaxial magnetic gear with double-layer PMs and spoke structure for tidal power generation. IEEE/ASME Transactions on Mechatronics.

[2.10] Aloeyi, E. F., Shoaei, A., & Wang, Q. (2023, August). A hybrid coaxial magnetic gear using flux-focusing halbach permanent magnet arrangement. In 2023 IEEE 14th International Conference on Power Electronics and Drive Systems (PEDS) (pp. 1-6). IEEE.

# 3 Dynamical response in coaxial magnetic gears

During acceleration, slippage phenomena could occur due to absence of contact between the two rotors of the magnetic gears. The dynamical phenomena during transient operation should be investigated in order to determine the transmission error [3.1]-[3.3]. The dynamical equations in coaxial magnetic gears consist of a system of two non-linear differential equations [3.4] that cannot be solved analytically. As a consequence, iterative methods are used in order to determine the dynamical response of the system that could increase the computational cost in an optimization processes. When acceleration and applied torque are small the system will converge to a solution depending on the equivalent gear ratio. However, when the values of acceleration and applied torque are high the system will diverge and the dynamical behaviour will not be depending on the gear ratio of the magnetic gear. A process that could determine the maximum operational characteristics (acceleration and torque) without the requirement for a numerical solution of the system of equations would be beneficial to researchers and the industry.

In the present work, an analytical non-dimensional condition will be derived that can determine the convergence/divergence of the system under constant acceleration and applied torque. A set of case studies will be performed with arbitrary inputs of inner rotor acceleration and applied torque in the outer rotor. A prediction on convergence/divergence of the system will be made from the developed non-dimensional condition. The dynamical equation of the outer rotor will be solved numerically in order to verify the prediction of the model. Finally, since in most applications it would be useful to restrict the transmission error to a certain value the derived non-dimensional condition could be modified in order to calculate the maximum operational characteristics that yield the allowed transmission error. A case study was performed where for a given acceleration of the inner rotor the maximum applied torque on the outer rotor was calculated so that the transmission error of the system did not exceed a certain value.

Furthermore, the case of acceleration with ripple has been investigated. It was demonstrated that during acceleration with ripple under constant applied outer load, the system showcases a chaotic behaviour similar to the driven pendulum [3.5]-[3.6]. A case study for the dynamical operation of coaxial magnetic gears under constant applied outer load and acceleration with ripple was performed. Specifically, a thorough analysis on the frequency of the ripple has been conducted. It was observed that when the ripple frequency was slightly lower than the frequency of the oscillation under steady acceleration, the system could potentially diverge even if the acceleration of the system was lower than the critical value. Furthermore, it was shown that a smaller acceleration with a given ripple frequency could lead to divergence while a higher acceleration with the same ripple frequency could not, a phenomenon that emphasizes the significance of the frequency ratio. Finally, it was observed that the system could appear to have a periodic-like behaviour for a considerable time of operation before it diverges which showcases the chaotic behaviour of the system.

With the present work, a detailed non-dimensional model has been derived that could be a useful tool for determining the stability of coaxial magnetic gears without the requirement of numerical solution of the governing equations. In addition, some

interesting observations are made regarding the chaotic behaviour of the dynamical response of coaxial magnetic gears during acceleration with ripple.

## *3.1 Non-dimensionalization of the governing ODEs*

In coaxial magnetic gears the system of the dynamical equations of the inner and outer rotor has the following form [3.2]-[3.4]:

$$I_{in}\ddot{\theta}_{in} + \sum_{k=1}^{\infty} \xi_{(2k-1)p_{in},in} \sin[(2k-1)p_{in}\theta_{in} + (2k-1)p_{out}\theta_{out}] = T_{in} \quad (3.1)$$

$$I_{out}\ddot{\theta}_{out} + \sum_{k=1}^{\infty} \xi_{(2k-1)p_{out},out} \sin[(2k-1)p_{in}\theta_{in} + (2k-1)p_{out}\theta_{out}] = T_{out} \quad (3.2)$$

where $(\xi_{(2k-1)p_{in},in})$ and $(\xi_{(2k-1)p_{out},out})$ are the amplitudes of the torque-contributing harmonics that can be calculated analytically for a given configuration of a coaxial magnetic gear [3.4], while $(T_{in})$ and $(T_{out})$ are the applied torques in the inner and outer rotor respectively. Neglecting the higher order harmonics (torque ripple) that have considerably lower amplitude (lower than 1%) [10], Eq.(3.1)-(3.2) take the following form:

$$I_{in}\ddot{\theta}_{in} + \frac{Mp_{in}}{p_{out}} \sin(p_{in}\theta_{in} + p_{out}\theta_{out}) = T_{in} \quad (3.3)$$

$$I_{out}\ddot{\theta}_{out} + M\sin(p_{in}\theta_{in} + p_{out}\theta_{out}) = T_{out} \quad (3.4)$$

where $(M)$ is the stall torque (first contributing harmonic) of the outer rotor [3.4], [3.7].

In general, magnetic gears are prone to slippage during acceleration. Therefore, without loss of generality, we will investigate the response of the outer rotor under acceleration $a$ of the inner rotor. As a result, Eq.(3.4) could be written in the following form:

$$I_{out}\ddot{\theta}_{out} + M\sin[\frac{1}{2}p_{in}at^2 + p_{out}\theta_{out}] = T_{out} \quad (3.5)$$

Eq.(3.5) is a non-linear differential equation that describes the dynamical response of the outer rotor of the magnetic gear, under constant applied torque and acceleration in the inner rotor. Eq.(3.5) cannot be solved analytically and its solution can only be determined numerically. However, it would be useful to know whether the solution will converge or if it will diverge without the requirement for numerical calculation of the solution of the system.

The transmission error of the system $(x)$ is defined by equation (3.6.A).

$$x = \frac{1}{2}p_{in}at^2 + p_{out}\theta_{out} \quad (3.6.A)$$

As a consequence, it yields that:

$$\ddot{\theta}_{out} = \frac{\ddot{x}}{p_{out}} - \frac{p_{in}a}{p_{out}} \tag{3.6.B}$$

and therefore Eq.(3.7) is derived:

$$\frac{I_{out}}{p_{out}}\ddot{x} + M\sin x = T_{out} + \frac{p_{in}I_{out}a}{p_{out}} \tag{3.7}$$

As a consequence, Eq.(3.7) could be written in the following form:

$$\ddot{x} + \omega_0^2 \sin x = \omega_0^2(\tau + \gamma) \tag{3.8}$$

where (τ) and (γ) are non-dimensional constants defined as:

$$\tau = \frac{p_{in}I_{out}a}{p_{out}M} \tag{3.9.A}$$

$$\gamma = \frac{T_{out}}{M} \tag{3.9.B}$$

and

$$\omega_0^2 = \frac{Mp_{out}}{I_{out}} \tag{3.9.C}$$

By multiplying Eq.(3.8) with $(\dot{x})$ and differentiating with respect to time we obtain:

$$\frac{d}{dt}\left(\frac{1}{2}\dot{x}^2 - \omega_0^2 \cos x\right) = \frac{d}{dt}(\omega_0^2(\tau + \gamma)\, x + c) \tag{3.10}$$

In general, the initial condition of the system for t=0 could be the case where the outer load $(T_{out})$ is applied and the coaxial magnetic gear operates under constant conditions without any kind of oscillations or ripple. As a result, the initial conditions for the transmission error (x) are: $x(0) = \sin^{-1}\left(\frac{T_{out}}{M}\right) = \sin^{-1}\gamma$ and $\dot{x}(0) = 0$.
Therefore, applying the initial conditions to Eq.(3.10) we obtain:

$$\frac{1}{2}\dot{x}^2 - \omega_0^2 \cos x = \omega_0^2(\tau + \gamma)\, x - \omega_0^2 \cos(\sin^{-1}\gamma) - \omega_0^2(\tau + \gamma)\sin^{-1}\gamma \tag{3.11}$$

It would be useful to investigate the stability of Eq.(3.11) when the acceleration $(a)$ (and consequently the non-dimensional constant (τ)) is applied. For every different initial condition $x(0)$ a different maximum acceleration can be applied to the system. If the acceleration exceeds the critical value, the system will diverge and the transmission error (x) will tend to infinity.

The fixed points of the system can be obtained from the solution of Eq.(3.5) for $\ddot{x} = 0$:

$$x' = \sin^{-1}(\tau + \gamma) \tag{3.12.A}$$

$$x^* = \pi - \sin^{-1}(\tau + \gamma) \tag{3.12.B}$$

The fixed point $(x^*)$, is the critical point for the stability of the system. If the transmission error exceeds $(x^*)$ then the system will diverge. Therefore, a criterion could be formed [3.8] for the stability of the system as follows, since $\dot{x}^2 \geq 0$:

$$\cos x^* + (\tau + \gamma)\, x^* - \cos(\sin^{-1}\gamma) - (\tau + \gamma)\sin^{-1}\gamma \geq 0 \qquad (3.13)$$

By applying different initial conditions, the maximum acceleration $(a)$ and as a consequence the maximum non-dimensional constant $(\tau)$ can be calculated numerically from Eq.(3.13). In Fig.3.1 the maximum non-dimensional constant $(\tau)$ and the maximum sum of $(\gamma + \tau)$ is presented with respect to $(\gamma)$.

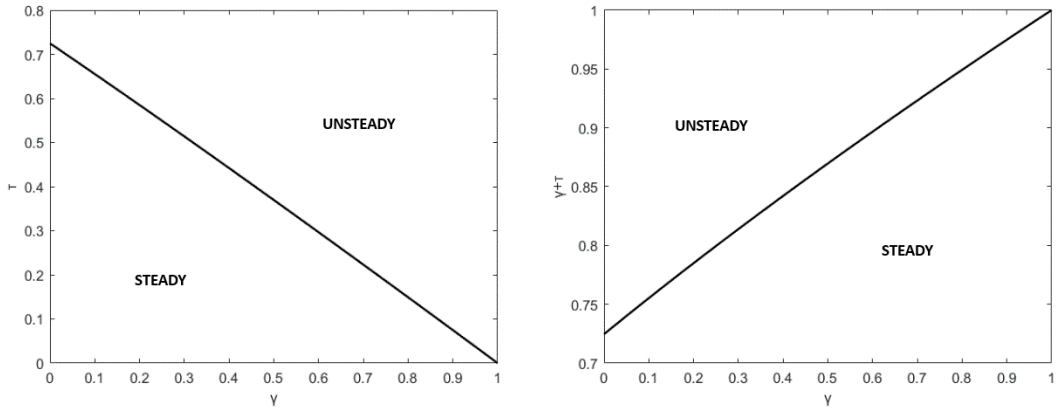


**Figure 3.1: Maximum non-dimensional acceleration (τ) as a function of the initial non-dimensional applied load (γ).**

It can be observed, that as expected when the outer applied load $(T_{out})$ is increased the maximum acceleration that can be induced to the system is reduced. In addition, in the limit case where the applied load $(T_{out})$ is equal to the stall torque $(M)$ and thus $\gamma = 1$, no acceleration can be applied to system. However, the maximum sum of $(\gamma + \tau)$ is increases as the outer applied load $(T_{out})$ is increased. Therefore, from Eq.(3.11) and Fig.2 the stability of the system can be determined for any given non-dimensional constant $(\gamma)$ and $(\tau)$.

In general, however the sum of $(\gamma + \tau)$ will be lower than the critical case derived from Eq.(3.11). In that case, the system will oscillate between the initial condition $x(0)$ and maximum transmission error value $(x_{max})$ that can be calculated from Eq.(3.11) by applying the values of $(\gamma)$ and $(\tau)$ and letting $\dot{x} = 0$. The equation could then be solved numerically in order to calculate the $(x_{max})$ value.

When the system oscillates between the $x(0)$ and $(x_{max})$ the period of the system could be determined from Eq.(3.11) as follows:

$$\frac{dx}{dt} = \sqrt{2}\omega_0\sqrt{\cos x + (\tau + \gamma)\, x - \cos(\sin^{-1}\gamma) - (\tau + \gamma)\sin^{-1}\gamma} \qquad (3.14.A)$$

Eq.(3.14.A) could be written to the following form:

$$dt = \frac{dx}{\sqrt{2}\omega_0\sqrt{\cos x + (\tau+\gamma)\,x - \cos(\sin^{-1}\gamma) - (\tau+\gamma)\sin^{-1}\gamma}} \tag{3.14.B}$$

Integrating Eq.(3.14.B) from $x(0)$ and $(x_{max})$ which is equal to half of the period $(T_0)$, we can obtain the period of the oscillation from Eq.(3.15)

$$T_0 = \frac{\sqrt{2}}{\omega_0}\int_{x(0)}^{x_{max}} \frac{dx}{\sqrt{\cos x + (\tau+\gamma)\,x - \cos(\sin^{-1}\gamma) - (\tau+\gamma)\sin^{-1}\gamma}} \tag{3.15}$$

The integral of Eq.(3.15) can only be solved numerically. The frequency of the oscillation can be obtained from $f_0 = {}^{1}/_{T_0}$.

When the amplitude of the oscillation is increased $(x_{max} - x(0))$ the period of the system is increased and as a consequence the frequency $(f_0)$ is decreased.

The minimum period of the oscillation is obtained when no external load is applied $(\gamma = 0)$ and a very small acceleration is applied to the system $(\tau \to 0)$. The period calculation for this case is shown in Appendix A3.1.

## *3.2 Modelling for acceleration with ripple and chaotic behaviour*

It is common for power transmission systems to exhibit ripple during acceleration. We will investigate the case where the acceleration is of the following form:

$$a(t) = a\big(1 + \varepsilon\sin(2\pi f t)\big) \tag{3.16}$$

where $(a)$ is the nominal acceleration, $(\varepsilon)$ is the ripple of the acceleration (as a percentage) and $(f)$ is the frequency of the ripple. A similar to Eq.(3.8) non-dimensional form can be obtained:

$$\ddot{x} + \omega_0^2 \sin x = \omega_0^2(\tau+\gamma) + \omega_0^2\varepsilon\tau\sin(2\pi f t) \tag{3.17}$$

Eq.(3.17) has a similar form to the driven pendulum that exhibits chaotic behaviour [3.5], [3.6] and could be written in the following form as a system of a three-dimensional first order ordinary differential equations:

$$\dot{v} = -\omega_0^2\sin x + \omega_0^2(\tau+\gamma) + \omega_0^2\varepsilon\tau\sin\varphi \tag{3.18.A}$$
$$\dot{x} = v \tag{3.18.B}$$
$$\dot{\varphi} = 2\pi f \tag{3.18.C}$$

The system of Eq.(3.18.A)-(3.18.C) could exhibit chaotic behaviour. It is interesting to investigate the behaviour of the system for various frequencies of the acceleration ripple $(f)$, especially for the case when the frequency of the ripple is near the frequency of the oscillation of the system $(f_0)$ under steady acceleration as calculated from Eq.(3.15).

### *3.3.1 Verification of the stability criterion and discussion*

In order to validate the developed model a case study was performed with the parameters presented in Table 3.1, while the permanent magnets used are Nd-Fe. The stall torque can be obtained following the methodology described in [3.4]. In addition, the torque ripple was also calculated and equal to 0.49 Nm which is lower than 0.2% of the stall torque and therefore the assumption of neglecting the torque ripple is justified.

**Table 3.1: Geometrical parameters**

| | |
|---|---|
| $p_{in}$ | 8 |
| $p_{out}$ | 32 |
| $r_1$ [mm] | 80 |
| $r_2$ [mm] | 100 |
| $r_3$ [mm] | 105 |
| $r_4$ [mm] | 125 |
| $r_5$ [mm] | 130 |
| $r_6$ [mm] | 150 |
| $r_{out}$ [mm] | 170 |
| δ [deg] | 5 |
| L[mm] | 100 |
| M [Nm] | 270 |
| $I_{out}$ [kgm$^2$] | 0.64748 |

The following two cases presented in Table 3.2 were considered in order to demonstrate the validity of the developed criterion. The critical value for convergence is $\tau + \gamma \leq 0.724611$

**Table 3.2: Performed case studies-results**

| | $a[\frac{rad}{s^2}]$ | $T_{out}$[Nm] | $\tau + \gamma$ | Theoretical prediction | Simulation result |
|---|---|---|---|---|---|
| Case 1 | 1208.64 | 0 | 0.724610 | Converges | Converges |
| Case 2 | 1208.66 | 0 | 0.724612 | Diverges | Diverges |

The transmission error for the two is presented in Fig.3.2 by solving numerically Eq.(8) in Simulink. For the numerical solution of the Eq.(3.8) a time step of $\Delta t = 10^{-7}$s is used.

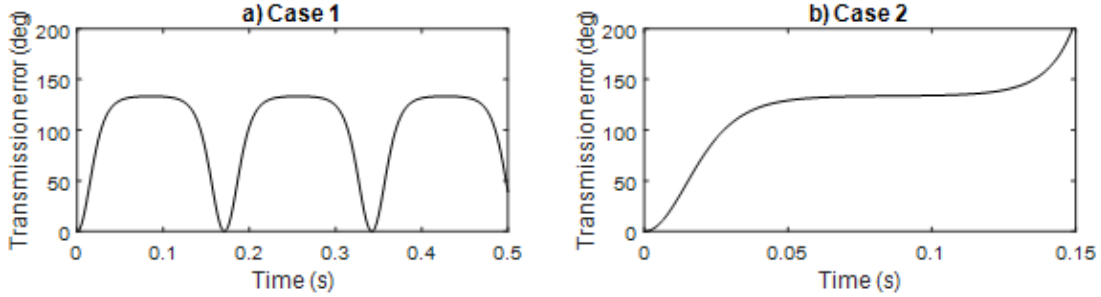


**Figure 3.2: Transmission error in cases 1-2 of Table 3.2.**

In Fig.3.2a and Fig.3.2b the transmission error for Case 1 and Case 2 is presented. The two cases represent a system of an accelerating inner rotor without an applied torque in the outer rotor. In Case 1 the acceleration is lower than the critical value and therefore the system will converge depending on the gear ratio. A transmission error with an oscillatory behaviour of a constant amplitude will be present in the response of the outer rotor. However, when the acceleration is higher than the critical value the system will diverge as shown in Case 2.

Finally, the maximum operational characteristics that yield a transmission error within a certain limit can be calculated. The maximum operational characteristics could be easily obtained from Eq.(3.11) where $(\mathrm{x})$ will take the value of the transmission error limit. For the parameters of the case study if the transmission error should be confided at $\mathrm{x} = 10°$ then the stability equation yields: $\tau + \gamma \leq 0.08704$.

If no outer load is applied then the maximum acceleration that can be induced in the inner rotor without the transmission error exceeding $10°$ is: $\mathrm{a} = 145.18\ \mathrm{rad/s^2}$.

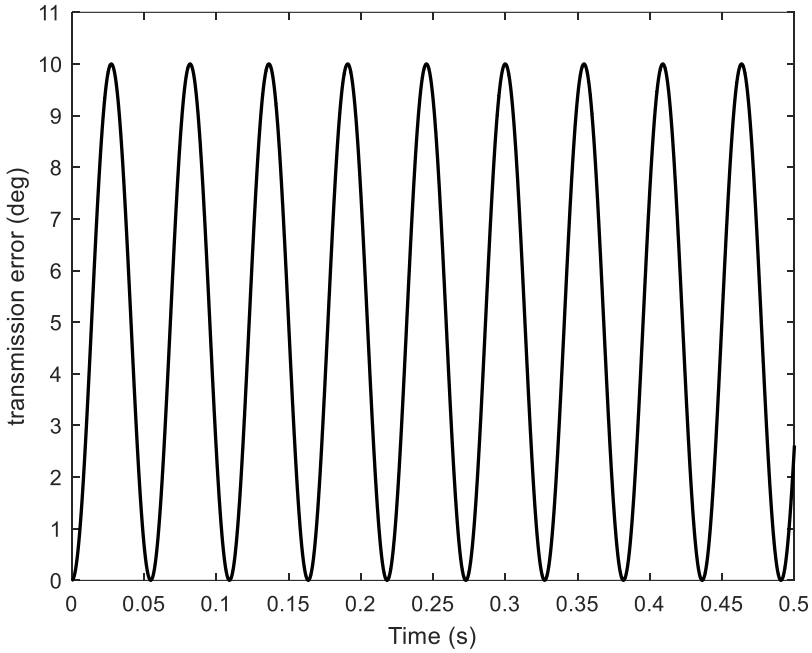


**Figure 3.3: Transmission error for $\mathbf{T_{out} = 0\ Nm}$ and $\mathbf{a = 145.18\ rad/s^2}$.**

In Fig.3.3 the transmission error for $\mathrm{T_{out}} = 0\ \mathrm{Nm}$ and $\mathrm{a} = 145.18\ \mathrm{rad/s^2}$ is presented. It can be observed that the transmission error does not exceed $10$ degrees.

### *3.3.2 Chaotic behaviour and discussion*

A different case study presented in Table 3.3 is considered to showcase the chaotic behaviour during acceleration with ripple.

**Table 3.3: Geometrical parameters**

| | |
|---|---|
| $p_{in}$ | $4$ |
| $p_{out}$ | $10$ |
| $r_1$ [mm] | 28 |
| $r_2$ [mm] | 33 |
| $r_3$ [mm] | 37.5 |
| $r_4$ [mm] | 47.5 |
| $r_5$ [mm] | 51 |
| $r_6$ [mm] | 56 |
| $r_{out}$ [mm] | 70 |
| δ [deg] | 15 |
| L[mm] | 100 |
| M [Nm] | $40$ |
| $I_{out}$ [$kgm^2$] | $0.020316$ |

Furthermore, the following non-dimensional parameters presented in Table 3.4 are considered. The maximum non-dimensional acceleration that can be applied to the system is equal to $\tau = 0.3696$ (when ε=0) as calculated from Eq.(10). For the numerical solution of the Eq.(3.8) and Eq. (3.17) a time step of $\Delta t = 10^{-7}$s is used.

**Table 3.4: Case study parameters**

| | |
|---|---|
| γ | $0.5$ |
| τ | $0.34$ |
| ε | 0.01 |

In Fig.3.4 the transmission error $(x)$ with respect to time is presented for the case of steady acceleration (ε=0).

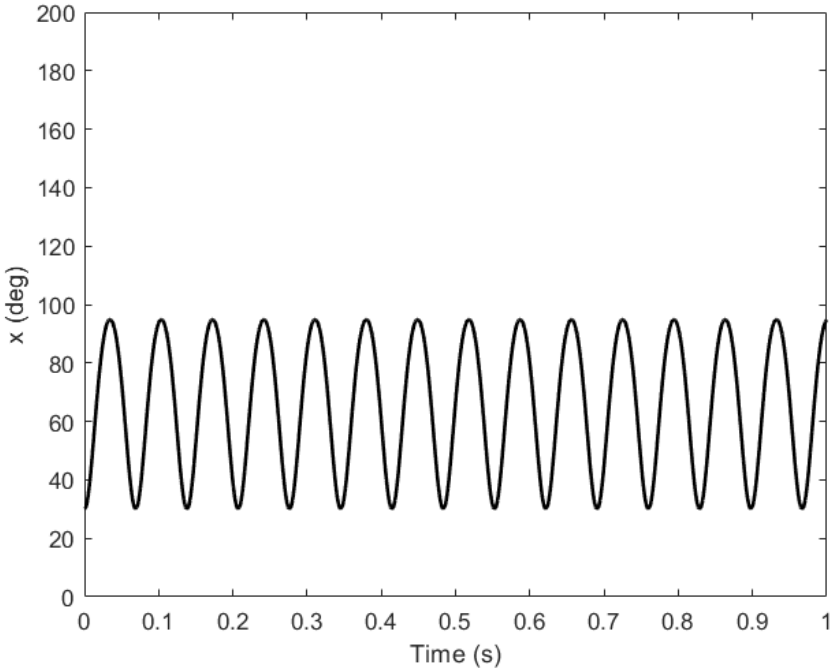


**Figure 3.4: Transmission error for steady acceleration (ε=0).**

In Fig. 3.5 the phase diagram of the oscillation is presented.

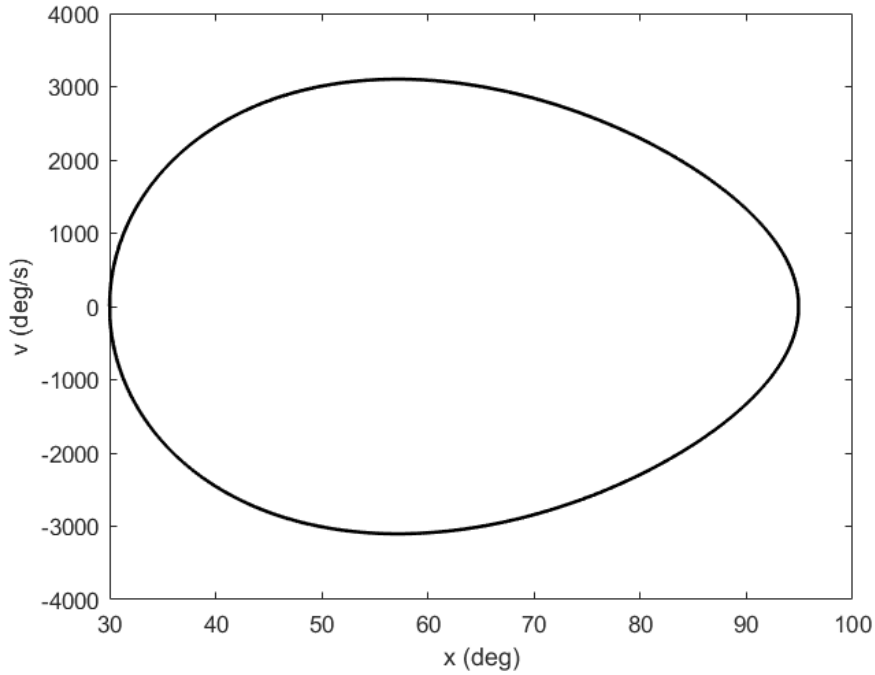


**Figure 3.5: Phase diagram for steady acceleration (ε=0).**

The frequency of the oscillation can be obtained from Eq.(3.15) and is equal to $f_0 = 14.48$ Hz.

The acceleration ripple is applied and the maximum transmission error is determined for different frequencies of the acceleration ripple. In Fig.3.6 for reasons of clarity,

when the system diverges the transmission error value is bounded to 200 degrees in order to showcase the trend of the phenomenon.

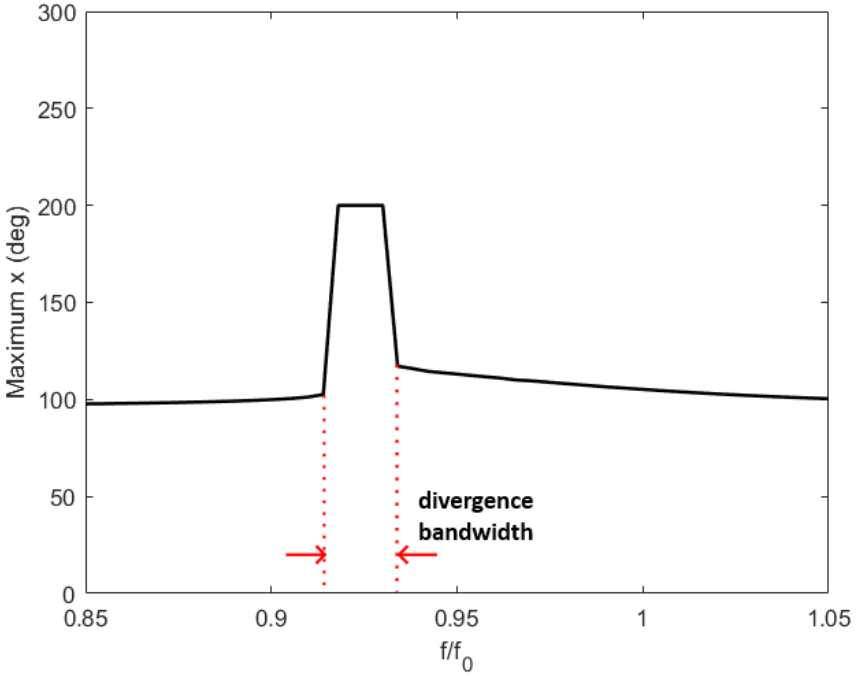


**Figure 3.6: Maximum transmission error for different acceleration ripple frequencies.**

It can be observed that the system will diverge when the ratio is between approximately 0.915 and 0.930 despite the fact that the sum of $(\gamma + \tau + \varepsilon)$ is lower than the critical value as calculated from Eq. (3.11). In addition, it can be observed that when the frequency of the ripple is equal to $(f_0)$ the system does not tend to increase the maximum value of the transmission error $(x)$ significantly. This phenomenon can be explained due to the fact that when the system increases its maximum value of $(x)$ then the period of the system will change according to Eq. (3.15). Specifically, the period of the system will increase as we approach higher values of $(x)$ and as a result the frequency of the oscillation of $(x)$ will decrease. Therefore, even though the ratio is initially equal to 1, the frequency of $(x)$ $(f_0)$ will soon be decreased and the system will stop being in phase and therefore the oscillation of $(x)$ will be limited to certain maximum.

However, when the acceleration ripple frequency $(f)$ is slightly lower than the initial frequency $(f_0)$ the system will gradually increase the maximum value of $(x)$ thus leading to larger period of oscillations and consequently lower $(f_0)$. Therefore, as the time progresses the frequency $(f_0)$ will tend towards the frequency of the acceleration ripple $(f)$ and could potentially lead to the divergence of the system due to resonance.

In general the sum of $(\gamma + \tau)$ should be close to the critical value so that the system will diverge under acceleration ripple $(f)$. This is attributed to the fact that the frequency of the oscillation of $(x)$, $(f_0)$, changes as the amplitude of the oscillation increases. Thus, it is difficult to have a resonant frequency for the entire oscillation of $(x)$ phenomenon when the initial sum of $(\gamma + \tau)$ is not close to the critical value.

In Fig. 3.7 the Poincare sections for different $f/f_0$ cases are presented. The sections are obtained after a simulation time of 30s. Each point at the Poincare sections is obtained depending on the frequency of the acceleration ripple. Therefore, each point is obtained every $1/f$ seconds. It is interesting to notice the behaviour of the section when the value $f/f_0$ is lower than 1 and near the divergence bandwidth.

From Fig. 3.7 the different behaviour of the system with respect to the ratio $f/f_0$ is presented. When the value of the ratio $f/f_0$ is not close to the divergence bandwidth (i.e. $f/f_0$ =1.07 and $f/f_0$ =0.90 case) the Poincare sections appear to be similar to the phase diagram of steady acceleration case presented in Fig.3.5 which implies that the ripple of the acceleration does not affect significantly the dynamical response of the system. However, when the ratio $f/f_0$ approaches the divergence bandwidth the Poincare sections showcase a significant alteration from the phase diagram presented in Fig.3.5.

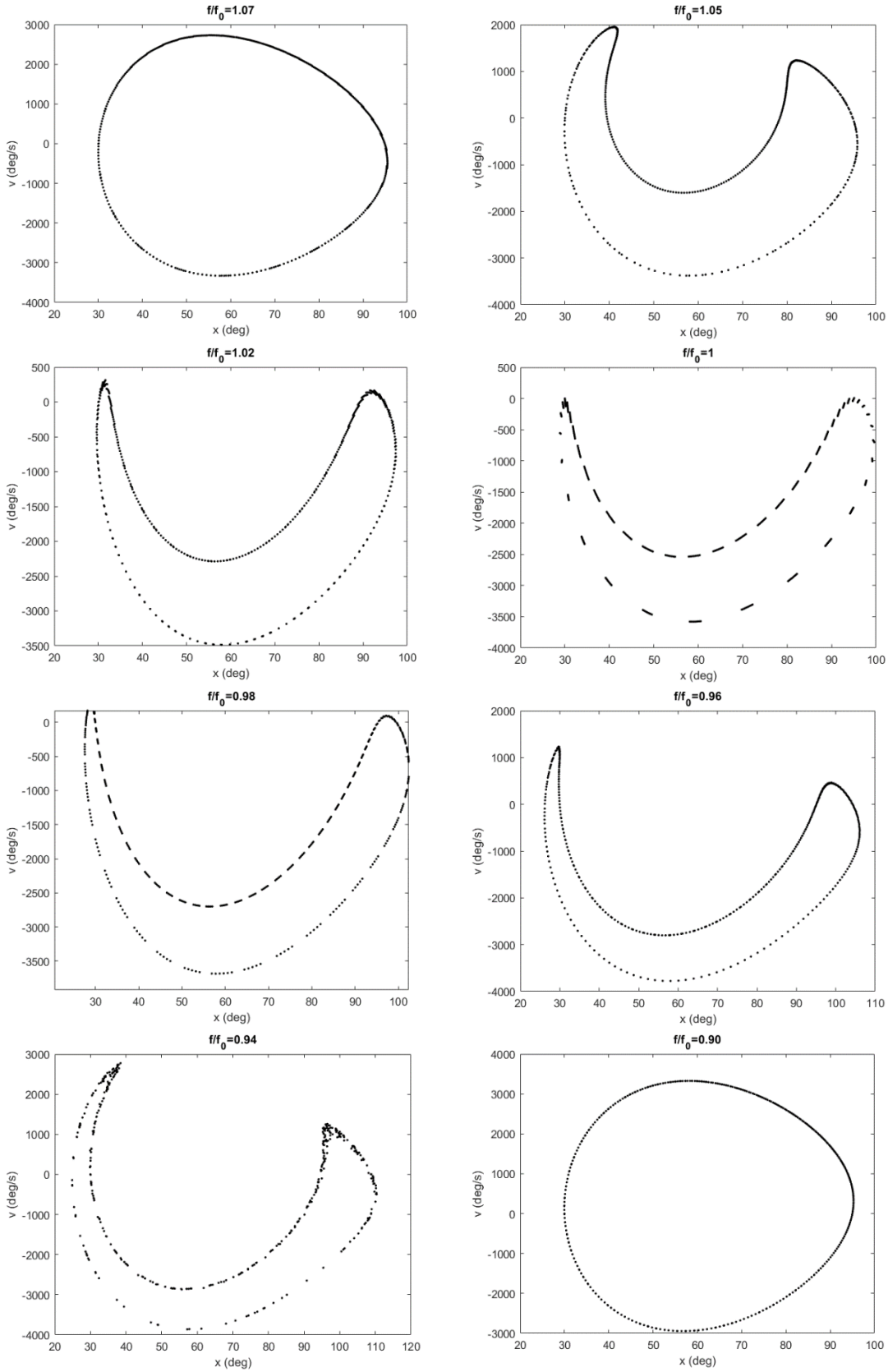


**Figure 3.7: Poincare sections for different acceleration ripple frequencies**

In Fig.3.8 the transmission error with respect to time is presented for two cases where the system will diverge. It is interesting to notice that the divergence could occur after

a significant number of oscillations as shown in the $f/f_0$=0.93 case. The system initially appears to have a periodical behaviour when suddenly diverges. Even, though an acceleration that exceeds 20 seconds is not expected during the operation of the coaxial magnetic gear it is interesting to showcase such phenomenon in order to further understand the chaotic behaviour of Eq.(3.17).

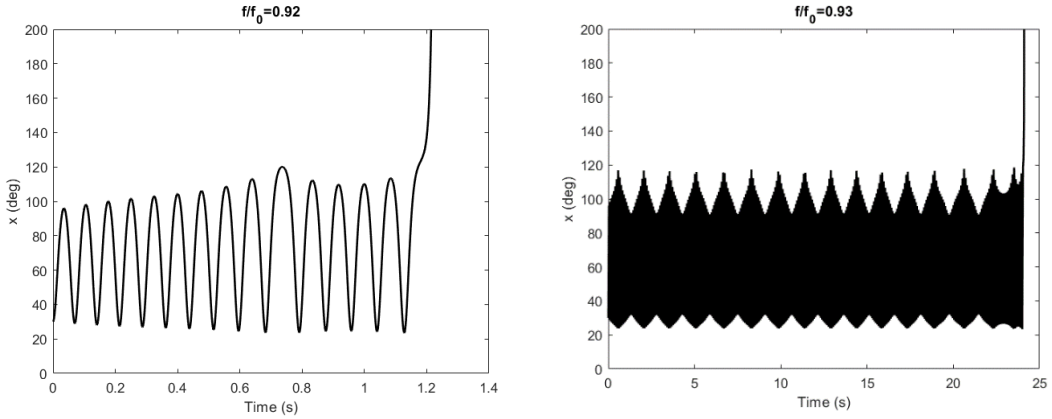


**Figure 3.8: System divergence for different acceleration ripple frequencies**

In Fig.3.9 the maximum transmission error for different non-dimensional acceleration with respect to the ratio $f/f_0$ is presented.

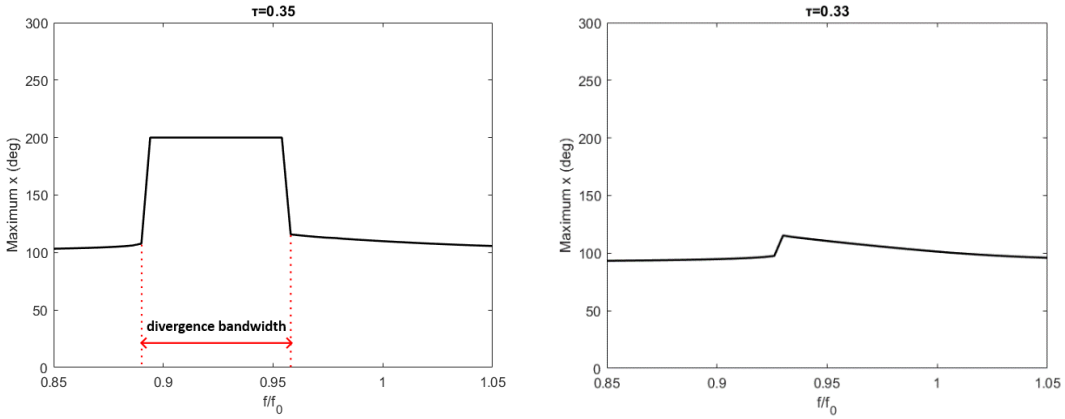


**Figure 3.9: Maximum transmission error for different acceleration ripple frequencies**

From Fig.3.9 it can be observed that for the case of $\tau = 0.35$ the system will diverge for a given bandwidth of the ratio $f/f_0$. The bandwidth is increased when compared to the case of $\tau = 0.34$ presented in Fig.3.6. This phenomenon, is expected since the sum of $(\gamma + \tau)$ is closer to the critical value. However, for the case of $\tau = 0.33$ the system does not diverge for any frequency of the ripple which validates the fact that the sum of $(\gamma + \tau)$ should be close to the critical value in order for the system to diverge under any frequency of the acceleration ripple $(f)$.

For the case of $\tau = 0.35$ and $\varepsilon = 0$ Eq. (3.15) yields $f_0 = 13.697$ Hz while for the case of $\tau = 0.33$ and $\varepsilon = 0$ Eq.(3.15) yields $f_0 = 15.079$ Hz.

It is interesting to notice that the same frequency of acceleration ripple could cause the divergence of the system at lower acceleration rates. For instance, an acceleration ripple frequency of $f = 13.3\ \mathrm{Hz}$ could result in divergence of system when $\tau = 0.34$ while the system has a periodical behaviour when $\tau = 0.35$.

Initially this phenomenon, could be regarded as counter intuitive, however it can be explained from Fig.3.6 and Fig.3.9.

For $\tau = 0.34$ the ratio $f/f_0$ is approximately equal to 0.919 while for $\tau = 0.35$ the ratio $f/f_0$ is equal to 0.971. As a result, for the case of $\tau = 0.34$ the oscillation is well within the critical bandwidth while for the case of $\tau = 0.35$ it is outside the critical bandwidth. The transmission error $(x)$ with respect to time is presented in Fig.3.10 for the two cases.

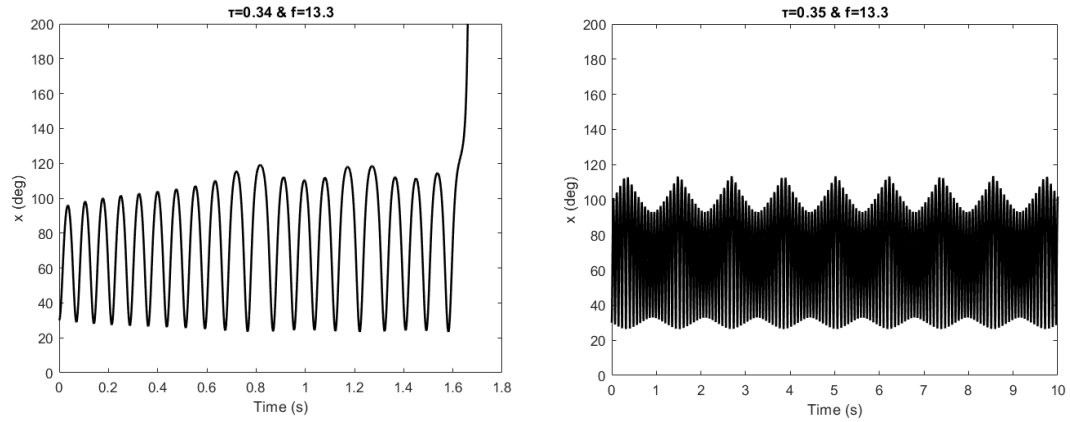


**Figure 3.10: Transmission error for different acceleration and same ripple frequency**

Finally, it is interesting to investigate the effect of the ripple of the acceleration ($\varepsilon$) to the stability of the system. For the case study presented according to the parameters of Table 3.3 and $\gamma = 0.5$ the maximum non-dimensional acceleration ($\tau_{max}$) of the inner rotor was calculated for different values of the ripple of the acceleration. The results are presented in Table 3.5. The maximum percentagewise non-dimensional acceleration ($\tau_{\%}$) is calculated as the ratio of the maximum non-dimensional acceleration under ripple conditions to the maximum non-dimensional acceleration when no ripple is present.

**Table 3.5: Maximum non-dimensional acceleration for different acceleration ripple values**

| $\varepsilon$ (%) | $\tau_{max}$ | $\tau_{\%}$ (%) |
|---|---|---|
| 0 | 0.3696 | 100 |
| 0.5 | 0.3498 | 94.64 |
| 1 | 0.3343 | 90.45 |
| 2 | 0.3049 | 82.49 |
| 5 | 0.2426 | 65.64 |

In Fig.3.11 the maximum percentagewise acceleration ($\tau_{\%}$) with respect to the ripple of acceleration ($\varepsilon$) and the fitted curve are presented.

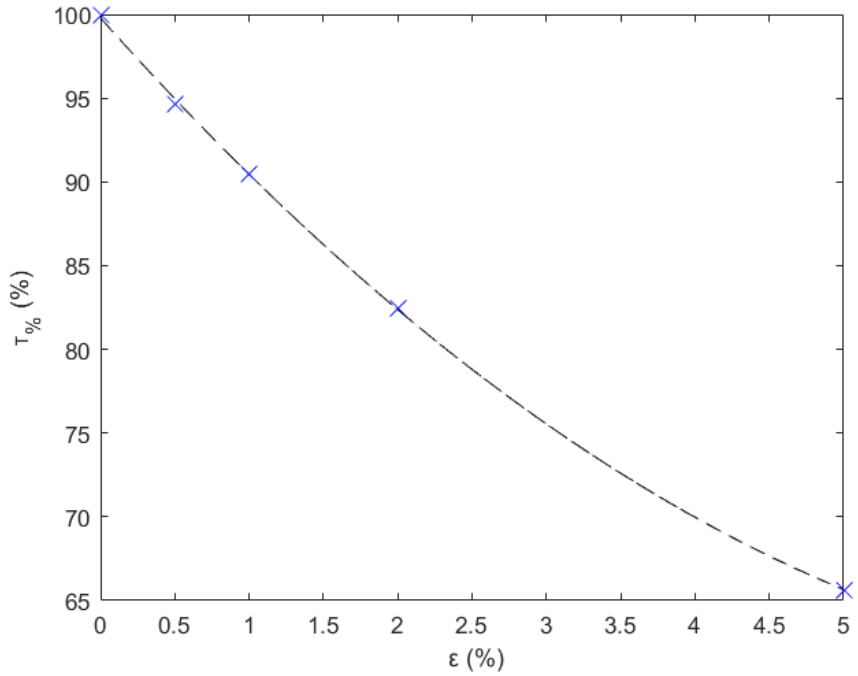


**Figure 3.11: Maximum ($\tau_{\%}$) for different acceleration ripple values ($\varepsilon$) and fitted curve**

As expected the maximum ($\tau_{\%}$) is decreased as the acceleration ripple ($\varepsilon$) is increased.

Furthermore, the effect of the non-dimensional value ($\gamma$) on the maximum percentagewise non-dimensional acceleration ($\tau_{\%}$) for different values of the ripple of the acceleration ($\varepsilon$) was investigated. The results are presented in Table 3.6.

**Table 3.6: Maximum ($\tau_{\%}$) for different acceleration ripple ($\varepsilon$) and non-dimensional ($\gamma$) values**

| $\gamma$ | $\varepsilon$ (%) | $\tau_{max}$ | $\tau_{\%}$ (%) |
|---|---|---|---|
| 0.3 | 0 | 0.5138 | 100 |
| | 0.5 | 0.4858 | 94.55 |
| | 1 | 0.4655 | 90.60 |
| | 2 | 0.4248 | 82.68 |
| | 5 | 0.3372 | 65.63 |
| 0.5 | 0 | 0.3696 | 100 |
| | 0.5 | 0.3498 | 94.64 |
| | 1 | 0.3343 | 90.45 |
| | 2 | 0.3049 | 82.49 |
| | 5 | 0.2426 | 65.64 |
| 0.7 | 0 | 0.2232 | 100 |
| | 0.5 | 0.2116 | 94.80 |
| | 1 | 0.2008 | 89.96 |
| | 2 | 0.1848 | 82.80 |
| | 5 | 0.1469 | 65.82 |

| | | | |
|---|---|---|---|
| 0.9 | 0 | 0.0748 | 100 |
| | 0.5 | 0.0709 | 94.79 |
| | 1 | 0.0676 | 90.37 |
| | 2 | 0.0620 | 82.89 |
| | 5 | 0.0496 | 66.31 |

From the results presented in Table 3.6 it is evident that the non-dimensional value ($\gamma$) has a negligible effect on the maximum percentagewise non-dimensional acceleration of the inner rotor regardless of the acceleration ripple.

From the analysis demonstrated in the present work some engineering insights can be obtained regarding the operation of coaxial magnetic gears. First and foremost it is important to protect the coaxial magnetic gear drive from resonance phenomena due to the oscillations that occur during acceleration. The frequency of the oscillation can be obtained from Eq.(3.15) for every applied outer load and inner rotor acceleration. The highest frequency that can be observed when no external load is applied $(\gamma = 0)$ and a very small acceleration is applied to the inner rotor $(\tau \to 0)$. The frequency of the oscillation calculation for this case is shown in Appendix A3.1. Therefore, to avoid resonant phenomena during acceleration the coaxial magnetic gear should be constructed in a way that the torsional frequencies of the system are significantly higher than the maximum frequency of the oscillations during acceleration. If this consideration is not taken into account then the coaxial magnetic gear could potentially experience high energy vibrations during acceleration that could endanger its operation.

Furthermore, the acceleration of the inner rotor is typically not steady in most engineering applications. For example, an inverter can provide a steady acceleration, however ripple is usually present. From the analysis of the present work it was demonstrated that the ripple of the acceleration could lead to the divergence of the system even if the non-dimensional value of the acceleration is lower than the critical value as obtained from the stability criterion of Eq.(3.13). For that reason, it is critical to examine the frequency of the ripple of the acceleration. It was shown that the system is particularly prone to this phenomenon if the ratio of the frequency of the ripple to the frequency of the oscillation, as obtained from Eq.(3.15), is in the range of 0.92-0.93. If the frequency of the ripple is within that bandwidth, for a given set of non-dimensional constants ($\gamma$) and ($\tau$), then it is vital that the non-dimensional acceleration of the inner rotor is lower than the ($\tau_{\%}$) value depending on the amplitude of the acceleration ripple ($\varepsilon$) as shown in Fig.3.11.

The above considerations should be taken into account when designing a coaxial magnetic gear in order to ensure a stable and robust operation during acceleration

## *Chapter 3-Conclusions*

In the present chapter a non-dimensional stability criterion for the dynamical response of coaxial magnetic gears under steady acceleration and constant applied outer load has been developed. A non-dimensional criterion was derived analytically in order to assess the dynamical convergence of the drive without the requirement of a numerical solution of the dynamical equation of the system. In addition, a closed-form of the period of the oscillations has been derived when a steady acceleration is induced to the system. Furthermore, the case of acceleration with ripple has been investigated since it is common for power transmission drives to operate under ripple. It was demonstrated that for the case of constant applied outer load and acceleration with ripple the non-dimensional governing differential equation is similar to the driven pendulum equation that can have chaotic behaviour. A thorough investigation on the effect of ratio between the frequency of the ripple and the frequency of the oscillation obtained for steady acceleration was conducted. A case study was performed where the effect of the ripple frequency was investigated. It was observed, that when the ratio was between 0.9-0.95 the system could exhibit divergence even if the applied acceleration was lower than the critical value. Furthermore, it was shown that a smaller acceleration with a given ripple frequency could lead to divergence while a higher acceleration with the same ripple frequency could not, a phenomenon that emphasizes the significance of the frequency ratio. In addition, it was observed that the system could appear to have a periodic-like behaviour for a considerable time of operation before it diverges which showcases the chaotic behaviour of the system. Finally, the effect of the ripple of acceleration was investigated. It was shown, that when the acceleration ripple ($\varepsilon$) is increased then the maximum percentagewise acceleration ($\tau_{\%}$) is decreased. Therefore, the developed non-dimensional model could be a valuable tool for the understanding of the dynamical response in coaxial magnetic gears both during steady acceleration and acceleration with ripple that could lead to efficient and robust operation.

## *Appendix A3.1*

The integral of Eq.(3.15) cannot be solved analytically in its general form. However, when no external load is applied ($\gamma = 0$) and a very small acceleration is applied to the system ($\tau \to 0$) both the calculation of ($x_{max}$) and the integral can be solved analytically implementing the Taylor expansion as follows:

The maximum transmission error value ($x_{max}$) can be calculated after simplifying Eq.(3.11) from:

$$\cos x + \tau\, x - 1 = 0 \tag{A3.1.1}$$

and since:

$$\cos x = 1 - \frac{x^2}{2!} + \frac{x^4}{4!} - \cdots + \cdots \tag{A3.1.2}$$

From Eq.(A3.1.1) and Eq.(A3.1.2) and neglecting the higher order terms we obtain:

$$x_{max} = 2\tau \tag{A3.1.3}$$

Therefore, Eq.(3.15) takes the following form:

$$T_0 = \frac{\sqrt{2}}{\omega_0} \int_0^{2\tau} \frac{dx}{\sqrt{-\frac{x^2}{2} + \tau\, x}} \tag{A3.1.4}$$

which could be written as:

$$T_0 = \frac{\sqrt{2}}{\omega_0} \int_0^{2\tau} \frac{\sqrt{2}dx}{\sqrt{\tau^2 - (x - \tau)^2}} \tag{A3.1.5}$$

By substituting $u = x - \tau$ and $w = \frac{u}{\tau}$ yields that:

$$T_0 = \frac{2}{\omega_0} \int_{-1}^{1} \frac{dw}{\sqrt{1 - w^2}} \tag{A3.1.6}$$

Therefore:

$$T_0 = \frac{2\pi}{\omega_0} \tag{A3.1.7}$$

## *Chapter 3-References*

[3.1] Frandsen, T. V., & Rasmussen, P. O. (2015, October). Slip torque investigation and magnetic redesign of motor integrated permanent magnet gear. In 2015 18th International Conference on Electrical Machines and Systems (ICEMS) (pp. 929-935). IEEE.

[3.2] Montague, R., Bingham, C., & Atallah, K. (2011). Servo control of magnetic gears. IEEE/Asme Transactions on Mechatronics, 17(2), 269-278.

[3.3] Montague, R. G., Bingham, C., & Atallah, K. (2012). Magnetic gear pole-slip prevention using explicit model predictive control. IEEE/ASME Transactions on Mechatronics, 18(5), 1535-1543.

[3.4] Tzouganakis, P., Gakos, V., Kalligeros, C., Tsolakis, A., & Spitas, V. (2023). Fast and efficient simulation of the dynamical response of coaxial magnetic gears through direct analytical torque modelling. Simulation Modelling Practice and Theory, 123, 102699.

[3.5] Hastings, S. P., & McLeod, J. B. (1993). Chaotic motion of a pendulum with oscillatory forcing. The American mathematical monthly, 100(6), 563-572.

[3.6] Van Dooren, R. (1996). Chaos in a pendulum with forced horizontal support motion: a tutorial. Chaos, Solitons & Fractals, 7(1), 77-90.

[3.7] Zhang, X., Liu, X., Wang, C., & Chen, Z. (2014). Analysis and design optimization of a coaxial surface-mounted permanent-magnet magnetic gear. Energies, 7(12), 8535-8553.

[3.8] Tzouganakis, P., Gakos, V., Kalligeros, C. et al. Formulation of a non-dimensional criterion for stable dynamical response in coaxial magnetic gears. J Eng Math 144, 19 (2024).

# 4 Power losses in coaxial magnetic gears

Power losses should be investigated during the design of coaxial magnetic gear drives in order to achieve optimal efficiency and avoid phenomena that could lead to the degradation of the system as a whole. In particular, eddy current losses have been a significant issue in CMGs especially in higher rotational speeds [4.1]. Therefore, it is essential during the design of CMGs drives to investigate this phenomenon, since excess eddy current losses could lead to increase of the temperature and deterioration of the PMs in the rotors that could gradually lead to degradation of the system as a whole.

In general, the calculation eddy current and core losses is a strenuous process that requires complex transient electromagnetic phenomena. Desvaux et al. [4.2] and Wang et al. [4.3] computed the eddy current losses of the PMs, by firstly calculating the square of the current density throughout the PMs and multiplying by the resistivity, then performing a volume integration and finally integrating with respect to time and dividing by the period of the system, to get the average value of the eddy current losses. They also performed tangential magnet segmentation to decrease the eddy current losses, by performing the volume integration on each segment separately. Filippini [4.4] performed both tangential and axial magnet segmentation and correlated the eddy current losses and the number of segments to a rational function. Regarding core losses, Filippini [4.4] starts with the computation of the induction throughout the ferromagnetic segments, with a simple finite-difference model that utilizes the boundary scalar magnetic potential conditions and the Laplace equation in cylindrical coordinates. Core losses, according to Deng [4.5], require using the rate of change of the induction to calculate hysteresis, eddy current and excess losses. Deng introduced a formula to calculate these losses while including the harmonic effect. Desvaux et al. [4.2] used this formula to perform core losses calculations. Hein et al. [4.6] reviews different approaches of the Steinmetz equation, which calculates hysteresis losses. Lee et al. [4.7] and Li et al. [4.8] propose that for the same magnitude of induction, rotational core losses are almost double the alternating core losses.

The calculation of the power losses, is a computationally high process as it requires the calculation of the magnetic induction in different angles of rotation of the rotors of the CMG. FE models, despite having high accuracy require significant computational time. As a consequence, an optimization process in order to minimize the power losses could potentially be a time consuming procedure. Therefore, a model that would utilize analytical solutions of the magnetic induction in the CMG could significantly reduce the computational cost and facilitate optimization processes and could become a valuable design tool.

This chapter focuses on the computation of PMs and ferromagnetic segments' losses. The analytical solutions of the scalar magnetic potential derived from Maxwell's equations are used to calculate the current density and thus the eddy

current losses of the PMs. Tangential segmentation is also performed to investigate its impact regarding loss reduction. Core losses are determined using a hybrid analytical-finite element model that utilizes the boundary scalar magnetic potential conditions. The resulting PMs and core losses were in excellent coherence with FEA results, while tangential segmentation greatly improved PMs efficiency. In addition, an investigation on the effect of different applied external loads, on the PMs efficiency is conducted. Finally, a study on the average power losses throughout one full period is conducted, along with a mesh sensitivity analysis in order to reduce the computational time without losing accuracy in the obtained results. From the conducted analysis it was demonstrated that the computational time can be reduced up to 80%. The mesh sensitivity analysis showed that mesh resolution is crucial for accurate core losses calculation, as meshes that are too coarse result in inaccurately high core losses while meshes that are too fine result in high computational costs. These two analyses are of great importance, as they ensure high accuracy and relatively low computational costs simultaneously, facilitating optimization efforts.

## *4.1 Mathematical Modelling of Power Losses*

The power losses in coaxial magnetic gears are attributed to eddy current losses in the PMs of the inner and outer rotor and to core losses in the ferromagnetic segments.

### *4.1.1 Eddy current losses in the PMs*

For the calculation of the PM losses the vector magnetic potential $\mathbf{A}$ throughout the PMs is required. The vector magnetic potential can be easily determined after the scalar magnetic potential $\varphi$ calculation as calculated in Chapter 1.

The vector magnetic potential $\mathbf{A}$ can be determined, using the following equations:

$$\mathrm{B_r^k}(\mathrm{r},\theta) = -\mu_0 \frac{\partial \varphi^{\mathrm{k}}}{\partial \mathrm{r}} = \frac{1}{\mathrm{r}} \frac{\partial \mathrm{A^k}}{\partial \theta} \tag{4.1}$$

$$\mathrm{B_\theta^k}(\mathrm{r},\theta) = -\mu_0 \frac{\partial \varphi^{\mathrm{k}}}{\partial \theta} = -\frac{\partial \mathrm{A^k}}{\partial \mathrm{r}} \tag{4.2}$$

where $\mathrm{B_r^k}$ and $\mathrm{B_\theta^k}$ are the radial and tangential induction of a point of the inner and outer rotor ($\mathrm{k}$:in or out), $\mathrm{r}$ and $\theta$ refer to the polar coordinates and $\mu_0$ is the vacuum permeability.

The eddy current losses for each PM are computed using the following formula [4.2]:

$$\mathrm{P_{eddy}^k} = \frac{\mathrm{L}}{\Theta_\mathrm{p}^\mathrm{k}} \int_0^{\Theta_\mathrm{p}^\mathrm{k}} \frac{1}{\sigma} \int_{\mathrm{S_{PM}^k}} \left( \left( \mathrm{J^k} \right)^2 \mathrm{r dr d\theta} \right) \mathrm{d\theta_0^k} \tag{4.3}$$

$$\mathrm{J^k}\left(\mathrm{r},\theta,\theta_0^\mathrm{k}\right) = \sigma \omega^\mathrm{k} \frac{\partial \mathbf{A}^\mathrm{k}}{\partial \theta_0} + \mathrm{C^k}(\theta_0^\mathrm{k}) \tag{4.4}$$

$$\mathrm{C^k}\left(\theta_0^\mathrm{k}\right) = -\frac{1}{\mathrm{S_{PM}^k}} \int_{\mathrm{S_{PM}^k}} \sigma \omega^\mathrm{k} \frac{\partial \mathbf{A}^\mathrm{k}}{\partial \theta_0^\mathrm{k}} \mathrm{r dr d\theta} \tag{4.5}$$

where $J^k$ is the eddy current density, $C^k$ is a term used to guarantee that the net current flowing in each PM arc segment is zero at any moment, $S_{PM}^k$ is the area of a PM and $\sigma$ is the conductivity of the PMs. $\theta_0^k$ and $\omega^k$ refer to the angle of rotation and the rotational speed of each rotor, while $\Theta_p^k$ is the angle that each rotor rotates in a complete period of the system.

For the calculation of $\Theta_p^k$, one must find the greatest common divisor of $p_{in}$ and $p_{out}$, and divide them with it. The result of this simple operation is the amount of revolutions the outer and inner rotor, respectively, complete in a period. For example, if $p_{in} = 4$ and $p_{out} = 10$, means that the inner rotor completes 5 revolutions, while the outer rotor completes 2 revolution in a period, resulting in $\Theta_p^{in} = 10\pi\ \text{rad}$ and $\Theta_p^{out} = 4\pi\ \text{rad}$.

### *4.1.2 Tangential segmentation of PMs*

Eddy currents losses in PMs can be reduced with their axial or tangential segmentation. The present work focuses on tangential segmentation. Incorporating tangential segmentation into the analytical model requires partitioning the angle, with respect to which the integration is performed, by the number of total segments ($K_{in}, K_{out}$), as shown in Eq. (4.6) [4.3] for each rotor.

$$\theta \in \left[\theta_0, \theta_0 + \frac{\pi}{p_{in}}\frac{1}{K_{in}}\right], \theta \in \left[\theta_0, \theta_0 + \frac{\pi}{p_{out}}\frac{1}{K_{out}}\right] \tag{4.6}$$

An example of tangential segmentation is presented in Fig. 4.1.

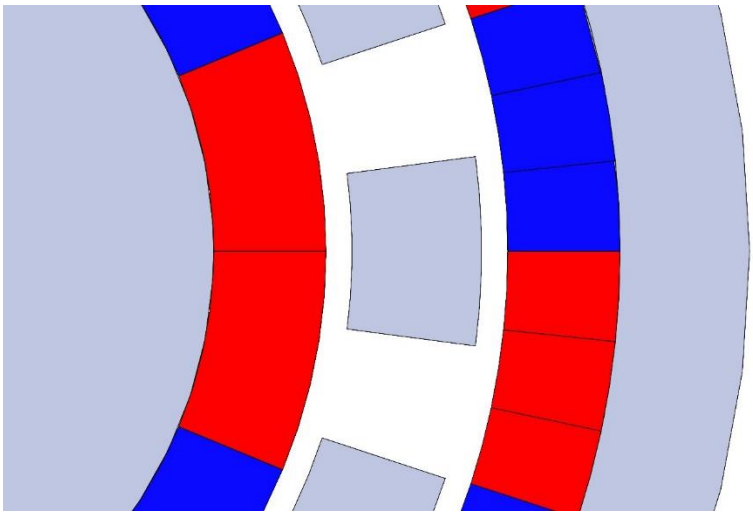

**Figure 4.1: Illustration of magnet segmentation ($K_{int} = 2$ and $K_{out} = 3$).**

### *4.1.3 Computation of core losses of the ferromagnetic segments using a hybrid model*

In a special case of sinusoidal variation of the magnetic fields, core losses are calculated from [4.2]:

$$P_{\text{core, sinusoidal}} = n\left(k_{\text{hyst}} f^{\alpha} B_m^{\beta} + k_{\text{eddy}} f^2 B_m^2 + k_{\text{exc}} f^{1.5} B_m^{1.5}\right) \tag{4.7}$$

where $f$ and $B_m$ are the frequency and peak value of the induction, respectively, and $\alpha, \beta, k_{\text{hys}}, k_{\text{eddy}}$ and $k_{\text{exc}}$ are constants that depend on the material and are provided by the manufacturer. Rotational fields results in core losses that are double those produced from alternating fields [4.7], [4.8]. This is denoted in Eq.(4.7) with the variable $n$, which has a value of $1$ when referring to alternating fields and $2$ when referring to rotating fields, as in this case.

In general, fields in CMGs do not appear with a strict sinusoidal variation, so a generalized equation is used to calculate the core losses [4.2], [4.5], [4.6]:

$$\begin{aligned} &P_{\text{eddy}}^{F} = P_{\text{core,generalised}} = \\ &L \int_{S_{\text{fer}}} n \left( \frac{k'_{\text{hyst}}}{T} \int_O^T \left| \sqrt{\left(\frac{dB_{\text{maj}}}{dt}\right)^2 + \left(\frac{dB_{\text{min}}}{dt}\right)^2} \right|^{\alpha} \left| \sqrt{B_{\text{maj}}^2 + B_{\text{min}}^2} \right|^{\beta-\alpha} dt + \right. \\ &+ \frac{k'_{\text{eddy}}}{T} \int_0^T \left( \left(\frac{dB_{\text{maj}}}{dt}\right)^2 + \left(\frac{dB_{\text{min}}}{dt}\right)^2 \right) dt + \\ &\left. \frac{k'_{\text{exc}}}{T} \int_0^T \left( \left(\frac{dB_{\text{maj}}}{dt}\right)^2 + \left(\frac{dB_{\text{min}}}{dt}\right)^2 \right)^{0.75} dt \right) r dr d\theta \end{aligned} \tag{4.8}$$

$$\begin{cases} k'_{\text{hyst}} = \dfrac{k_{\text{hyst}}}{2^{\beta-\alpha}(2\pi)^{\alpha-1} \int_0^{2\pi} |\cos\theta|^{\alpha} d\theta} \\ k'_{\text{eddy}} = \dfrac{k_{\text{eddy}}}{2\pi^2} \\ k'_{\text{exc}} = \dfrac{k_{\text{exc}}}{(2\pi^2)^{0.75}} \end{cases} \tag{4.9}$$

$B_{\text{maj}}$ and $B_{\text{min}}$ represent the major and minor axes of the ellipse fitted to the induction locus. $S_{\text{fer}}$ refers to the area of a segment, while $T$ is a complete period of the system.

$B_{\text{maj}}(t)$ and $B_{\text{min}}(t)$ are calculated using the following equations:

$$B_{\text{maj}}(r, \theta, t) = \|B(r, \theta, t)\| \cos\left(a(t)\right) \tag{4.10}$$

$$B_{\text{min}}(r, \theta, t) = \|B(r, \theta, t)\| \sin\left(a(t)\right) \tag{4.11}$$

$$\xi(r, \theta) = \arctan\left( \frac{B_r\left(r, \theta, t_{\max\|B(r,\theta,t)\|}\right)}{B_\theta\left(r, \theta, t_{\max\|B(r,\theta,t)\|}\right)} \right) \tag{4.12}$$

$$a(r, \theta, t) = \arctan\left( \frac{B_r(r, \theta, t)}{B_\theta(r, \theta, t)} \right) - \xi(r, \theta) \tag{4.13}$$

where ξ and a(t) are defined in Fig. 4.2.

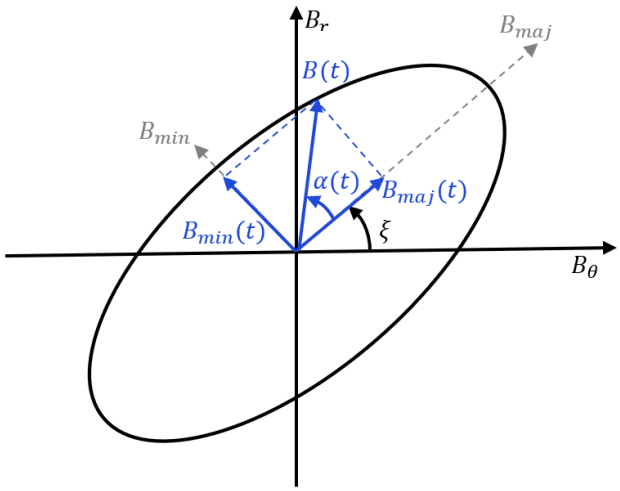


**Figure 4.2: A sketch of the fitted ellipse, along with the parameters required for core loss calculations.**

In order to calculate the core losses, the values of $B_r$ and $B_\theta$ on the ferromagnetic segment's surface should be calculated. However, the analytical model developed in Chapter 1 doesn't calculate the scalar magnetic potential of the segments, but it does calculate the magnetic potential on their boundaries. Those analytically calculated values can be used as boundary conditions for a finite element model. This model makes use of the Laplace's equation of the scalar magnetic potential φ in a cylindrical coordinate system [4.4].

$$\frac{\partial^2 \varphi}{\partial r^2} + \frac{1}{r}\frac{\partial \varphi}{\partial r} + \frac{1}{r^2}\frac{\partial^2 \varphi}{\partial \theta^2} = 0 \tag{4.14}$$

A grid is created, using the reference system shown in Fig. 4.3. The average radius $r_i$ and angle $\theta_j$ of each module are calculated as in Eq. (4.15-4.16), where $\Delta r = (r_4 - r_3)/N$ and $\Delta\theta = \delta/N$, where N is the number of rows and columns of the finite element grid.

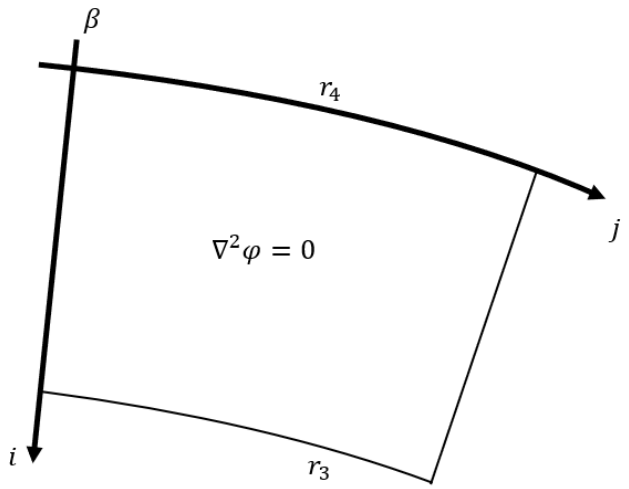


**Figure 4.3: The reference system of the finite element grid.**

$$\mathrm{r_i} = \mathrm{r_4} - \left(\mathrm{i} - \frac{1}{2}\right)\Delta\mathrm{r} \tag{4.15}$$

$$\theta_\mathrm{j} = \beta - \left(\mathrm{j} - \frac{1}{2}\right)\Delta\theta \tag{4.16}$$

Using central finite differences, Laplace's equation leads to a system of $\mathrm{N}^2$ equations, presented in the following equations:

$$\mathrm{D_{N^2xN^2}}\ \Phi_{\mathrm{N^2x1}} = \mathrm{R_{N^2x1}} \tag{4.17}$$

For all $(\mathrm{i},\mathrm{j})$ pairs where $\mathrm{i} = 1$ or $\mathrm{i} = \mathrm{N}$ or $\mathrm{j} = 1$ or $\mathrm{j} = \mathrm{N}$, the corresponding modules of $\mathrm{D}, \Phi$ and $\mathrm{R}$ are assigned values according to Eq. (4.18), where $\varphi(\mathrm{r_i}, \theta_\mathrm{j})$ is the boundary condition. For the rest of the $(\mathrm{i},\mathrm{j})$ pairs, Eq. (4.19) is followed.

$$\begin{cases} \mathrm{D_{(i-1)N+j,(i-1)N+j}} = 1 \\ \mathrm{R_{(i-1)N+j,1}} = \varphi(\mathrm{r_i}, \theta_\mathrm{j}) \end{cases} \tag{4.18}$$

$$\begin{cases} \mathrm{D_{(i-1)N+j,(i-1)N+j}} = -\frac{2}{\Delta\mathrm{r}^2} - \frac{2}{\mathrm{r}^2\Delta\theta^2} \\ \mathrm{D_{(i-1)N+j,(i-1)N+j+1}} = \frac{1}{\mathrm{r}^2\Delta\theta^2} \\ \mathrm{D_{(i-1)N+j,(i-1)N+j-1}} = \frac{1}{\mathrm{r}^2\Delta\theta^2} \\ \mathrm{D_{(i-1)N+j,(i-1)N+j+N}} = \frac{1}{\Delta\mathrm{r}^2} + \frac{1}{2\mathrm{r}\Delta\mathrm{r}} \\ \mathrm{D_{(i-1)N+j,(i-1)N+j-N}} = \frac{1}{\Delta\mathrm{r}^2} - \frac{1}{2\mathrm{r}\Delta\mathrm{r}} \\ \mathrm{R_{(i-1)N+j,1}} = 0 \end{cases} \tag{4.19}$$

Solving for $\Phi_{\mathrm{N^2x1}}$ returns the scalar magnetic potential $\varphi(\mathrm{r_i}, \theta_\mathrm{j})$ on every module of the grid. $\mathrm{B_r}$ and $\mathrm{B_\theta}$ on the ferromagnetic segment can now be calculated using Eq. (4.1, 4.2) and the core losses can be calculated.

## *4.2 Results and discussion*

### *4.2.1 Eddy current and core losses calculation and comparison with FEA*

A case study is performed with the parameters described in Table 4.1. The rotational speed of the inner rotor is assumed to be 2500 rpm. The time step used is equal to the time it takes for the inner rotor to rotate by 2° and, equivalently, for the outer rotor to rotate by 0.8°. This time step allows for high accuracy computations and simultaneously limits the amount of time steps in one period. The computations are performed for the case of full load. An algorithm based on the developed model is constructed in MATLAB. The results were compared to those obtained from the FE transient analysis performed in the Ansys Maxwell software.

**Table 4.1: Parameters of the CMG example used for the calculations**

| | | |
|---|---|---|
| $p_{in}$ | Number of inner ring pole pairs | $4$ |
| $p_{out}$ | Number of outer ring pole pairs | $10$ |
| $Q$ | Number of ferromagnetic segments | $14$ |
| $r_1$ | Inner radius of inner ring | $53\text{mm}$ |
| $r_2$ | Outer radius of inner ring | $66\text{mm}$ |
| $r_3$ | Inner radius of flux-modulator ring | $69\text{mm}$ |
| $r_4$ | Outer radius of flux-modulator ring | $84\text{mm}$ |
| $r_5$ | Inner radius of outer ring | $87\text{mm}$ |
| $r_6$ | Outer radius of outer ring | $87\text{mm}$ |
| $L$ | Length | $100\text{mm}$ |
| $\delta$ | Ferromagnetic segment angle | $15°$ |
| $B_r$ | Residual induction of magnets | $1.47\text{T}$ |
| $\mu_0$ | Vacuum magnetic permeability | $4\pi \cdot 10^{-7}\ \text{Hm}^{-1}$ |
| $\mu_r^I = \mu_r^{III}$ | Relative permeability of the magnets | $1.05$ |
| $\sigma$ | Conductivity of the magnets | $0.9\text{MS/m}$ |

Fig. 4.4.a shows that the eddy current losses of the PMs are proportional to the square of the rotational speed of the rotors, while Fig. 4.4.b shows that the percentage of eddy current losses to total transmitted power is proportional to the rotational speed of the rotors, as expected from Eq.(4.3-4.5).

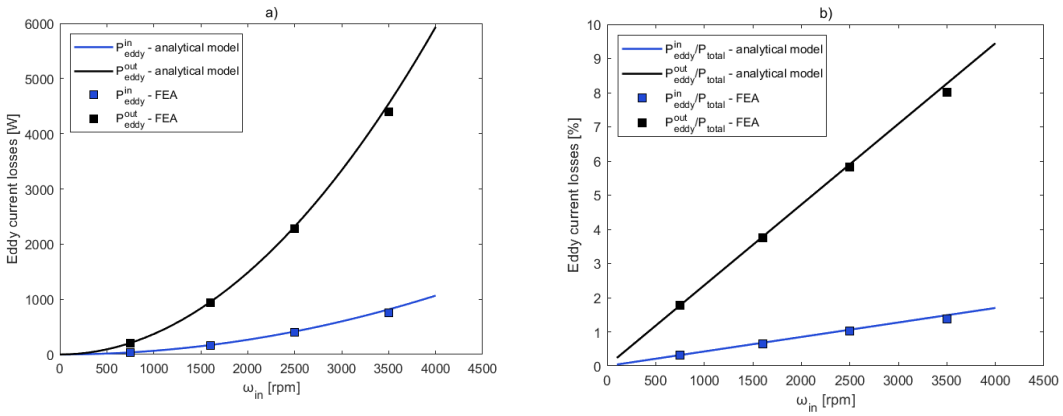


**Figure 4.4: Comparison of results obtained from the analytical model and the 2D finite element analysis model regarding: a) eddy current losses and b) percentage of eddy current losses to total transmitted power.**

It is observed that the eddy current losses on the outer rotor are higher compared to the inner rotor, a result that is in coherence with similar studies in the literature [4.2], [4.4]. In addition the total eddy current losses in the PMs exceed 5% of the total transmitted power after 2000 rpm, illustrating the drawback of CMGs in high rotational speeds which has also been reported in the literature [4.1]. The analytical results of the developed model were verified with FEA. The discrepancies between the analytical model and the FEA simulations are small and of the same nature for both rotors. For slower rotational speeds, the analytical model results in slightly less eddy current losses, 0.01% for the inner rotor and 0.9% for the outer rotor PMs less that FEA simulations for an inner rotational speed of 750rpm. As rotational speeds increase, the analytical model results in larger eddy current losses, reaching deviances of 7.8% and 3.1% for the inner and outer rotor PMs, respectively, for an inner rotational speed of 3500rpm.

Fig. 4.5 shows the effect of magnet segmentation on the eddy current losses.

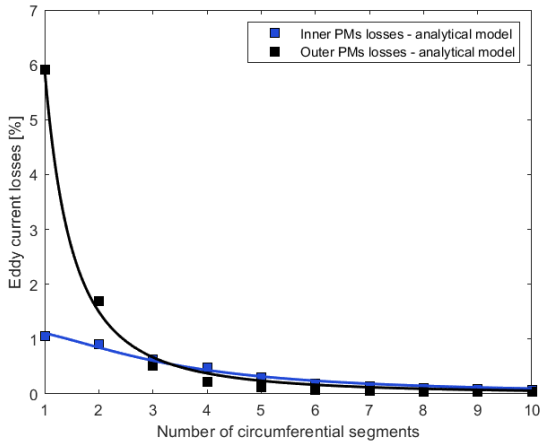


**Figure 4.5. Tangential segmentation effects on the eddy currents losses of the PMs.**

The losses decrease rapidly in the outer rotor and more slowly in the inner rotor, as tangential segments increase. According to Fillipini [4.4], the eddy current losses

should follow the function $\mathrm{P_{eddy}}(\mathrm{K_k}) = \frac{\mathrm{c}}{\mathrm{a^2+b^2K_k^2}}$, where $\mathrm{K_k}$ is the number of tangential segments of every PM of a rotor and $\mathrm{a}, \mathrm{b}, \mathrm{c}$ are constants.

Fitting this function results in a coefficient of determination of $R^2 = 0.9842$ and $R^2 = 0.9963$, for the inner and outer PMs losses, while the values of $a, b$ and c are equal to 0.115, 0.039 and 0.016 for the inner PMs and 0.031, 0.215 and 0.280 for the outer PMs, respectively.

For the calculation of the core losses some additional parameters are required and are presented in Table 4.2.

**Table 4.2: Parameters used in this case study for the calculation of core losses**

| | | |
|---|---|---|
| $\mathrm{k_h}$ | Hysteresis loss coefficient | $152.2\mathrm{WsT^{-\beta}m^{-3}}$ |
| $\mathrm{k_{ed}}$ | Eddy current loss coefficient | $0.403\mathrm{Ws^2T^{-2}m^{-3}}$ |
| $\mathrm{k_{ex}}$ | Excess loss coefficient | $0.1\mathrm{Ws^{1.5}T^{-1.5}m^{-3}}$ |
| $\alpha$ | Steinmetz coefficient | 1 |
| $\beta$ | Steinmetz coefficient | 2 |

The induction locus of a single finite element of a ferromagnetic segment and its fitted ellipse is presented in Fig. 4.6.

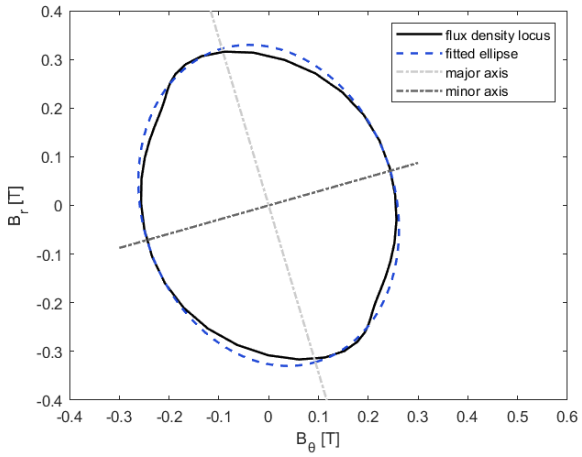


**Figure 4.6: The induction locus of a finite element of a ferromagnetic segment, the fitted ellipse and its axes.**

The resulting induction of the proposed hybrid model on a ferromagnetic segment at a random point in time is shown in Fig. 4.7. For the ferromagnetic segments, a 60x60 mesh grid is used.

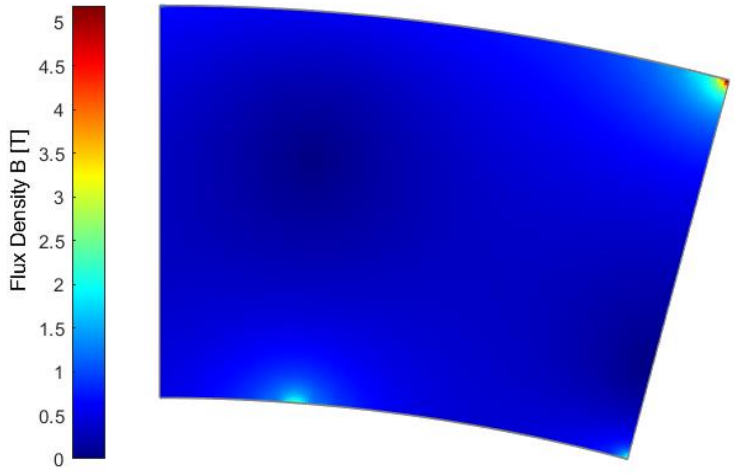


**Figure 4.7: Induction distribution on a ferromagnetic segment.**

Induction is generally close to zero and smooth, except for some small areas around the edges, and especially the corners, where it can reach values as high as $5\mathrm{T}$.

Fig. 4.8.a) and 4.8.b) compare the computed results to those obtained using FEA, for various rotational speeds.

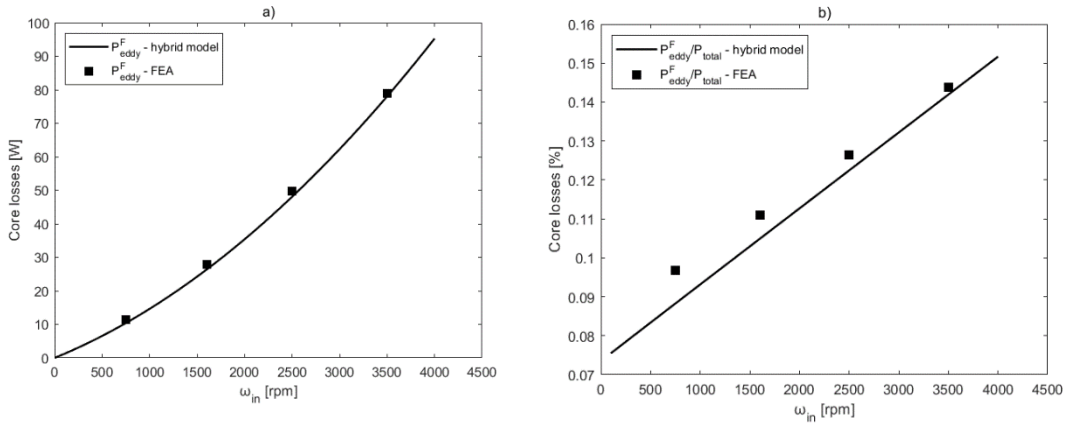


**Figure 4.8: Comparison of results obtained from the hybrid model and the 2D finite element analysis model regarding: a) core losses and b) percentage of core losses to total transmitted power.**

Core losses were found to be one order of magnitude less that inner PMs losses and two orders of magnitude less that outer PMs losses. Specifically, the core losses do not exceed 0.2% of the total transmitted power, even at high rotational speeds. The results of the analytical model were compared to those obtained from FEA. Higher discrepancies in core losses between the results from the hybrid model and the FEA software for lower rotational speeds, that are further highlighted in Fig. 4.8.b), can be attributed to the overall lower losses, that make slight deviations stand out. However, the discrepancies don't surpass $10\%$ for an inner rotational speed greater than 500rpm, and they decrease, percentage-wise, as the rotational speeds increase.

### *4.2.2 Power losses for different external loads*

Different external loads result in different relative positions of the two rotors. It would be interesting to investigate how and if the transmitted load has any effect of the power losses of the CMG. To simplify the calculations, $\theta_{out}$ is initialized as zero, and $\theta_{in}$ is assigned different values that correspond to certain percentages of stall torque. In addition, only PMs losses were taken into account, as core losses are two orders of magnitude less that total PMs losses, while having a greater computational cost. Fig. 4.9 illustrates how, in this case study, the efficiency peaks at about $88\%$ load. Total losses for the case of 88% of the stall torque are 5.5% lower than for the case of full load.

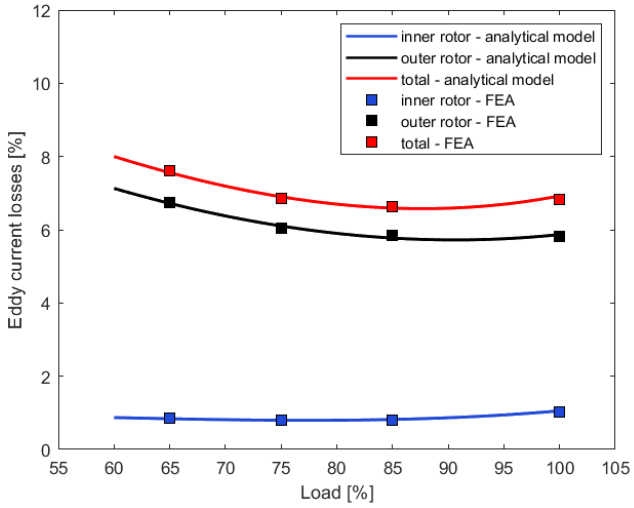


**Figure 4.9: PMs power losses as a percentage of total power transmitted versus load.**

The analytical results were verified and found to be in excellent coherence with FEA. Overall, deviances between the two methods do not exceed 1.5%.

### *4.2.3 Algorithm computational cost vs accuracy*

For the calculation of the eddy current losses a full period as defined from $\Theta_p^k$ is required. However, the developed model requires time steps throughout one complete period of the system. In addition, the hybrid model for the calculation of core losses requires a meshing technique that could significantly increase the computational cost. Therefore, it is important to investigate how the computational cost could be reduced without losing accuracy in the obtained results.

#### *4.2.3.1 Reduction of time steps*

To reduce computational time, it is investigated whether a period is needed to compute the power losses with adequate accuracy or if the losses converge sooner than that. Therefore, the time of the integration $t_s$ will be investigated. The value $t_s$ can range between 0 and $T$. It is noted that the time step used remains the same in all cases and it is equal to the time it takes for the inner rotor to rotate by 2° and, equivalently, for the outer rotor to rotate by 0.8°.

The average PMs and core losses are calculated for various $t_s$ values. Fig. 4.10 illustrates that the power losses converge rapidly. The computational time cost can be reduced by a factor of 5, with a deviation of less than $2\%$ from the results obtained for a complete period.

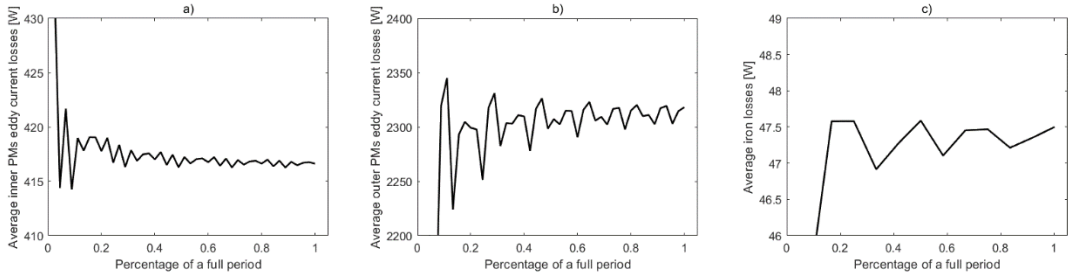


**Figure 4.10: Average power losses versus the percentage of a complete period used to calculate them a) inner PMs, b) outer PMs, c) ferromagnetic segments.**

### *4.2.3.2 Mesh sensitivity analysis*

A mesh sensitivity analysis on the adopted mesh on the ferromagnetic segments is conducted in order to find the optimal mesh resolution that provides accurate core losses results in minimal computational time. Starting from a 10x10 grid and gradually reaching a 120x120 grid, it is found that for a very coarse mesh the computed value of the core losses is significantly larger than their true value, and for finer meshes, the computed losses decrease and converge, as shown in Fig. 4.11.

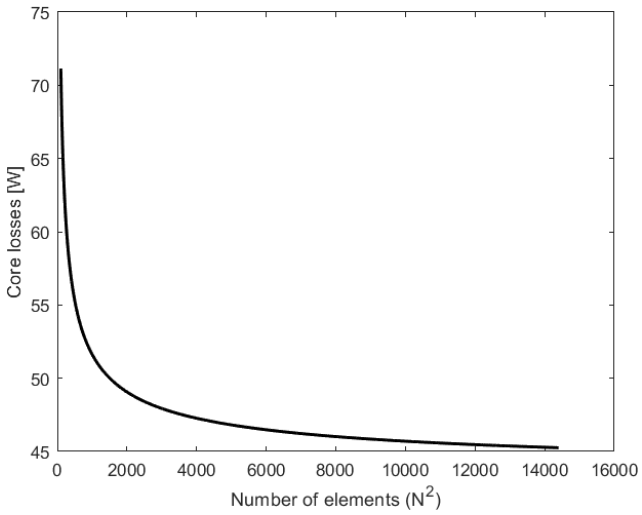


**Figure 4.11: Convergence of core losses using mesh sensitivity analysis.**

Grids ranging from 10x10 to 40x40 don't significantly increase the computational time, as solving the system of $\mathrm{N}^2$ equations requires less of time than calculating the induction values on the boundary of the ferromagnetic segments, as obtained in the methodology followed in Chapter 1. However, the finer the meshes get, the computations get more time consuming, as it is known that solving a system of linear equations can have a complexity of up to $\mathrm{O}(\mathrm{N}^3)$.

Coarse meshes lead to greater computed core losses because, as shown in Fig. 4.7, the largest values of induction and the corresponding time derivatives, which define the losses, are concentrated in small areas near the edges and corners of each ferromagnetic segment. This means that a coarse mesh attributes a large value of $\frac{dB_{maj}}{dt}$ and $\frac{dB_{min}}{dt}$ to a relatively large element, resulting in greater computed core losses. Thus, it is imperative that areas near the edges of the ferromagnetic segments have a mesh that is fine enough to accurately determine the induction distribution. Future research could conduct mesh sensitivity analysis with a focus on utilizing finer mesh near the boundaries and gradually transitioning to coarser mesh towards the center, where induction is generally smoother, to reduce a significant percentage of computational time.

## *Chapter 4-Conclusions*

In the chapter an analytical 2D model is used to calculate eddy currents losses in the PMs of a coaxial magnetic gear, as well as their minimization using magnet segmentation. A hybrid model is used to calculate the core losses in the ferromagnetic segments of the flux-modulator ring. The model utilizes the analytically computed values of the scalar magnetic potential on the boundaries of the segments and uses Laplace's equation in order to compute the magnetic induction throughout the segments for the calculation of the core losses. Both models are validated using a transient FEA simulation which shows a convergence of 1.51% and 3.18% for the eddy current and core losses respectively, for an indicative inner rotor speed of 2500rpm. It was demonstrated that as expected the total power losses increase as the rotational speed increase. The segmentation of the PMs was shown to play a crucial role in reducing the eddy current losses. The method showed that by performing just 2 segmentations on the outer rotor PMs, the overall losses decrease by over one order of magnitude. In addition, an investigation of the effect of the initial positioning of the rotors shows that peak efficiency is achieved at about 88% load in the performed case study. Finally, an attempt to reduce computational time while keeping the accuracy high is made, by proving that only a small fraction of the period of the system is needed in order to accurately calculate total losses and by performing a mesh sensitivity analysis on the adopted grid the ferromagnetic segments. The results of average power losses throughout one full period illustrate the rapid convergence of power losses in a period, which can reduce the computational time by 80% with negligible errors. The mesh sensitivity analysis shows that mesh resolution is crucial for accurate core losses calculation, as meshes that are too coarse result in inaccurately high core losses and meshes that are too fine results in very high computational costs. These two analyses are of great importance, as they ensure high accuracy and relatively low computational costs simultaneously, facilitating optimization efforts. The developed model could be a valuable optimization tool for the reduction of power losses since it combines high accuracy and low computational cost.

## *Chapter 4-References*

[4.1] P. M. Tlali, R. J. Wang, S. Gerber, Magnetic gear technologies: A review, Proceedings - 2014 International Conference on Electrical Machines, ICEM 2014

[4.2] M. Desvaux, S. Sire, S. Hlioui, H. Ben Ahmed and B. Multon, Development of a Hybrid Analytical Model for a Fast Computation of Magnetic Losses and Optimization of Coaxial Magnetic Gears, IEEE Trans. Energy Convers. 34 (1) (2019) 25-35

[4.3] J. Wang, K. Atallah, D. Howe, and P. H. Mellor, Rotor eddy-current loss in permanent-magnet brushless ac machines, IEEE Trans. Magn. 46 (7) (2010) 2701-2707

[4.4] Filippini, Mattia. “Magnetic gears numerical modelling and optimization.” (2019).

[4.5] F. Deng, An improved iron loss estimation for permanent magnet brushless machines, IEEE Trans. Energy Convers. 14 (4) (1999) 1391-1395

[4.6] H. Hein , S. Yue and Y. Li, Comparative Core Loss Calculation Methods for Magnetic Materials under Harmonics Effect, IOP Conference Series: Materials Science and Engineering. 486. 012019 (2019)

[4.7] J.I. Lee, K.H. Shin, T.K. Bang, K.H. Kim, K.Y. Hong, J.Y. Choi, Core-Loss Analysis of Linear Magnetic Gears Using the Analytical Method. Energies. 14(10) (2021)

[4.8] Y. Li, J. Zhu, Q. Yang, Z. W. Lin, Y. Guo, C. Zhang, Study on Rotational Hysteresis and Core Loss Under Three-Dimensional Magnetization, IEEE Trans. Magn., 47(10) (2011) 3520-3523

# 5 Design of an experimental coaxial magnetic gear

The purpose of this chapter is the analysis of the design of a Coaxial Magnetic Gear (CMG) illustrating its key aspects during its design. For the overall system design, a detailed calculation of machine elements was carried out. Following the basic design, special attention was given to the selection of ball bearing clearances with shafts and housings. The study of the system's natural frequencies revealed that the preload of the bearings and, consequently, the operating internal clearance is a crucial factor affecting the natural frequency and the risk of resonance. Furthermore, a simulation was conducted using appropriate software to analyse the thermal losses due to eddy currents, ensuring that the temperature remains within an allowable range to prevent magnet demagnetization. Finally, the effect of the radial forces applied in the modulator ring to the induced torques in the rotors was investigated.

## *5.1 Basic Geometrical Parameters*

The main geometrical parameters of the designed CMG are presented in Table 5.1.

**Table 5.1: Parameters of the designed CMG**

| | | |
|---|---|---|
| $p_{in}$ | Number of inner ring pole pairs | $4$ |
| $p_{out}$ | Number of outer ring pole pairs | $10$ |
| $Q$ | Number of ferromagnetic segments | $14$ |
| $r_1$ | Inner radius of inner ring | $28\text{mm}$ |
| $r_2$ | Outer radius of inner ring | $33\text{mm}$ |
| $r_3$ | Inner radius of flux-modulator ring | $37.5\text{mm}$ |
| $r_4$ | Outer radius of flux-modulator ring | $47.5\text{mm}$ |
| $r_5$ | Inner radius of outer ring | $51\text{mm}$ |
| $r_6$ | Outer radius of outer ring | $56\text{mm}$ |
| $r_{out}$ | Outer radius of outer rotor | $70\text{mm}$ |
| $L$ | Length | $100\text{mm}$ |
| $\delta$ | Ferromagnetic segment angle | $15°$ |

From the analytical model developed in Chapter 1, the stall torque of the inner rotor is 20 Nm while the stall torque of the outer rotor is 50 Nm based on Table 5.1 parameters.

## *5.2 Alternative ways of operation*

During the analysis of the present thesis, it was assumed that inner rotor is the input of the system, the outer rotor the output of the system, while the modulator ring is fixed. However, the modulator ring could also be the output of the system. Therefore, it was deemed necessary in the design of an experimental setup to include both ways of operation. In Fig 5.1, the alternative where the output is the outer rotor is presented:

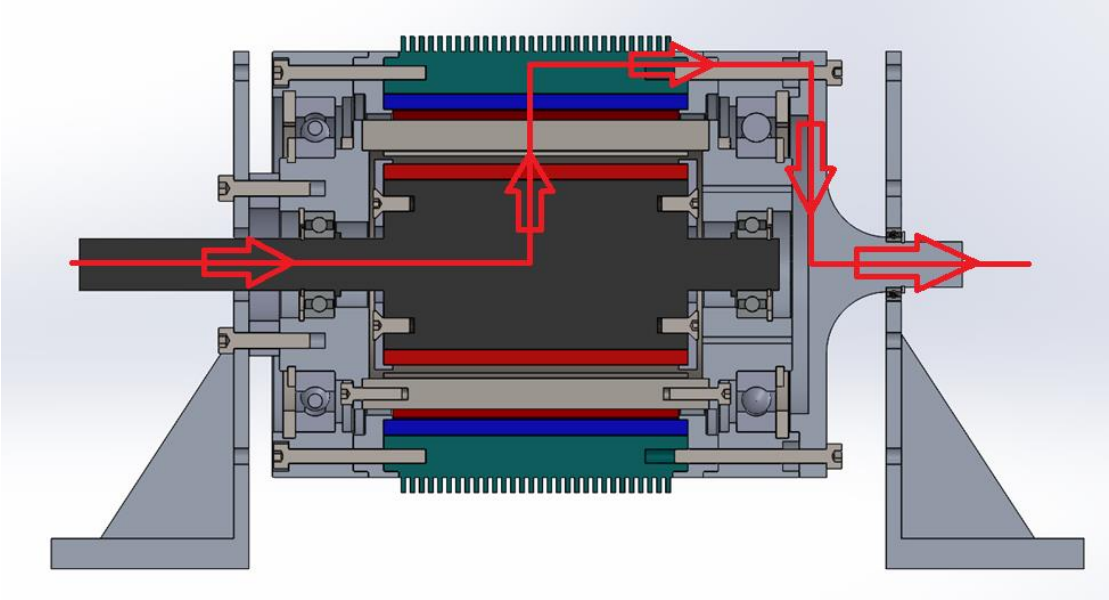

**Figure 5.1: Output from the outer rotor**

In Fig 5.2, the alternative where the output of the CMG is the modulator ring is presented:

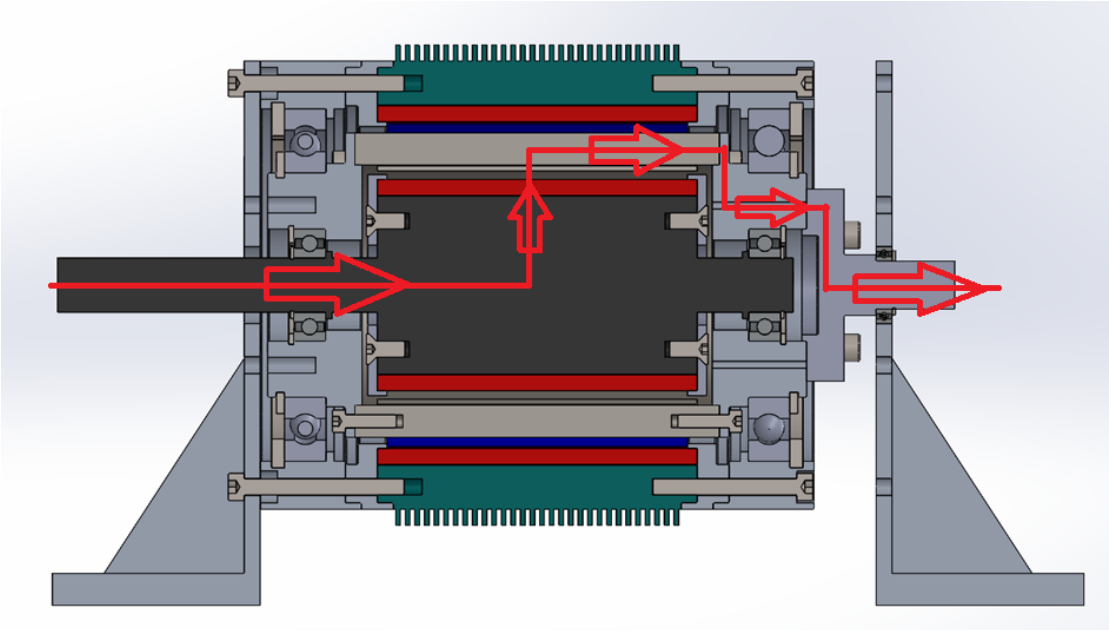

**Figure 5.2: Output from the modulator ring**

## *5.3 Stress on the rotors and modulator ring*

The induced stress on the two rotors and the modulator ring based on the expected torques were calculated with SolidWorks. In Fig. 5.3 the resulting safety factor of the inner rotor is presented:

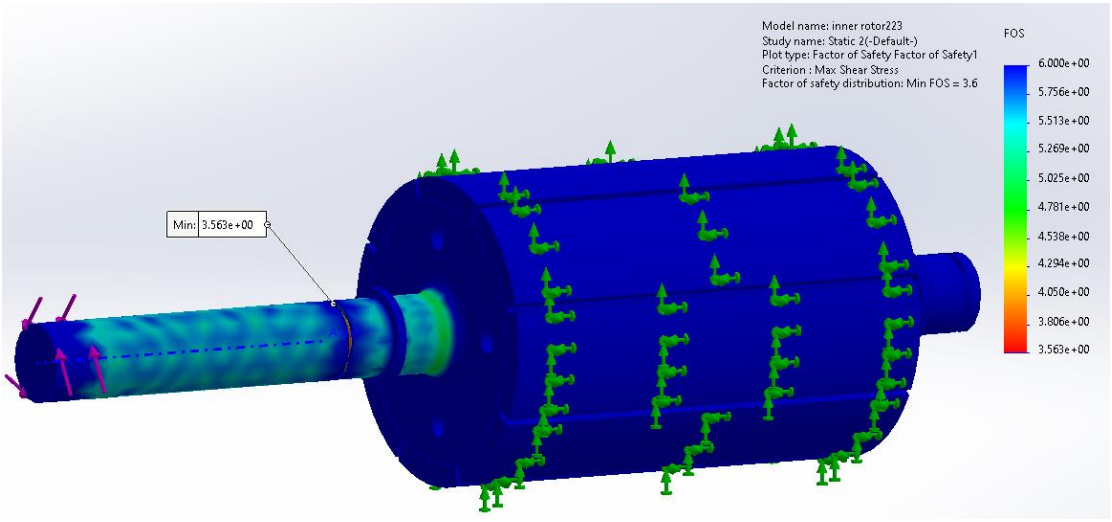


**Figure 5.3: Safety factor of the inner rotor**

It is observed that the applied stresses are well below the critical values since the safety factor is over 3.5 in the entire inner rotor.

In Fig. 5.4 the resulting safety factor of the outer rotor is presented:

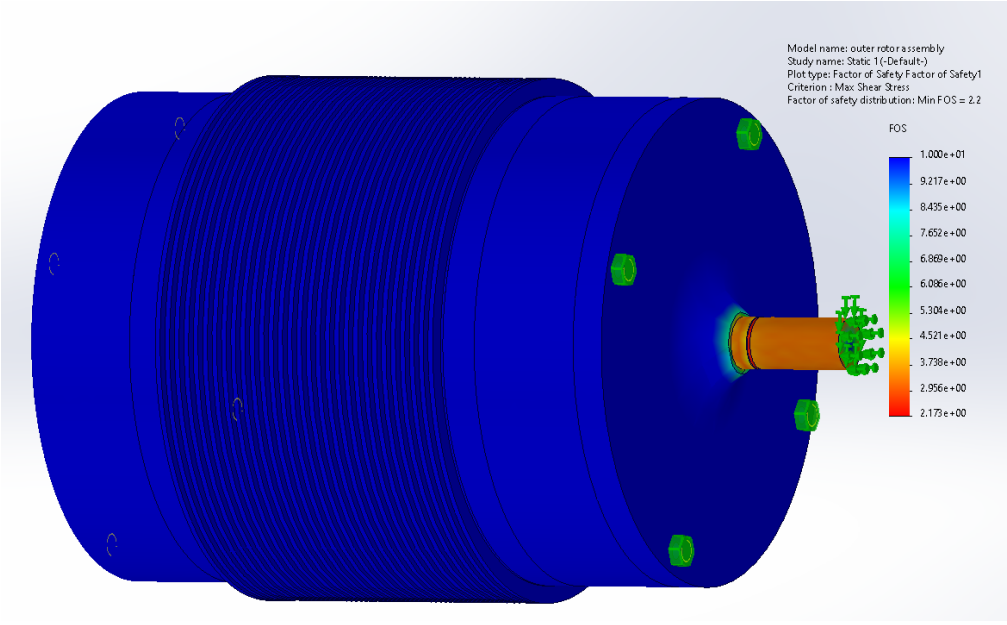


**Figure 5.4: Safety factor of the outer rotor**

It is observed that the applied stresses are well below the critical values since the safety factor is over 2.1 in the entire outer rotor.

For the reduction of the manufacturing cost, the modulator ring is designed as shown in Fig.5.5. The modulator ring is comprised from 14 bars that are connected with bolts.

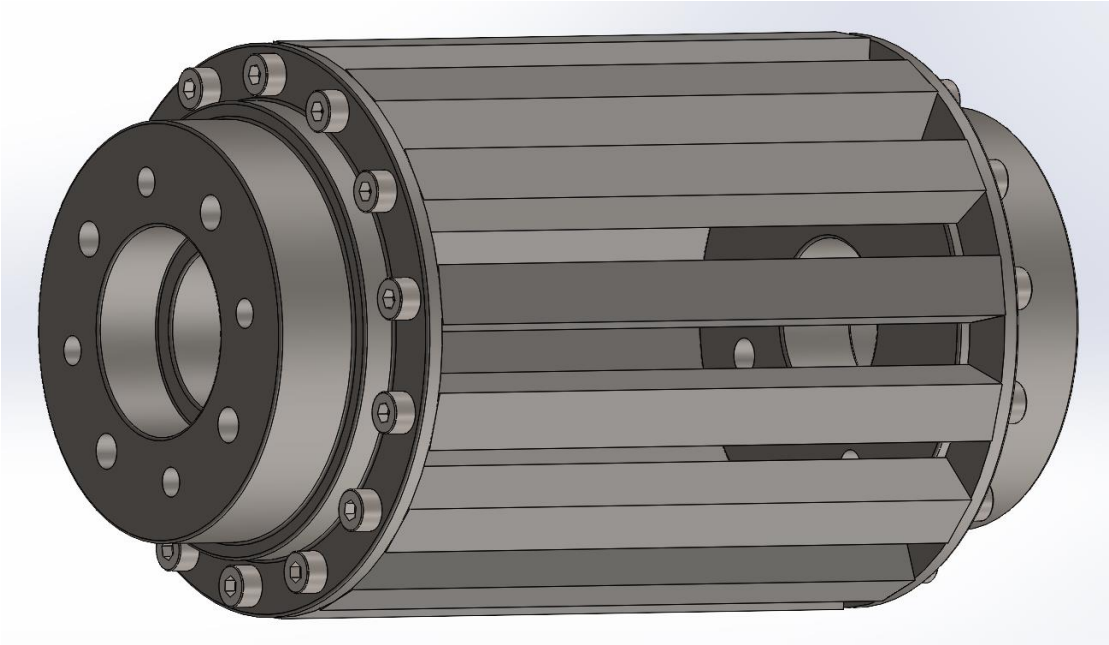

**Figure 5.5: Modulator ring design**

The safety factor of the modulator ring is shown in Fig.5.6. It is observed that stress concentration occurs in the connection of the modulator ring bars with the bolts. However, the safety factor is higher than 1.3 in the entire modulator ring.

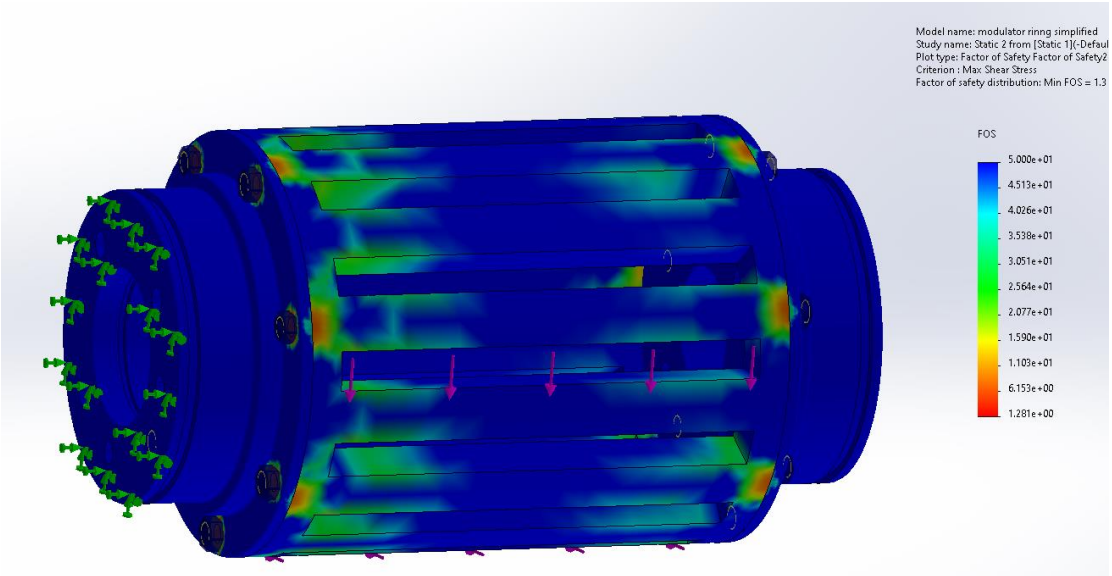


**Figure 5.6: Safety factor of the modulator ring**

## *5.4 Magnet attachment to the rotors*

The placement of the permanent magnets is a crucial aspect for the smooth operation of the CMG. During the operation of the CMG centrifugal forces and radial forces between the magnets are applied that could lead to detachment of the PMs, especially for the case of the inner rotor where the centrifugal force is in the outward direction. To secure the position of the PMs a combination of attachment rings and epoxy glue is employed. In Fig.5.7 the applied stresses on a single PM due to the centrifugal force is presented.

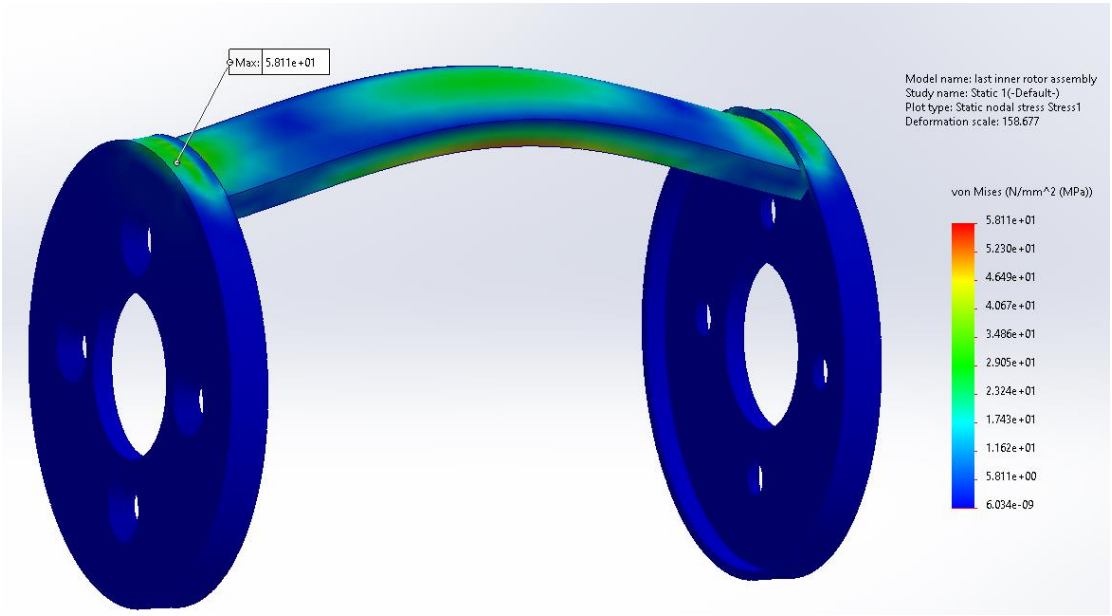


**Figure 5.7: Stress on PM and attachment rings**

For additional security, epoxy glue is placed between the rotors and the PMs using the design shown in Fig.5.8 and Fig.5.9 for the inner rotor.

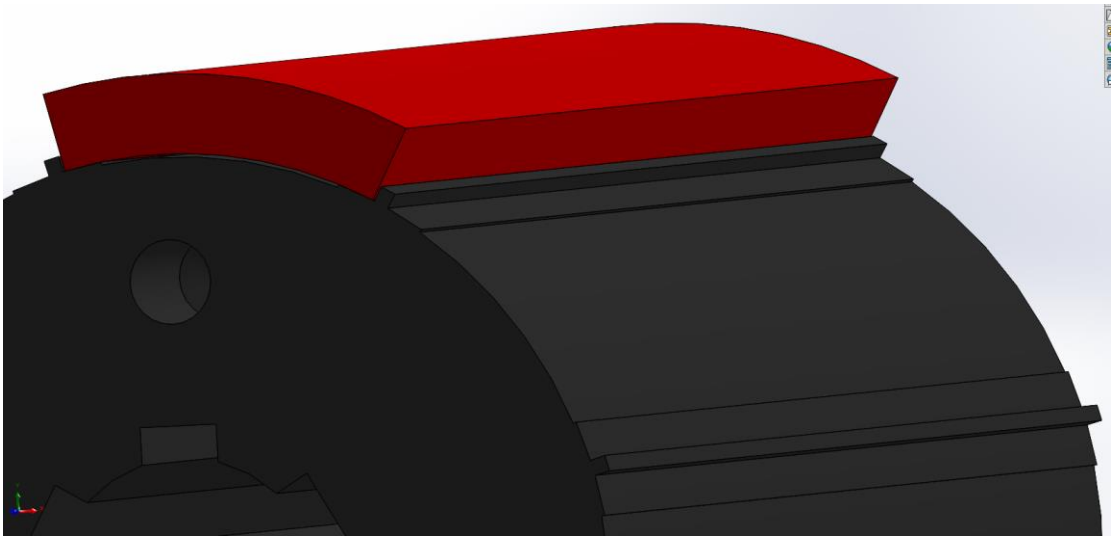

**Figure 5.8: Positioning of the PMs in the inner rotor**

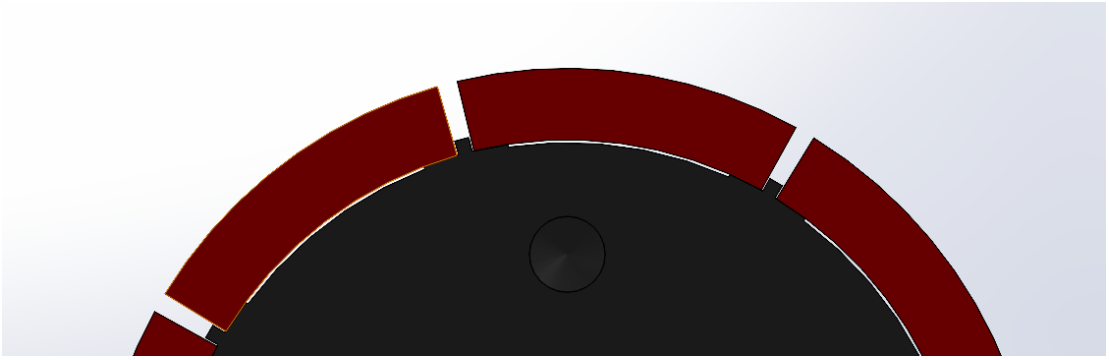

**Figure 5.9: Detail of the configuration of epoxy glue placement in the inner rotor**

Similarly, for the outer rotor the design for epoxy glue placement is presented in Fig.5.10 and Fig.5.11.

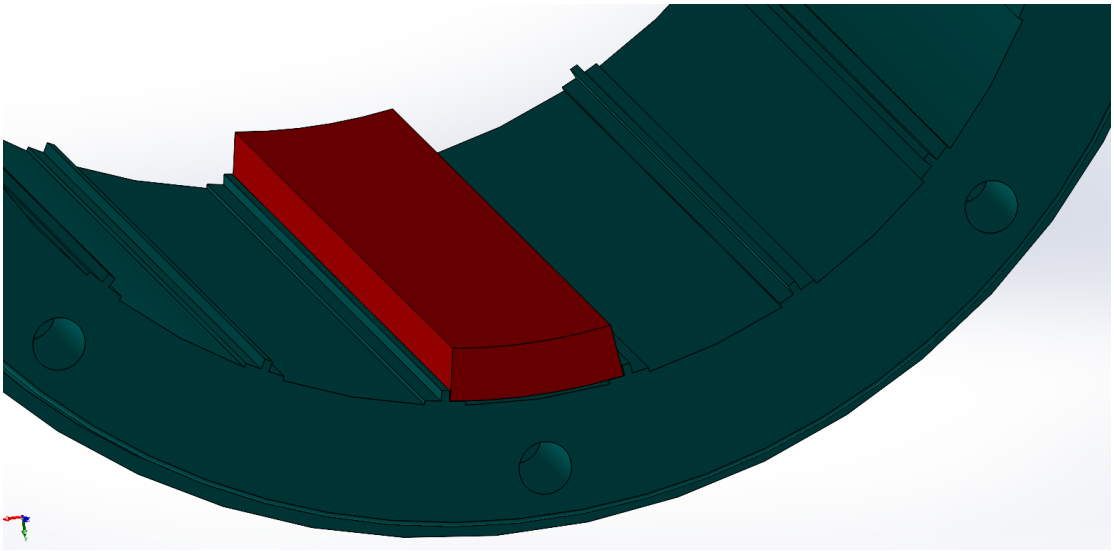

**Figure 5.10: Positioning of the PMs in the outer rotor**

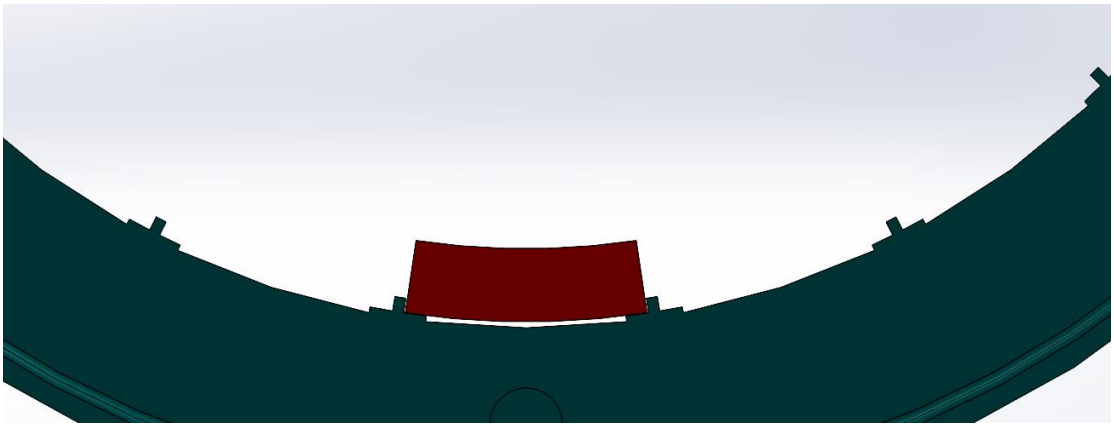

**Figure 5.11: Detail of the configuration of epoxy glue placement in the outer rotor**

## *5.5 Bearing selection and natural frequencies of the CMG*

An important design parameter of the CMG is the selection of the ball bearings in the rotors. The selection of the ball bearings and their clearances with the shafts and housings, plays a crucial role on the natural frequencies of the system and expected life of operation of the bearing. In general, the optimal effective clearance is negative implying that preload is required as shown in Fig.5.12 [5.1].

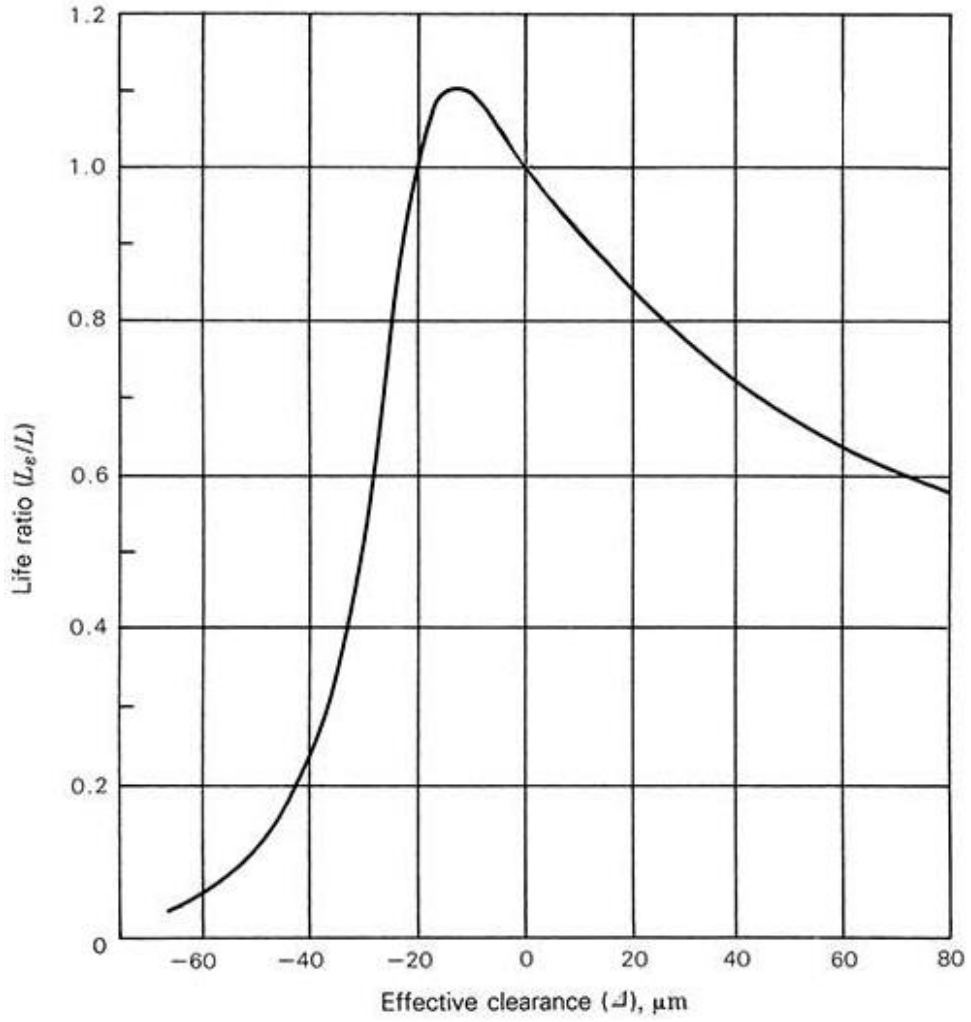


**Figure 5.12: Effective clearance and life ratio of a ball bearing**

From Fig.5.12 it is observed that the optimal clearance is in vicinity of -10 μm. For that, reason the ball bearings along with the shafts and housings and their tolerances are selected in a way that a total effective clearance of -10 μm is achieved in order to combine both rigidity and longevity [5.2].

During the analysis of the transient response of the CMG in Chapter 3, the period of possible oscillations is obtained. Since these oscillations have a significant energy as observed from Fig.3.4, the design of the CMG should avoid the vicinity of the frequencies as obtained from Eq.(3.15).

The highest frequency that can be observed (small oscillation amplitude case as illustrated in Appendix 3.1) can be determined from the following equation:

$$\omega^2 = \mathrm{M}_{\mathrm{stall}} \frac{\mathrm{p}}{\mathrm{I}} \tag{5.1}$$

where $\mathrm{M}_{\mathrm{stall}}$ is the stall torque of, $\mathrm{p}$ the number of pole pairs and $\mathrm{I}$ is the moment of inertia of each respective rotor.

In Fig.5.13 the natural frequency of the inner rotor is obtained in ANSYS. The effective clearance is -11 μm. The torsional frequency is approximately 412 Hz which is almost one order of magnitude higher than the oscillation frequency as obtained from Eq.(5.1).

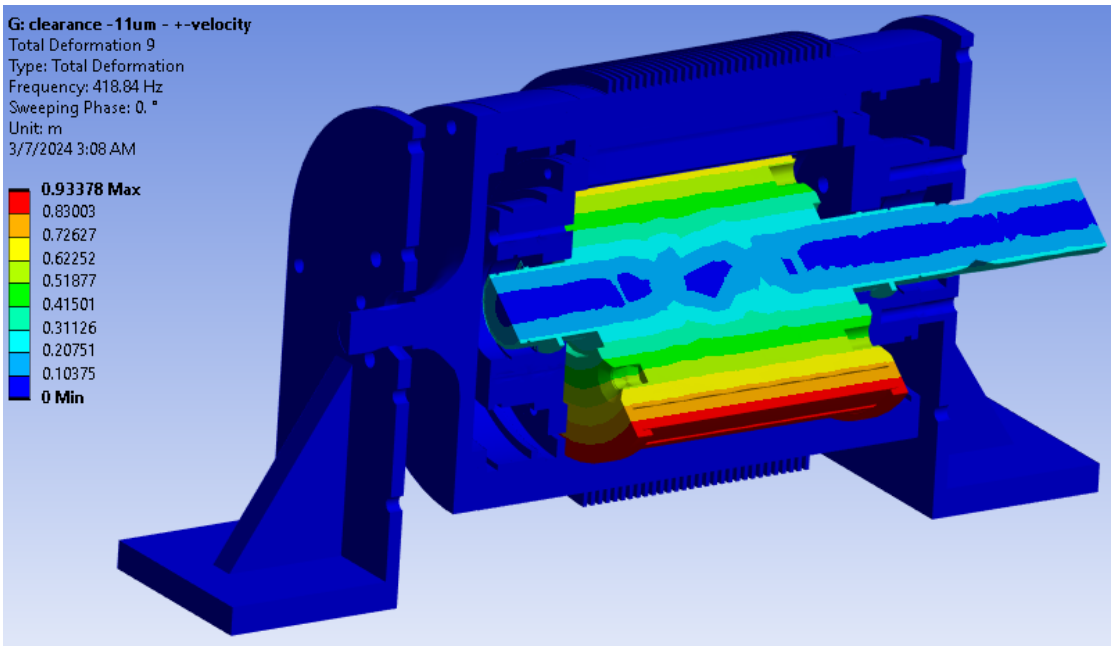


**Figure 5.13: Natural frequency of the inner rotor for an effective clearance of -11μm**

As a consequence, the inner rotor of the CMG is protected from resonant phenomena that could be caused during transient operation.

In Fig.5.14 the natural frequency of the outer rotor is obtained in ANSYS. The effective clearance is -11 μm. The torsional frequency is approximately 451 Hz which is almost one order of magnitude higher than the oscillation frequency as obtained from Eq.(5.1).

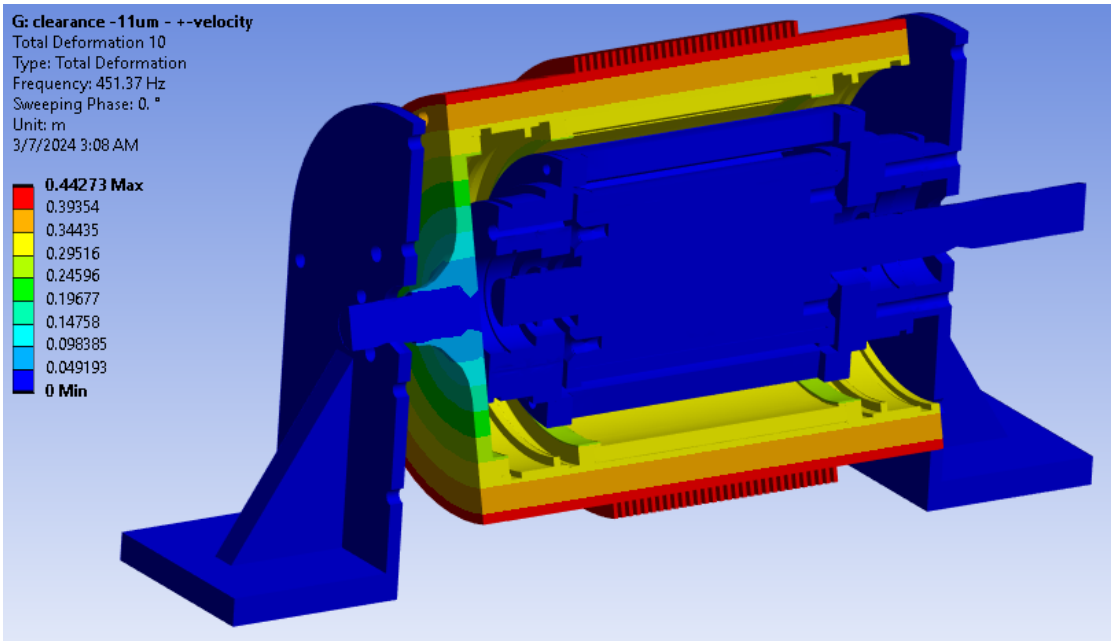


**Figure 5.14: Natural frequency of the outer rotor for an effective clearance of -11μm**

As a consequence, the outer rotor of the CMG is protected from resonant phenomena that could be caused during transient operation.

## *5.6 Temperature calculation of the CMG due to power losses*

From the analytical model developed in Chapter 4, the eddy current and power losses can be calculated. It is important to calculate the increase of temperature in the CMG in order to determine whether the PMs are affected and if the system will degredate as the time progresses. The highest losses are expected to be observed in the outer rotor following the analysis in Chapter 4. To increase the effective cooling area, the outer rotor is designed with fins as shown in Fig.5.15.

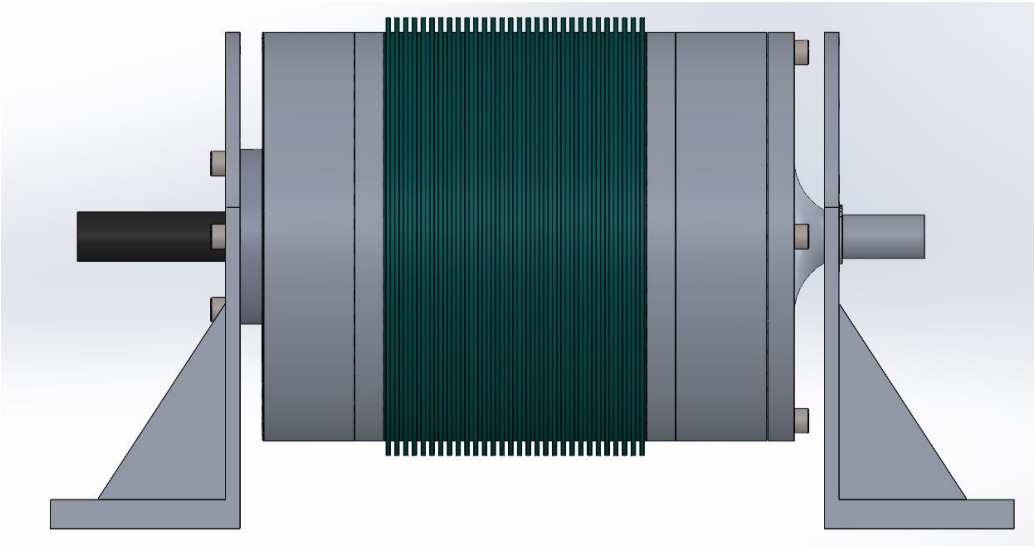

**Figure 5.15: Cooling fins in the outer rotor**

A transient thermal analysis was conducted in ANSYS in order to calculate the temperature on the PMs of the outer rotor. The inner rotor angular velocity was considered to be equal to 2500 rpm.

In Fig.5.16 the temperature profile of the PMs in the outer rotor is presented after 10 minutes of operation.

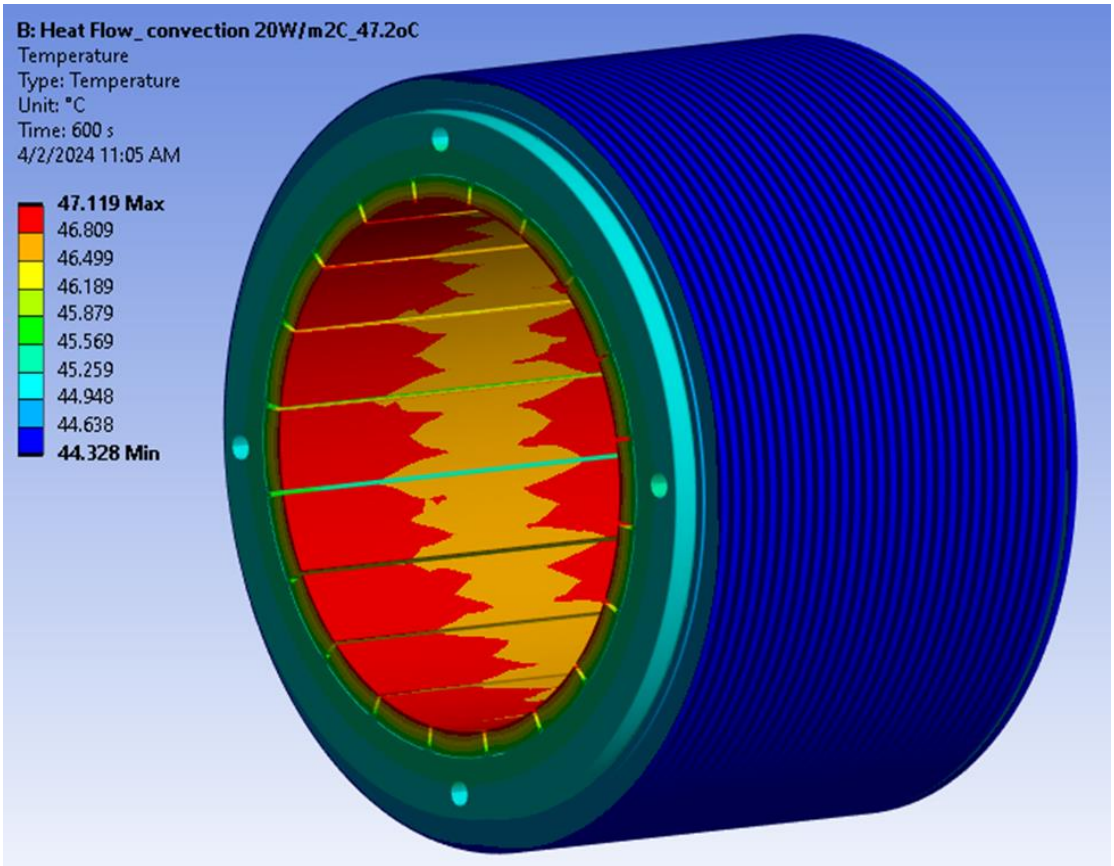


**Figure 5.16: Temperature profile of the outer rotor**

The temperature is lower than 50$^{o}$C and therefore the PMs are not affected from the power losses due to eddy current phenomena. However, as established in Chapter 4 magnet segmentation could significantly decrease the power losses and consequently the CMG could operate at even higher rotational speeds.

## *5.7 Torque ripple due to radial forces*

The magnetic induction in the CMG besides inducing tangential forces that result in applied torques in the two rotors, induce radial forces. As a consequence, the ferromagnetic segments in the modulator ring are displaced. Therefore, the relative position of segments changes as the CMG rotates. As a result the different geometry of the modulator ring at each angle of rotation yields different induced torques that could insert torque ripple during the operation of the CMG [5.3]. For the calculation of this phenomenon, a transient model taking into account radial forces applied on the modulator ring at each angle of rotation and the displacement of the modulator ring depending on the applied radial force is constructed.

The radial force can be calculated from the Maxwell Stress Tensor [5.4] from the following equation:

$$F_r = \frac{\delta L r_3}{4\pi\mu_0}\int_0^{2\pi}[B_r^2(r_3) - B_\theta^2(r_3)]d\theta \quad (5.2)$$

Due to the deflection of the ferromagnetic segments, the gap between the modulator ring and the rotors is not constant in the z-direction. Therefore, the torque applied to the rotors is calculated from:

$$M_{in}(r_2) = \int_0^L dm_{in}(z)dz \quad (5.3)$$

$$M_{out}(r_5) = \int_0^L dm_{out}(z)dz \quad (5.4)$$

where $dm_{in}$and $dm_{out}$ are the different torque values that appear along the z-axis.

From the performed analysis it was calculated that the torque ripple in the CMG due to radial forces is 0.2-0.3% which is near the order of the second torque harmonic. The value of the torque ripple is small and therefore this phenomenon is not expected to have a significant role during the operation of the CMG.

## *Chapter 5-Conclusions*

In this Chapter a detailed design of a CMG drive is presented showcasing the important designs aspects for manufacturing a robust and efficient CMG drive. Special attention was given to the placement and security of the PMs in the two rotors. A detailed analysis regarding the bearing tolerances and their subsequent effect on the natural frequencies of the CMG drive is conducted illustrating its significance as a design aspect. Furthermore, a transient thermal analysis is conducted in order to investigate whether the power losses due to eddy current losses could increase the temperature of the PMs, leading to degradation of the system as whole. It was shown that the temperature in the PMs did not exceed 50$^{o}$C and therefore the CMG with the proposed design is not expected to have temperature problems during its operation. However, by implementing the magnet segmentation technique the temperature during the operation of the CMG could decrease further that could make possible the achievement of higher rotational speeds. Finally, an investigation of the radial forces on the induced torques in the rotors was conducted. It was shown that the torque ripple due to the relative displacement of the modulator ring was in the order of the second torque contributing harmonic and therefore this phenomenon is not expected to pose problems during the operation of the CMG.

## *Chapter 5-References*

[5.1] Required minimum initial internal clearance – SKF.

[5.2] T. A. Harris and M. N. Kotzalas, Essential concepts of bearing technology. 2006

[5.3] Tzouganakis, P., Gakos, V., Kalligeros, C., Papalexis, C., Tsolakis, A., & Spitas, V. (2022). Torque ripple investigation in coaxial magnetic gears. In MATEC Web of Conferences (Vol. 366, p. 01004). EDP Sciences.

[5.4] Ye, Q., & Lin, H. (2017). On deriving the Maxwell stress tensor method for calculating the optical force and torque on an object in harmonic electromagnetic fields. European Journal of Physics, 38(4), 045202.

# *Thesis Conclusions*

In the present thesis two analytical 2D models for fast and efficient calculation of the applied torques for every rotation angle, geometry configuration and constitutive parameters of the magnets using the Maxwell Stress Tensor were introduced. The first model refers to the standard CMG drive, while the second to the Halbach-array CMG drive, due to its comparative advantages. The results obtained from the models were compared against those obtained from FEA. The calculated torques at the inner and outer rotor were in perfect agreement with FEA, however the analytical models were more than two orders of magnitude faster. In addition, an analytical calculation of the torque ripple in coaxial magnetic gear drives is made possible using the proposed models. An investigation of the influence of the modulator ring on stall torque was performed illustrating that there is an optimum arc length for the ferromagnetic segment to maximize torque density.

Furthermore, the dynamical equations of the coaxial magnetic gear drive were formulated and a model was developed to simulate the dynamical response of the system without the requirement of torque calculation at each time step that significantly decreases computational cost. The slippage phenomenon was thoroughly investigated in the present thesis. It was demonstrated that the governing equations of the dynamical response of the coaxial magnetic gear are the same with the dynamical equation of the driven pendulum. A non-dimensional criterion was formulated for the prediction of the dynamical behavior of the CMG drive during transient operation. Finally, it was demonstrated that the dynamical response of the CMG drive could exhibit chaotic behavior under certain conditions. With the developed analysis, besides the significant reduction of the computational cost important insights regarding the complex dynamical phenomena during the operation of CMG drives are obtained.

Moreover, a detailed analysis regarding the calculation of power losses during the operation of CMGs has been conducted. Using the analytical calculation of the magnetic induction the eddy current losses in the permanent magnets of the CMG and the core losses on the modulator ring were obtained. An investigation on the effect of the magnet segmentation to the power losses was conducted, illustrating that eddy current losses can be significantly reduced by applying this technique.

Finally, a detailed design of a CMG drive is presented showcasing the important designs aspects for manufacturing a robust and efficient CMG drive. A detailed analysis regarding the bearing tolerances and their subsequent effect on the natural frequencies of the CMG drive is conducted illustrating its significance as a design aspect.

# *Thesis Novelties*

In the present thesis, the following novelties regarding the modelling of coaxial magnetic gear drives were made:

- An analytical model for the calculation of the induced torques in the two rotors for every configuration and constitutive parameters of the standard CMG was established. In addition, the developed model also facilitates the analytical calculation of torque ripple. The model was generalized for the case of Halbach-array CMGs.

- The applied torque in the two rotors can be calculated as a function of the stall torque and the position of the two rotors. Therefore, only one calculation of the magnetic induction in the CMG is required (in the stall torque position) to determine the induced torques in the two rotors for every angle of their rotation. As a result, the applied torques are calculated analytically as a function of rotation that reduces significantly the computational cost and facilitates the formulation of an analytical system of ODEs for the dynamical response of the CMG drive.

- The dynamical response of the CMG during transient operation was thoroughly investigated. Due to the analytical expression of the applied torques as a function of the rotation angles of the rotors, an analytical system of ODEs for the dynamical response of CMGs was formed. It was shown that the dynamical equations of CMGs resemble the driven pendulum equation. A non-dimensional criterion was formulated for the prediction of the dynamical behavior of the CMGs during transient operation. Therefore, a significant reduction of the computational cost was achieved since no iterative methods are required for the simulation of the CMG during transient operation. Furthermore, important insights regarding the complex dynamical phenomena during the operation of CMG drives are obtained. Finally, it was demonstrated that the dynamical response of the CMGs could exhibit chaotic behavior under certain conditions.

# *Future Work*

From the observations of the present thesis, some ideas regarding future work are presented below:

- The present analysis regarding the analytical modelling of the scalar magnetic potential, the magnetic induction and the induced torques in the two rotors is implemented through a 2D model. It would be interesting to investigate the possibility of an analytical 3D model that would take into consideration the edge effects on the CMG drive.
- The modelling of the dynamical response of the CMG during transient operation could include the effect of damping. The power losses as discussed in Chapter 4 of the present thesis can be attributed mainly to the eddy current losses in the PMs of the CMG drive. It was demonstrated that the power losses in each rotor are proportional to the square of their respective angular velocity. Including the phenomenon of damping could lead to similar equations as the coupled damped-driven pendulum. However, in that case the two dynamical equations of the two rotors cannot be decoupled and therefore the dynamical response would be even more complex and chaotic compared to the presented case were damping is neglected. Therefore, it could be interesting to investigate the dynamical response of the CMG under these conditions.
- A generalized optimization could be implemented taking into account parameters such as the achieved torque density, the minimization of slippage during transient operation and the reduction of the power losses due to eddy current and core losses. Even though such an optimization process could be time consuming the analytical models derived in the present thesis can facilitate such endeavour.
- It would be important to investigate how the analytical models and results obtained in the present thesis compare to experimental results.

With the proposed ideas of future work the analysis and understanding of the complex phenomena that govern CMG drives could be improved that could possibly lead to their wider adoption in the industry.

# *Thesis Publications*

The following publication in international journals and conferences were made on coaxial magnetic gears:

**Publications in International Journals:**

1. Tzouganakis, P., Gakos, V., Papalexis, C., Kalligeros, C., Tsolakis, A., & Spitas, V. (2024). Chaotic behaviour in the dynamical response of coaxial magnetic gears during acceleration. Chaos, Solitons & Fractals, 187, 115441.

2. Tzouganakis P, Gakos V, Kalligeros C, Papalexis C, Tsolakis A, Spitas V. Torque Calculation and Dynamical Response in Halbach Array Coaxial Magnetic Gears through a Novel Analytical 2D Model. Computation. 2024; 12(5):88.

3. Nikolarea N, Tzouganakis P, Gakos V, Papalexis C, Tsolakis A, Spitas V. Detailed Investigation of the Eddy Current and Core Losses in Coaxial Magnetic Gears through a Two-Dimensional Analytical Model. Mathematical and Computational Applications. 2024; 29(3):38.

4. Tzouganakis, P., Gakos, V., Kalligeros, C. et al. Formulation of a non-dimensional criterion for stable dynamical response in coaxial magnetic gears. J Eng Math 144, 19 (2024).

5. Tzouganakis, P., Gakos, V., Kalligeros, C., Tsolakis, A., & Spitas, V. (2023). Fast and efficient simulation of the dynamical response of coaxial magnetic gears through direct analytical torque modelling. Simulation Modelling Practice and Theory, 123, 102699.

**Publications in International Conferences:**

1. Tzouganakis, P., Gakos, V., Kalligeros, C., Papalexis, C., Tsolakis, A., & Spitas, V. (2022). Torque ripple investigation in coaxial magnetic gears. In MATEC Web of Conferences (Vol. 366, p. 01004). EDP Sciences.

# *Other publications of the author*

**Publications in International Journals as first author:**

1. Tzouganakis, P., Gakos, V., Kalligeros, C., Papalexis, C., & Spitas, V. (2024). A novel time-dependent analytical model for optimizing efficiency and valve timing in Ericsson engines. Journal of Thermal Analysis and Calorimetry, 1-9.

2. Tzouganakis, P., Kalligeros, C., Papalexis, C., Koronaki, I., Antonakos, G., & Spitas, V. (2022). A new second order thermal model for accurate simulation of the transient and steady–state response of beta-type Stirling engines based on time-varying calculation of thermal losses. International Journal of Engine Research, 14680874221132026.

**Publications in International Journals:**

1. Papalexis, C., Rakopoulos, D., Nikolopoulos, N., Della Rocca, A., Jochler, G., Tassa, O., ... & Spitas, V. (2023). Developing Creep and Stress Relaxation Models to Assess the Service Life of an Additive Manufactured Industrial-Scale Recuperator Utilizing Inconel 625 and AISI 310S Materials. Materials, 16(22), 7226.

2. Papalexis, C., Stefanitsis, D., Zeneli, M., Nikolopoulos, N., & Tzouganakis, P. (2023). Proof of Concept of a Novel Solid–Solid Heat Exchanger Based on a Double L-Valve Concept. Energies, 16(17), 6156.

3. Kalligeros, C., Papalexis, C., Vasileiou, G., Tzouganakis, P., Spitas, C., Spitas, V. (2023). Exploiting double-flank roll testing spur gear measurements to determine gear parameter deviations through numerical simulation of free-form meshing gears. Simulation Modelling Practice and Theory, 126, 102757.

4. Tsolakis, E., Kalligeros, C., Tzouganakis, P., Koulocheris, D., & Spitas, V. (2021). A novel experimental setup for the determination of the thermal expansion coefficient of concrete at cryogenic temperatures. Construction and Building Materials, 309, 125134.

**Publications in International Conferences:**

1. Georgitzikis, V., Breda, S., Kalligeros, C., Spitas, V., Rogkas, N., Cicalese, G., ... & Fontanesi, S. (2023). Thermodynamic and Tribological Analysis of an Innovative Mechanism for Reciprocating Machines (No. 2023-24-0016). SAE Technical Paper.

2. Kalligeros, C., Koronaios, P., Tzouganakis, P., Papalexis, C., Tsolakis, A., & Spitas, V. (2022). Development of a free-form tooth flank optimization method to improve pitting resistance of spur gears. In MATEC Web of Conferences (Vol. 366, p. 01003). EDP Sciences.